

TECHNICAL UNIVERSITY OF BERLIN

MASTER'S THESIS

**Design and Optimization of a Hubless Rim-Driven Thruster
for an Autonomous Surface Vehicle using RANSE Simulations**

Author:
Heinrich Grümmer

Enrolment Number:
320072

Supervisor:
Dr.-Ing. Stefan Harries

Reviewer:
**Prof. Dr.-Ing. Andrés
Cura Hochbaum**



*A thesis submitted in partial fulfillment of the requirements
for the degree of Master of Science*

**Dynamics of Maritime Systems
Institute for Land and Sea Transport Systems**

November 14, 2016

Declaration of Authorship

Hiermit erkläre ich, dass ich die vorliegende Arbeit selbstständig und eigenhändig sowie ohne unerlaubte fremde Hilfe und ausschließlich unter Verwendung der aufgeführten Quellen und Hilfsmittel angefertigt habe.

Ort, Datum

Unterschrift

Scope

Within this thesis a hubless rim-driven thruster for an autonomous surface vehicle (ASV) shall be designed and optimized using RANSE simulations. The task is derived from the aXatlantic project, aiming at a solar powered, autonomous and unmanned crossing of the Atlantic. The design of the nozzle and the propeller shall be derived from an optimization process, using CAESSES as a simulation-driven design toolbox along with a fully automatic grid generation process and the open source CFD software OpenFOAM.

In a first step, the simulation is to be set up and verified by systematic comparison to existing experimental data of the Ka4-70 nozzled propeller by MARIN (see J. D. van Manen and M. W. C. Oosterveld, *Analysis of Ducted-Propeller Design*, Society of Naval Architects and Marine Engineers, Nov. 1966). Open water simulations are to be made and compared to Oosterveld's findings (see M. W. C. Oosterveld, *Wake adapted ducted propellers*, PhD thesis, Delft University of Technology, 1970). A dependency study, including dependencies on the size of the computational domain, the number of propeller revolutions simulated, chosen time step, Reynolds number and mesh resolution needs to be carried out.

The simulations shall be based on OpenFOAM's dynamic mesh handling capability and the coupling of the rotating propeller-region and the stationary part of the domain via an arbitrary mesh interface (AMI). Only a section of the overall domain will be simulated due to the rotational symmetry of the problem. Utilizing a wall function approach, a substantial number of variants shall be investigated at a reasonable computational effort. Empirical models accounting for the neglect of friction within rim and nozzle need to be employed to improve the solutions accuracy and allow for meaningful performance predictions of the examined thruster.

In a second step, a fully-parametric model of both the nozzle and the propeller blade, limited by the electromagnetic and geometric specifications of the available motor, shall be developed. The nozzle section design can be based on a class shape transformation (CST) technique, allowing for a very wide range of geometric variations. To limit the number of design variables, the propeller design will be based on an existing blade series with characteristics suitable for the task at hand and only major geometric parameters will be fed into the optimization algorithm. A preliminary design of the system shall serve as the starting point for the optimization.

Finally, the design space will have to be examined using an exploration algorithm. A subsequent exploitation should be carried out so as to further investigate and optimize the most promising design variants. Considering tests

and calculations regarding the ASV's hull, solar cells and electric motor, a well-founded decision towards a final thruster shall be made in order to allow the vessel to operate at high efficiency.

The thesis is supervised by Prof. Dr.-Ing. Andrés Cura Hochbaum (Dynamics of Maritime Systems at TU Berlin) and Dr.-Ing. Stefan Harries (CEO of FRIENDSHIP SYSTEMS and external lecturer at TU Berlin). The candidate working on the thesis is asked to provide updates of his work and discuss results on a regular basis.

Abstract

Keywords: Optimization, Rim-Driven Thruster (RDT), Computational Fluid Dynamics (CFD), Computer Aided Engineering (CAE), Simulation-Driven Design (SDD), Response Surface Methodology (RSM), Class Shape Transformation (CST), Autonomous Surface Vehicle (ASV)

The thesis covers the optimization of a hubless RDT for use in a small ASV targeted to cross the Atlantic [11]. A CFD setup for viscous flow simulations is derived from comparison with existing experimental findings [22] based on OpenFOAM. The accuracy in performance prediction is enhanced by empirical models accounting for the neglect of friction within nozzle and rim. A sophisticated parametric CAD model of the thruster unit is compiled within CAESES. The modeling of the nozzle's section is based on CST methodology. Geometric constraints, imposed by the embedded Brushless DC (BLDC) motor, are incorporated and optimized motor position and section thickness is determined for every design variant. An automatic grid generation procedure is evolved using Pointwise. Hull resistance data is obtained from experiments carried out at TU Berlin's towing tank facilities. Subsequently, an optimization with the objective of maximizing the vessel's speed at a given power supply is carried out. CAESES is used as a framework for the SSD process. An exploration based on a Sobol algorithm, followed by an optimization utilizing a surrogate (RSM) model are carried out. An improvement in open water efficiency of 168 % is achieved, corresponding to an increase of speed from 1.22 m/s to 1.46 m/s .

Zusammenfassung

Schlüsselwörter: Optimierung, Ringpropeller, Numerische Strömungsmechanik, Rechnergestützte Konstruktion, Rechnergestützter Entwurf, Response Surface Methode, Class Shape Transformation, Autonomes Oberflächenfahrzeug

Die Arbeit behandelt die Optimierung eines Ringpropellers für ein autonomes Oberflächenfahrzeug welches für eine Atlantiküberquerung eingesetzt werden soll [11]. Basierend auf OpenFOAM wird ein CFD-Setup für die Strömungssimulation erstellt. Eine Abschätzung der Energiedissipation aufgrund der Strömung im Spalt zwischen Düse und Propellerring erfolgt durch den Abgleich mit bestehenden experimentellen Daten [22]. Basierend auf der CST Methodik, unter Berücksichtigung der Einschränkungen durch den für die Installation des Elektromotors benötigten Bauraum, wird in CAESES ein komplexes parametrisches CAD Modell aufgesetzt. Dieses stellt die optimale Profilhöhe der Düse bei geeigneter Positionierung des Motors für beliebige Parameterkombinationen sicher. Die automatisierte Gittergenerierung erfolgt mittels Pointwise und Widerstandsversuche im Schleppkanal der TU Berlin liefern relevante Daten zum Schiffsrumpf. Anschließend erfolgt in CAESES die Optimierung mit dem Ziel der Maximierung der Schiffsgeschwindigkeit unter Aufwendung der zur Verfügung stehenden Antriebsleistung. Die Optimierung umfasst eine Sobol-Sequenz in der Explorationsphase, sowie eine darauf aufbauende Optimierung mittels RSM. Ergebnis der Arbeit ist eine Verbesserung des (open water) Wirkungsgrades auf 168 %, was einer Erhöhung der Schiffsgeschwindigkeit von 1.22 m/s auf 1.46 m/s entspricht.

Acknowledgements

I would like to thank my supervisor Dr.-Ing. Stefan Harries (CEO of FRIENDSHIP SYSTEMS and external lecturer at TU Berlin) for his support – not just recently in context of this thesis, but also by encouraging me to aim the aXatlantic project towards a professional level since it started in 2015.

I would also like to thank Prof. Dr.-Ing. Andrés Cura Hochbaum (Head of chair Dynamics of Maritime Systems (DMS) at TU Berlin) for joining the team and allowing for this work to be taken another significant step ahead.

Furthermore, I would like to acknowledge:

Dipl.-Ing. Karsten Rieck and his colleagues for their hands-on support during the towing-tank experiments,

Dr. Reinhard Schulze for his contribution of an initial draft of the baseline blade-design,

Prof. S. M. Abu Sharkh (University of Southampton) for providing me with factual papers from his archives

and all my family and friends for their ongoing support through the years of my study which will be finished with this thesis. Thank you.

Contents

Declaration of Authorship	i
Scope	ii
Abstract	iv
Zusammenfassung	v
Acknowledgements	vi
1 Introduction	1
1.1 Preliminary work and objectives	1
1.2 On rim-driven thrusters	3
1.3 Recent work	4
2 Reference Simulation	7
2.1 Reference design	7
2.1.1 Blades according to table of offsets	7
2.1.2 Blades according to given figure	9
2.1.3 Hub	10
2.1.4 Nozzle	10
2.1.5 Parametric model	11
2.2 Grid generation	11
2.2.1 Separating the propeller region	13
2.2.2 Treatment of near-wall cells	13
2.2.3 Grid generation of propeller region	15
2.2.4 Grid generation of domain region	17
2.3 Simulation setup	18
3 Verification of reference simulation	22
3.1 Domain size and number of revolutions	22
3.2 Reynolds number and time discretization	24
3.3 Mesh resolution	26
3.4 Convergence and mesh quality	27
3.5 Correction of frictional dissipation	29
3.6 Comparison of results	32
4 Optimization	34
4.1 Baseline design	34
4.1.1 Class Shape Transformation (CST) methodology	34

4.1.2	Nozzle design	35
4.1.3	Propeller design	38
4.2	Design variables	39
4.3	Objective	41
4.4	Grid generation	46
4.5	Simulation setup	48
4.6	Exploration phase	49
4.7	Optimization phase	50
4.8	Evaluation	53
5	Verification of optimized thruster design	57
5.1	Estimated self propulsion point	57
5.2	Reynolds number of optimized variant	58
5.3	Mesh resolution of optimized variant	59
5.4	Extrapolation of forces	60
5.5	Residuals	63
6	Conclusion	65
6.1	Optimized thruster	65
6.1.1	Geometry comparison	65
6.1.2	Visualization	69
6.1.3	Performance	73
6.2	Re-evaluation of invalid design variants	76
6.3	Summary	77
6.4	Outlook	78
A	Schematic hull design	80
B	Blade geometry: table of offsets	82
C	Program files overview	83
	Bibliography	85

List of Figures

2.1	Ka 4-70 propeller in nozzle 19A	8
2.2	Leading edge fitting procedure	9
2.3	MARIN Nozzle 19A	11
2.4	Parametric model	12
2.5	Hub and rim, surface meshes	16
2.6	Exploded view, propeller region mesh	16
2.7	Domain region mesh	17
3.1	Study: domain size and number of revolutions	24
3.2	Study: time step and Reynolds number	25
3.3	Study: mesh resolution	25
3.4	Residuals of p and v_x	28
3.5	Forces at $J = 0.5$	28
3.6	Open water diagram	32
4.1	Total resistance data and curve fitting	44
4.2	Automatic grid generation (nozzle)	46
4.3	v_d evaluated at different rotational speeds	54
4.4	$P(J)$ at self propulsion point	55
5.1	Grid convergence	61
5.2	Number of revolutions, optimized design	61
5.3	Convergence of moments	62
5.4	Residuals p and v_x , simulation of optimized design	64
6.1	Nozzle: baseline and optimized design	66
6.2	Linesplan: baseline and optimized propeller	67
6.3	Pitch: baseline and optimized propeller	68
6.4	Baseline thruster images	69
6.5	Optimized thruster images	69
6.6	Pressure distribution upstream	70
6.7	Pressure distribution propeller-plane	70
6.8	Pressure distribution downstream	71
6.9	Pressure distribution and formation of tip vortices 1	71
6.10	Pressure distribution and formation of tip vortices 2	72
6.11	Pressure distribution and formation of tip vortices 3	72
6.12	Open water diagram: baseline vs. optimum	75

List of Tables

2.1	Table of offsets for the hub given in figure 2.1	11
2.2	Estimated non-dimensional wall distance	14
2.3	Average non-dimensional wall distance	14
2.4	Boundary and initial conditions	19
3.1	Grid resolution reference design	26
3.2	Mesh quality and statistics	30
4.1	Design variables	40
4.2	Total resistance experimental data	44
4.3	Sobol sequence and results	51
4.4	Dakota algorithm design variables	52
4.5	Dakota algorithm results	53
5.1	Verification of optimized design	58
5.2	Grid resolution optimized design	60

List of symbols

symbol	description	unit
propulsive characteristics		
η_o	open-water efficiency	[-]
η_{o,J_d}	open-water efficiency at J_d	[-]
J	coefficient of advance	[-]
J_d	design advance coefficient	[-]
v_s	ship speed	[m/s]
v_d	design speed of vessel ($v_s(J_d)$)	[m/s]
v_a	speed of advance	[m/s]
n_d	design rotational speed ($n(J_d)$)	[1/s]
T	thrust	[kg·m/s ²]
T_N, T_P, T_B, T_R	thrust components: (nozzle, propeller, blade, rim)	[kg·m/s ²]
Q	torque	[kg·m ² /s ²]
Q_P, Q_B, Q_R	torque components: (propeller, blades, rim)	[kg·m ² /s ²]
K_T	thrust coefficient	[-]
$K_{T,N}, K_{T,P}, K_{T,B}, K_{T,R}$	thrust coefficient components: (nozzle, propeller, blade, rim)	[-]
K_{T,J_d}	thrust coefficient at J_d	[-]
K_Q	torque coefficient	[-]
$K_{Q,P}, K_{Q,B}, K_{Q,R}$	torque coefficient components: (propeller, blade, rim)	[-]
K_{Q,J_d}	torque coefficient at J_d	[-]
P	power delivered at propeller shaft	[kg·m ² /s ³]
R_T	total resistance	[kg·m/s ²]
C_B	block coefficient	[-]
t	thrust deduction coefficient	[-]
w	wake fraction coefficient	[-]
η_H	hull efficiency	[-]
c_F	frictional resistance coefficient	[-]
c_R	residual resistance coefficient	[-]
c_A	additional resistance coefficient	[-]

CST methodology

ζ_u	upper nozzle curve	[—]
ζ_l	lower nozzle curve	[—]
C	general class function	[—]
N_1	coefficient of class function	[—]
N_2	coefficient of class function	[—]
ψ	lengthwise coordinate	[—]
S_u	shape function (upper)	[—]
S_l	shape function (lower)	[—]
N_u	coefficient of shape function S_u	[—]
N_l	coefficient of shape function S_l	[—]
A_u	parameter of shape function S_u	[—]
A_l	parameter of shape function S_l	[—]
$S(\psi)$	component shape function	[—]
K_i^n	coefficient of function $S(\psi)$	[—]

correction of frictional losses

A_S	area of rim-end face (suction side)	[m^2]
A_P	area of rim-end face (pressure side)	[m^2]
$Q_{rim,end}$	additional torque due to friction of rim-end faces	[$kg \cdot m^2 / s^2$]
$Q_{rim,out}$	additional torque due to friction of rim-out faces	[$kg \cdot m^2 / s^2$]
Ta	Taylor number	[—]
R_i	inner cylinder radius	[m]
R_o	outer cylinder radius	[m]
d	gap width	[m]
s	axial gap clearance	[m]
h	radial gap clearance	[m]
l_{rim}	axial rim length	[m]
\bar{p}_p	mean circumferential pressure (pressure side)	[$kg/m \cdot s^2$]
\bar{p}_s	mean circumferential pressure (suction side)	[$kg/m \cdot s^2$]

simulation setup

D_D	domain diameter	[m]
x	coordinate axis of propeller rotation	[—]
x_0	position of propeller plane	[—]
l_i	domain inlet length	[m]
l_o	domain outlet length	[m]
R_D	domain radius	[m]
n_{rev}	number of full propeller revolutions	[—]
n_{steps}	number of time steps	[—]
Δt	time step	[s]

geometry

P	propeller pitch	$[m]$
D	propeller diameter	$[m]$
R	propeller radius	$[m]$
R_{hub}	hub radius	$[m]$
r	local propeller radius	$[m]$
n_{blades}	number of propeller blades	$[-]$
α	local blade-section angle	$[\circ]$
$\alpha_{total}(r)$	blade-section angle	$[\circ]$
$\alpha_{baseline}(r)$	initial blade-section angle	$[\circ]$
$\Delta\alpha$	adds offset to $\alpha_{baseline}(r)$	$[\circ]$
$\alpha_{distribution}$	adds radial distribution to $\alpha_{baseline}(r)$	$[-]$
Δc	additional camber	$[-]$
$c_{distribution}$	additional radial camber distribution	$[-]$
$c_r(\psi)$	camber function at local radius	$[-]$
α_{nozzle}	angle of attack (nozzle section)	$[\circ]$
l_{nozzle}	nozzle length	$[m]$
I_1, I_2, I_3	shape parameters A_l	$[-]$
O_1, O_2, O_3	shape parameters A_u	$[-]$
b_l	lower bound of design variable	$[-]$
b_u	upper bound of design variable	$[-]$
v_b	value of design variable at baseline	$[-]$

general symbols

n	rotational speed	$[1/s]$
ω	angular velocity	$[rad]$
p	pressure	$[kg/m \cdot s^2]$
ν	kinematic viscosity	$[m^2/s]$
ρ	density	$[kg/m^3]$
Y_+	non-dimensional wall distance	$[-]$
y	wall distance	$[m]$
f	scaling factor mesh resolution	$[-]$
Re_x	local Reynolds number	$[-]$
$Re_{0.7}$	local Reynolds number at $r/R = 0.7$	$[-]$
$l_{0.7}$	local characteristic length at $r/R = 0.7$	$[m]$
l_x	local characteristic length	$[m]$
v_{vec}	tangential velocity at blade	$[m/s]$
v_x	velocity component (x)	$[m/s]$
C_f	Schlichting skin-friction coefficient	$[-]$
τ_w	wall shear stress	$[kg/m \cdot s^2]$
u_*	friction velocity	$[m/s]$
Co	Courant number	$[-]$
S	wetted surface	$[m^2]$
a, b, c	curve fitting parameters	$[-]$

Chapter 1

Introduction

1.1 Preliminary work and objectives

The problem addressed in this thesis, is the design of a thruster unit, suitable for use in an ASV. The task is derived from the aXatlantic project [11] which aims at a solar powered, autonomous, unmanned crossing of the Atlantic. A possible future application of the system could be modern oceanography, climate research or any other field, where accurate live data of ocean surface state is of high value. There are many concepts of ocean going drones, providing measurements in deep water, but also subsurface and surface data, as well as weather information. All of them have different trade-offs, like buoys floating uncontrolled or wave gliders being prone to getting tangled in floating obstacles. Some have very limited power supply via batteries, others are slow or not maneuverable at all. Developing an ASV, which is solar powered and therefore able to undertake long lasting missions on the open seas has numerous advantages compared to existing concepts.

One of the main concerns in the design of the vessel was, to avoid the use of a long, weighted keel which protrudes from the bottom of the hull. This keel would allow the vessel to catch sea grass, rope, fishing lines and other objects that might be floating on the ocean surface and thus, get entangled. At the same time, a rather large surface on top of the boat is needed, to be able to collect enough solar energy to power the necessary hardware and propel the vessel.

Particular attention has been paid to the hulls self righting ability which is one of the key features of an autonomous boat operating on the high sea. A unique design has been developed based on an optimization process aiming at the most favorable hydrostatic characteristics. This design gives the boat self-righting ability without the use of a long keel, while keeping the above-water profile of the vessel as low as possible to avoid too much drift in high winds. A flat deck, carrying the solar cells, is placed on top of the main hull and supported by flaring *wings* above the waterline to give it sufficient structural integrity. Once flipped over, a design like this easily leads to a very stable position of the hull if the wings provide too much buoyancy. Therefore, the wings, main hull and solar deck do not enclose a watertight volume and hence do not create additional buoyancy in unfavorable areas. The main hull, housing all of the electronics necessary for navigation, communication, power supply and propulsion, is shaped almost circular in cross section and has a small

keel. This design, along with a center of gravity low enough, helps to provide a positive righting arm over a full 180° range of heeling angles.

The figures given in the appendix A show a schematic section view of the hull and the righting arm curves for the main hull, as well as for the main hull with attached, but watertight wings for a better understanding. It can be seen, that the main hull will return back to its upright position from any heeling angle, while the flat-top hull has its angle of vanishing stability at 145° and shows inverted stability at greater heeling angles. Two righting arm curves of the correct setup with non watertight wings are also given in A. One of them shows the righting arm curve of the baseline geometry. The second curve shows the righting arm curve, after the optimization towards a self-righting design with maximum stability has been carried out.

Based on this preliminary work, a propulsion system for the vessel had to be chosen. Again, the main focus was, to prevent the vessel from getting entangled, as the low torque available does not allow the mounting of rope or net-cutters on a propeller shaft. A hubless, rim-driven thruster (RDT) meets this requirement. In this application, the additional nozzle will unlikely contribute much to the efficiency, as nozzles usually show their potential when it comes to high blade loading and advance coefficients near bollard pull. However, the advantages offered by a RDT, engineered as a steerable thruster unit, outweigh the potentially higher power consumption.

Consequently, this thesis aims at designing the most suitable RDT for the aXatlantic hull. The design is limited by the electromagnetic and geometric specifications of the available motor and will be focused on the hydrodynamic aspects of the system rather than construction and manufacturing aspects. The open source software OpenFOAM will be used to carry out RANSE CFD simulations of tip-driven thrusters in homogeneous inflow. Experimental findings provided by Oosterveld in his comprehensive work on 'wake adapted ducted propellers' [22] are used, to verify the CFD results in the first part of the thesis. Empirical models will be used, to account for simplifications in the simulation setup and to gauge the results. In the second part of the thesis, a parametric geometry model of a RDT, feasible for use in the application of interest, will be generated, using the upfront CFD platform CAESES. An automated meshing procedure will be launched based on Pointwise as a grid generation tool. The CFD simulations are run using the setup and post processing routines evolved in the first stage. An exploration and subsequent optimization algorithm will control the geometry variation leading to a final RDT design. The objective will be to maximize the vessels speed, taking into account not only the hydrodynamic properties of the thruster and hull, but also the boundary conditions imposed by the remaining system.

The following section will provide a more detailed insight into the potentialities of nozzles and the benefits and trade-offs, related to ducted propellers, RDTs and hubless RDTs.

1.2 On rim-driven thrusters

Within this thesis, as well as in the literature, the terms rim-driven and tip-driven are used to describe the same matter. As opposed to a conventional propeller, driven via its shaft, the torque driving the propeller blades of a RDT is delivered via a surrounding ring that is structurally connected to the blade tips.

The propeller shaft, usually prone to getting caught in floating obstacles or debris, is missing in this configuration and the absence of a hub allows for objects to pass through the unit without interference. This is one of the significant benefits of RDTs over conventional propulsion systems as Freeman and Marshall [10] state in their article on this relatively new propulsion system. Numerical simulations were used in their work, not only to gain insight into the thrust characteristics and structural integrity of the system, but also to evaluate flow trajectories inside the unit. A high flow velocity area in the center of the shaft-less thruster supports the free passage of any debris, that otherwise might lead to fouling of the propeller.

The absence of a hub and shaft also diminishes the frictional losses of the propulsion unit and eliminates dissipation due to formation of a hub vortex [5]. As the blade tips are connected directly to the rim, no tip leakage vortex exists. The compact design also helps in saving cabin cubic, allows for a flexible mounting and aids in the reduction of secondary systems [5, 13, 31].

The mayor disadvantage of RDTs over conventional ducted propellers is that the ring, surrounding the propeller, needs to be countersunk into the nozzle [22]. Regardless of whether the power source is an electric motor, embedded into the nozzle, or if some kind of mechanic transmission is used to deliver the torque, this creates a small gap between the nozzle and ring. As the unit is fully submerged while operating, this gap is filled with fluid and the flow evolving leads to significant frictional losses. At the same time, if the thruster uses an electromagnetic motor, the fluid filling the air-gap works as a coolant and therefore allows compact motor designs and high power input without creating too much heat [14]. The viscous flow simulations in this thesis do not include this gap and the neglect of friction needs to be accounted for by separate empirical models, subsequently.

The nozzle of a RDT serves multiple different purposes and thus, needs to be designed specifically to suit the task at hand. In general, two types of nozzles can be distinguished, namely the accelerating and the decelerating nozzle. This discourse will omit the decelerating type, as its main purposes are the increase of pressure in the propeller region to avoid cavitation and the reduction of noise level. The accelerating type of nozzle can be subdivided into two different fields of application.

At low speeds and high screw loadings, as they often occur on tugboats or fishing trawlers, a duct surrounding the propeller has the most benefits over a conventional propeller. The high velocity on the inside of the nozzle leads to an excess pressure on the outside surface of the nozzle. Because of the nozzle's

section design, this pressure creates a force acting towards the direction of in-flow and hence, contributes to the total thrust of the propulsion system. The additional thrust created by the nozzle therefore increases towards bollard pull condition. As the speed of advance increases, the fixed nozzle creates substantial drag and thus, the efficiency decreases towards higher speeds [22].

If the main operating condition of the vessel concentrates on higher speeds of advance and light screw loading, the nozzle section needs to be chosen with respect to low viscous and pressure drag. Although this might not lead to better free running speed than an open propeller, other benefits provided by the nozzle can be kept. In the application at hand, the nozzle provides great protection for the propeller and, as described earlier, allows for the absence of a shaft and hub. Furthermore, the nozzle creates directional stability and provides exceptional maneuverability due to thrust vectoring of the steerable unit.

The nozzle section needs to be designed carefully, as the length and profile of the nozzle have a significant impact on the danger of flow separation and possible cavitation of the propeller and nozzle. If flow separation occurs, the drag will increase abruptly and the efficiency decreases. If the separation happens on the inside surface of the nozzle, the propeller will work in highly irregular flow and thus the efficiency decreases further. In general, flow separation occurs if the nozzle is too heavily loaded, but too light loading also leads to an increasing drag, as a large surface area induces unnecessary high skin-friction. In [22], Oosterveld calculates a rough approximation on the danger of flow separation, depending on the lift coefficient of the two dimensional nozzle profile. He also estimates the skin-friction drag based on empirical formulas and his results show that the optimum ideal efficiency can be written as a function of nozzle length to diameter ratio and thrust coefficient. His results show that a gain in efficiency at high screw loads is obtained at rather large ratios of length to diameter of the nozzle. At ratios higher than 1, the gain in efficiency is counterbalanced by the additional drag of the increasing nozzle surface. The contraction of the nozzle should be as large as possible without flow separation occurring at the inside surface and the propeller-thrust to total-thrust ratio must be as small as possible. At lower screw loadings and higher speeds of advance, the nozzle's length to diameter ratio must be kept as small as possible, consequently. This puts high requirements on the electric motor embedded in the nozzle. Only a low radial height allows for a profile of low drag and as the rim will be connected directly to the rotor, the axial length should not exceed the rim's dimension.

1.3 Recent work

In 2011, Cao Qing-ming et al. [5] investigated the steady wake field and loading distributions of a rim-driven thruster using a commercial RANS solver. Four different cases of propeller blades in a nozzle based on the Marin duct 37A were examined and the resulting total thrust and torque at different revolution rates were compared to experimental data. Rim surface effects are split up into rim-end, inboard and outboard faces and addressed by different models,

respectively. Empirical formulas were used to correct the torque losses and validated to be consistent with the measured values.

Bulten and Suijkerbuijk [3] conducted RANS CFD simulations, determining the full scale performance of steerable thrusters. The validation of the results was based on model scale measurements by Marintek in Norway. Straight, as well as oblique inflow conditions were simulated and the time averaged forces and moments induced by the interaction of the flow with shank and brackets upstream were evaluated. The amplitudes of forces and moments were found to be within less than 10% and accurate performance predictions in good agreement with the model tests have been made. The mesh used, featured a high quality boundary layer extrusion and a wall function was applied to keep the number of cells within reasonable limits. $Y+$ values within 200 and 300 were accepted, leading to an overall cell count of 1.5 million which was found to be sufficient to capture the general flow features well. Operating conditions ranging from bollard pull to free sailing condition were examined and a comparison between full and model scale CFD results, showing significant Reynolds scaling effect, has been made.

A rim-driven thruster which has been developed by Sharkh, Turnock and Draper [24], has been investigated by Dubas [7], who carried out steady state RANS CFD simulations, using the OpenFOAM integrated `MRFSimpleFoam` solver. The verification of the results involved the variation of the computational domain size, a mesh dependency study and a comparison between two different turbulence models, namely the RNG $k-\epsilon$ and the $k-\omega$ SST model. The results varied slightly from the experimental data used for comparison with increasing derivation towards lower advance coefficients. A breakdown of the total thrust and torque into the contributions of the different thruster components shows the negative effect of the use of stators and a duct with its profile symmetric to the center plane.

In [6], Dubas presents extensive explanation on a much more detailed view into the above mentioned thruster unit. Different analytical models, accounting for the friction occurring in the gap rim and nozzle are introduced and their results compared. Also an approach of estimating the friction using a separate CFD simulation as described by Batten [1] is pointed out, though not carried out. An optimization study of a slightly simplified thruster unit is conducted, incorporating a surrogate model and finally leading to an increase of absolute efficiency of 6%. The automatic geometry generation, as well as meshing, running of the simulation and post processing is described, using a number of different software tools suiting the various tasks.

Sharkh, Hughes, Lai and Turnock investigated an electromagnetic, tip-driven propeller (EDTP) unit, designed to use as a propulsor for underwater vehicles. Their work is related closely to the aim of this thesis and also helpful in the design and construction tasks carried out in parallel to this work. A good overview on all separate parts of their work is given in [25]. A lifting surface panel model is developed in [13] to allow performance prediction and optimization of the thruster. A comparison of a slotless and a slotted motor with similar radial dimensions, suitable for mounting within the nozzle is drawn

in [23]. Optimum winding configurations are determined, based on FEA and efficiency, as well as costs are compared and verified via experimental measurements. In [12], a prototype of an electromagnetic tip-driven thruster is tested in a towing tank over a range of advance speeds. Valuable information is given on design problems typical for RDTs and how they can be overcome. The experimental results are compared to a standard propeller and the influence of varying nozzle geometries, blade sections and dimensions is pointed out. In [24], the same thruster unit is tested at high input power of up to 6 kW and the results are compared to measurements by Oosterveld [22], whose findings also serve as a reference for the CFD simulations carried out in this thesis. PhD students associated with the project, carried out fundamental work on frictional losses and an apparatus to measure them is under construction [25], 2010.

Chapter 2

Reference Simulation

To assure the reliability of the obtained simulation results, a verification of the CFD setup will be performed. Therefore, studies on the solutions independence of mesh resolution, size of time step, Reynolds number, number of revolutions simulated and size of computational domain will be carried out, subsequently. A comparison of open water diagrams obtained from the simulation and those obtained from experimental investigations carried out by Oosterveld [22] in 1970, will be undertaken. As the computational model does not account for the friction that occurs inside the gap between the rotating propeller's ring and the nozzle, a certain underestimation of torque is expected to be observed. These offsets are attributable to the above mentioned neglect of friction between rim and nozzle and therefore handled by mathematical models separately.

2.1 Reference design

In [22] a valuable source of experimental data on tip-driven thrusters can be found. In chapter 9 of the dissertation, a series of ring propellers with their ring countersunk in a nozzle surrounding the propeller, has been evaluated. The thruster investigated features the MARIN nozzle 19A (see figure 2.3), surrounding a Ka 4-70 propeller (figure 2.1). The experiments cover 5 different ratios of P/D ranging from 0.6 to 1.4. Out of those the variant of $P/D = 0.8$ is chosen to be investigated. In the following sections, detailed geometry data will be given, as the procedure of geometry generation for each component of the thruster is covered.

2.1.1 Blades according to table of offsets

Oosterveld [22] gives a table of offsets of the examined Ka 4-70 propeller, which serves as the basis for implementing a parametric model of the propeller. The original table can be found in the appendix B. An approximation of the suction and pressure side sections, based on a least squares approach, was carried out using a cubic B-Spline defined by 6 control vertices. The blade sections have a sharp trailing edge and a simple script was used to achieve a smooth fitting leading edge. As no radius data is given in the table, the leading edges of the given sections are fitted individually. The above mentioned B-Spline curves defining the pressure and suction side of each section range from the sharp

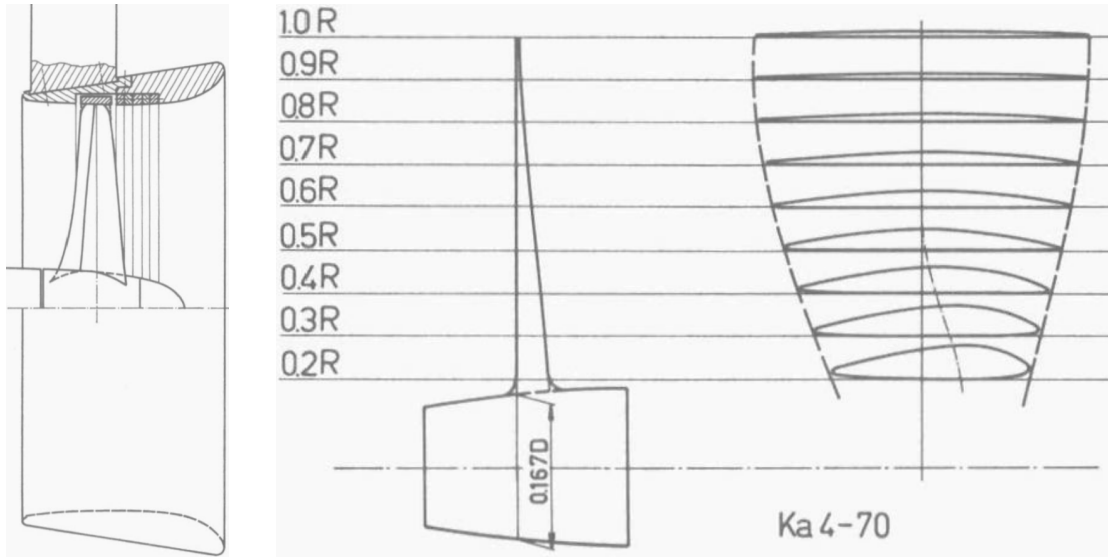


FIGURE 2.1: Particulars of Ka 4-70 ring-propeller series in nozzle 19A, given in [22].

trailing edge up to 95% of the interval between the maximum thickness position and the leading edge. The remaining gap at the leading edge is then closed by a cubic B-Spline, defined by 4 control vertices. The two control vertices at the ends are matching the free ends of the pressure and suction side sections to ensure C^0 continuity. The remaining two control vertices are positioned such that C^1 continuity is ensured. The figure 2.2i shows an example of the resulting curve closing the leading edge gap for the section at $r/R = 0.3$. As can be seen, the transition between the three curves meets C^1 continuity requirements because the control vertices p_1 and p_2 are positioned along the tangents of the suction and pressure side curve ends, respectively. One can see, that the blade tip does not match the given leading edge point. By moving the points p_1 and p_2 independently along the tangents t_1 and t_2 , a solution ensuring the matching of the blade tip and the given control vertex can be found. However, by making this an exact match, it was found, that the transition from one section to the next is rather poor. To overcome this issue, the following 3 steps are executed twice in a row:

- The points p_1 and p_2 are moved incrementally along the tangents in the same chord-wise direction towards p'_1 and p'_2 , to ensure the correct length of the section as shown in figure 2.2ii.
- The points are now incrementally moved in opposite directions along the tangents, until the z coordinate of the blade tip matches the given value (see the points p''_1 and p''_2 in figure 2.2iii).
- As the previous shifting of the points changed the chordwise position of the blade tip again, the points are now moved incrementally in the same chordwise direction again until the correct length is restored (see p'''_1 and p'''_2 in figure 2.2iv).

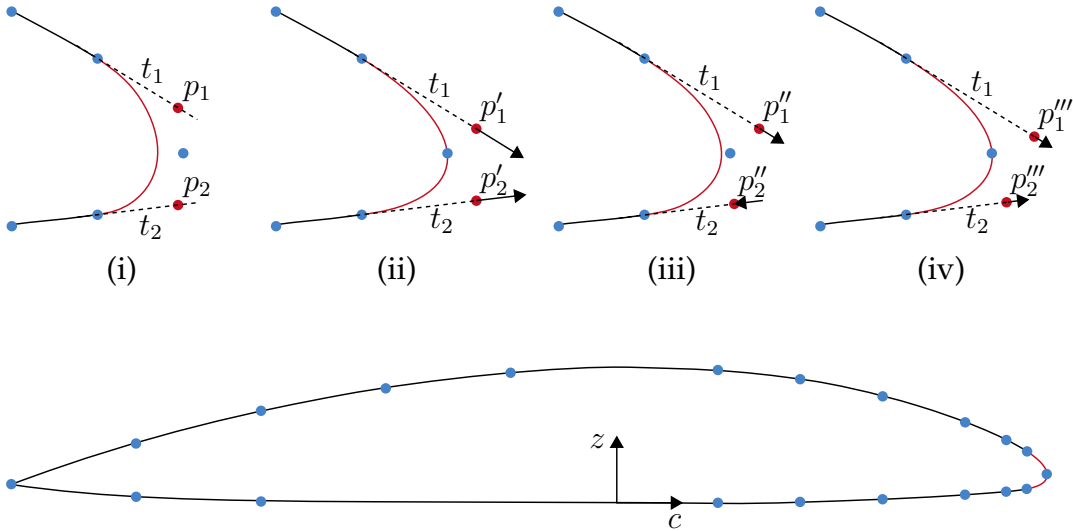


FIGURE 2.2: The upper images (i) to (iv) show the iterative procedure of the leading edge fitting. The profile in the bottom picture shows the resulting closed section at $r/R = 0.3$ and the orientation of the z - and chord-wise coordinate c .

The last step of this procedure ensures the correct length of each section, but again changes the z coordinate to some degree. If the loop was executed an infinite number of times, the blade tip would match the exact given point. By executing it only twice, the transition between the sections is found to be much smoother and the resulting sections are now fed into the surface generation process. A parameter P , controlling the propeller pitch, is introduced and the angle of attack $\alpha(r)$ of each section is changed according to this parameter. At each local radius r the corresponding angle of attack can be calculated as

$$\alpha(r) = \arctan\left(\frac{P}{2\pi r}\right). \quad (2.1)$$

A cylinder transformation is applied to every given section, wrapping it around a cylinder with the same radius as the sections local radius r . The sections are scaled by a factor of 0.125 as the experimental data is based on a propeller with a diameter of $D = 250\text{mm}$ and the working unit for the CAD, as well as the simulation, is set to meters. Via skinning the final surface of the propeller blade is created and extrapolated in radial direction, to ensure a watertight connection towards the hub and rim of the propeller. The given variable fillet radius connecting the blade and the hub is neglected, as this simplifies the meshing process significantly and should not influence the results considerably.

2.1.2 Blades according to given figure

The process of blade generation described in the previous section led to sections varying slightly from those given in figure 2.1 by Oosterveld. The most obvious difference is the trailing edge radius present in the drawing, but also a small

mismatch in the curvature of the suction and pressure side can be observed when examined closely. To gain a quantitative knowledge on how much a possibly dissimilar blade geometry would affect the simulation results, a second propeller blade geometry is generated. The figure 2.1 is imported into a vector graphics tool and the sections from $r/R = 0.2$ to $r/R = 1$ are retraced, using B-Spline curves. The resulting curves are then saved in Drawing Interchange File Format (DXF) and imported into CAESES for further use. The length of one section is determined and a scaling is applied to all of them. Following this, the same steps as described in 2.1.1, involving cylinder transformation, setting the pitch, skinning and extrapolating the surface, are executed to generate a parametric blade. A simulation of each thruster, purely distinguished by the two versions of distinct blade geometries, is performed. A significant difference in performance can be observed, when comparing the two different blade geometries to each other. The results of the geometry derived from the given table are in good agreement with the experiments, while the compared geometry derived from the drawing leads to an offset in the resulting measures. Hence, the first mentioned version will be used for further investigation and the reliability of the correct blade geometry of the Ka4-70 propeller is assured. The propulsive characteristics obtained from the simulations will be presented in detail in chapter 3.

2.1.3 Hub

The radius of the hub used during the experiments is given by Oosterveld as $R_{hub} = 0.0835D$. The exact profile of the hub however, is missing and can only be seen in figure 2.1. It is therefore necessary, to extract the shape of the hub from the given drawing. This is done in a very similar fashion as it was done with the blade sections previously. The hubs cross section is imported into a vector graphics software and the image horizon is corrected. Afterwards, the scaling is determined by comparing known values such as the propeller radius. Vertical grid lines are overlaid to set up equidistant ordinate values. A list of measurements can then be obtained which were recorded in table 2.1 for reproducibility. The exact position of the propeller inside the hub can be determined and is found to be at $0.1821D$ in direction of inflow. Using these values, a spline can be fitted and act as a profile for the rotational hub surface which can be seen in figure 2.4 among with the nozzle and blades.

2.1.4 Nozzle

The nozzle investigated by Oosterveld in [22] is a standard MARIN Nozzle 19A. A detailed description of the geometry can be found in [21] and is shown in figure 2.3.

The profile can easily be generated from the given drawing and scaled to the correct dimensions. A rotational extrusion leads to the final geometry used in the thruster assembly. As Oosterveld [22] suggests to keep the surface area of the rotating propeller ring as low as possible, a part of the nozzle's inside will

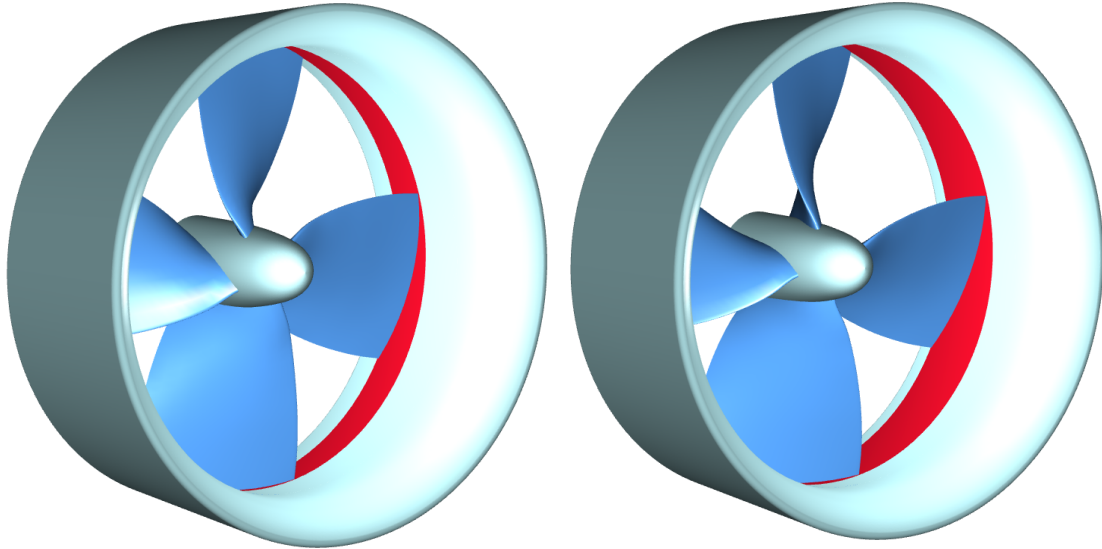


FIGURE 2.4: Parametric model of the nozzle, hub and blades showing ratios of $P/D = 0.8$ and $P/D = 1.4$. The rim length is adjusted with pitch to minimize frictional losses. During the experiments carried out by Oosterveld the variable rim length has been achieved through changeable spacer rings.

into two separate volumes. The first one containing the propeller, as well as the hub and ring, will be referred to as the propeller region from now on. The second one, containing the remaining computational domain and the nozzle, consequently will be denoted as the domain region. In a first step, the entire computational domain will be separated into 4 rotational symmetric regions. This procedure is essential to be able to take advantage of the rotational symmetric flow expected and thus cut computational costs by solving only a 90° region of the flow. Hereby it is helpful, to define the intersecting surface in such a way that the transition between the hub and the intersecting surface includes an angle close to 90° . This will make it easier in the following meshing process to grow a high quality boundary layer off of the hub into the propeller region. The same applies to the transition between the intersection surface and the rim. The intersecting surface should follow the pitch of the propeller in the near-hub region, to allow for splitting up propellers with higher ratios of P/D without cutting the blades. The rim itself should be cut almost perpendicular. If the intersection was to follow the propeller pitch at the rim as well, the resulting surface mesh would incorporate very low angles of (depending on the pitch) down to $< 10^\circ$ and hence, not allow for a high quality volume mesh. The domain is cylindrical in shape and the initial size is set to $D_D = -4D \leq x_0 \leq 6D$, where D is the propeller diameter, D_D the domain diameter, $x_0 = 0$ the position of the propeller plane and the free stream velocity is pointing towards positive x .

2.2.1 Separating the propeller region

After cutting out the 90° region as described above, the rotating part of the volume needs to be separated. The width of the propeller ring is set to match the area covered by the rotating blades, varying with the specified ratio of P/D . As this can again lead to grid elements of bad shape in terms of low angles close to the blade tips, an additional length of $0.016R$ is added on either side of the ring. Figure 2.5 shows the surface mesh of the rim and hub, and the upper detailed view shows the possibility of generating highly orthogonal grid elements due to the additional space around the blade tip.

A circular conical surface is then defined at each end of the rim with its tip located on the axis of rotation of the propeller. On the upstream side, this cone includes an opening angle of 120° at the tip. This ensures an angle of no less than 60° between the cone and the nozzle which is important for generating a hexahedral grid in the domain region, later on. A higher opening angle would be even better as it would allow the domain region's hexahedrals to be even closer to a perfect 90° angle. However, as the propeller region needs to accommodate the hub, as well as the boundary layer mesh grown off of it, it does not allow for a higher opening angle. On the outlet side no such restrictions appear and the opening angle is therefore set in such a way that the propeller domain only just includes the rear end of the hub.

2.2.2 Treatment of near-wall cells

The propeller region contains 4 surfaces which will be defined as walls in the simulation setup. These are the hub, the two faces of the blade and the rim. The domain region adds the nozzle surface to this list. As a $k-\omega$ -SST turbulence model will be applied during the simulation, along with a wall function, special attention needs to be paid to the volume mesh in close proximity to these walls. To avoid incorrect modeling of the buffer layer and laminar sub-layer, the near-wall spacing needs to satisfy certain criteria.

For each advance coefficient J , a non-dimensional wall distance value $Y+$ can be estimated beforehand, depending on the relative speed of fluid along the surface and the distance of the near-wall cell-faces to the wall. The table 2.2 shows the estimated values based on wall distances of $y = 1 \text{ mm}$ at the hub, $y = 0.2 \text{ mm}$ at $0.7R$, $y = 0.15 \text{ mm}$ at $1R$ and $y = 3 \text{ mm}$ at the nozzle. Based on this table, the initial mesh is generated and the actual $Y+$ values occurring during the simulations can be adjusted by applying small changes to the mesh. The aim was, to generate a mesh allowing to simulate the full range of advance coefficients $[0 \leq J \leq 0.7]$, while keeping $Y+$ within the range of $[15 \leq Y+ \leq 200]$. The $Y+$ values actually observed during the final open water test simulation, are given in the following table 2.3. Good practice usually involves a variation of $Y+$, to ensure the model is working correctly and the results are not distorted due to the boundary layer cells being positioned too close or too far away from the wall. However, as the spreading of $Y+$ is rather large during the actual simulation, no such study is carried out, as this would lead to a significant amount of near-wall cells exceeding the limits of $[15 \leq Y+ \leq 200]$. The growth rate

of the boundary layer cells varies from 1.1 to a maximum of 1.25 for a smooth transition away from the walls. A minimum of 10 – 20 layers is ensured which is considered sufficient for a wall-function mesh.

J	v_a in m/s	$Y+$ at hub	$Y+$ at $0.7R$	$Y+$ at $1R$	$Y+$ at nozzle
0	0	33.06	37.46	38.81	–
0.1	0.179	34.45	37.46	38.80	35.94
0.2	0.357	38.21	37.46	38.74	65.77
0.3	0.533	43.55	37.46	38.65	93.65
0.4	0.706	49.74	37.46	38.52	120.11
0.5	0.875	56.32	37.46	38.37	145.33
0.6	1.04	63.01	37.46	38.18	169.35
0.7	1.2	69.65	37.46	37.97	192.21

TABLE 2.2: Estimated non-dimensional wall distance $Y+$ for a range of given advance coefficients J and speeds of advance v_a at different radial positions.

J	$Y+$ at hub	$Y+$ at blade	$Y+$ at rim	$Y+$ at nozzle
0	31.67	27.93	43.29	18.28
0.1	31.26	27.56	43.33	19.00
0.2	31.22	27.18	43.05	20.07
0.3	31.53	26.98	42.81	20.47
0.4	32.10	26.86	42.87	20.83
0.5	32.88	26.73	42.73	21.48
0.6	33.65	26.55	42.27	23.15
0.7	34.39	26.33	41.63	24.62

TABLE 2.3: Average non-dimensional wall distance $Y+$ at given combinations of advance coefficient J and speed of advance v_a during the open water test simulations.

In order to calculate $Y+$ for a given near-wall spacing y at a specific radial position, the Reynolds number is calculated as

$$Re_x = \frac{v_{vec} l_x}{\nu} \quad . \quad (2.2)$$

For The length l_x , the chordlength $l (r/R = 0.7) = 89.04 \text{ mm}$ is used and the actual tangential velocity v_{vec} at any radial position is estimated via vectorial addition of the speed of advance and the rotational velocity as

$$v_{vec} = \sqrt{v_a^2 + (0.7\pi n D)^2} \quad . \quad (2.3)$$

The last column of table 2.2 is calculated using $v_{vec} = v_a$, as the nozzle itself does not rotate. The skin-friction can be calculated according to the Schlichting skin-friction correlation

$$C_f = (2\log_{10}(Re_x) - 0.65)^{-2.3} \quad (2.4)$$

and the wall shear stress as

$$\tau_w = \frac{1}{2}C_f\rho v_{vec}^2 \quad . \quad (2.5)$$

This leads to the non-dimensional wall distance value

$$Y_+ = \frac{yu_*}{\nu} \quad (2.6)$$

with the friction velocity

$$u_* = \sqrt{\frac{\tau_w}{\rho}} \quad . \quad (2.7)$$

The physical constants $\rho = 998.21 \text{ kg/m}^3$ and $\nu = 1.004e^{-6} \text{ m}^2/\text{s}$ are chosen to match the properties of freshwater at 20°C .

2.2.3 Grid generation of propeller region

For the propeller region, different meshing approaches and grid topologies have been compared. While the simulation of the reference design does not yet ask for an automatic grid generation, some considerations related to this upcoming task are already spent at this point. All the meshing within this thesis was done using the commercial grid generator Pointwise. While a manual meshing approach is sufficient for the reference simulation, the optimization task asks for some way of automatic grid generation. Through the use of glyph scripts, Pointwise enables the user to achieve the level of automation necessary for this task.

A first meshing approach is based on structured surface meshes on the two blade faces. An extrusion is carried out off, of these surface meshes with the boundaries set to match the adjacent hub and rim. This extrusion does not cover a significant volume and is mainly created to ensure a sufficient number of boundary layer cells near the blade and the desired near-wall spacing values. The remaining region of the hub is then resolved by an unstructured grid of triangles and extruded as well. Hereby the inner boundaries are set to match the adjacent grid created by the previous extrusion. The remaining 3 boundaries are set to match the adjacent surfaces separating the propeller region. In a similar way the rim is handled. Unstructured triangles are added to the remaining surfaces and the rest of the volume of the propeller region is resolved, using tetrahedral elements. A few important benefits are gained by setting up the mesh this way. Growing a volume mesh, incorporating a boundary layer

off a surface, does not usually involve many difficulties. In this particular case however, some difficulties arise from the presence of adjacent wall surfaces, namely the hub, blades and ring. Growing a volume mesh out of these corners often leads to the collision of cells. This will stop the extrusion and the arising gaps will be filled with tetrahedral elements afterwards, which are likely to be low angled and highly skewed. Occasionally it is therefore necessary to carry out slight adjustments around these critical areas, which involves checking the mesh quality and applying manual changes to the surface mesh. By generating the boundary layer mesh separately from the volume mesh, changing the wall spacing and grading of the boundary layer mesh becomes a very simple task once the first mesh is compiled. This allows for easier adjustments of the near-wall spacing when fine tuning the Y^+ values.

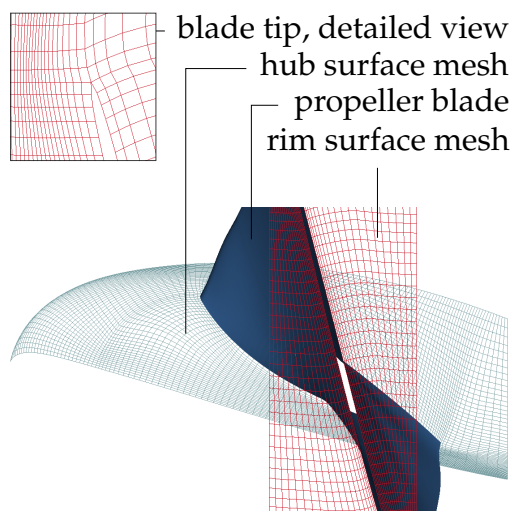


FIGURE 2.5: Top view of the $1/4$ section of the propeller region. The mesh parameterizations of the rim and hub surfaces run almost perpendicular. Thus, the volume mesh of the propeller region can not be generated as a single block-structured grid.

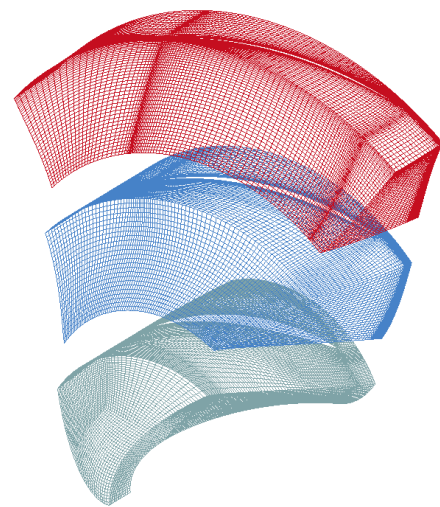


FIGURE 2.6: The exploded view of the propeller region mesh shows the 3 separate block-structured grids. The correct exchange of solution information at the adjacent, non matching grids, is ensured via an interpolation algorithm.

As pointed out before, a fully automatic mesh generation process is desired for the following optimization. Hence a slightly more time consuming way of generating the mesh is chosen. Although the above described procedure enables the user to easily change the parameters of the boundary layer mesh, it does not perform well, when it comes to automated grid generation of changing propeller geometries. Furthermore, a large number of designs will be evaluated during the upcoming optimization and hence, reducing computational costs becomes an important factor. A fully hexahedral mesh is therefore chosen as this type of mesh reduces the overall cell count compared to the use of polyhedral elements [28]. The basic problem of resolving the propeller region using a block-structured grid of hexahedrals is the twist of the blades in radial

direction. Figure 2.5 shows the structured surface meshes on the hub and rim surfaces and the problem arising from the blade pitch, can be seen. The grid lines at the hub run from the blade towards the left and right cutting edges of the hub and perpendicular. At the rim however, the grid lines run from the blade towards the front and back of the propeller region and perpendicular. The parametrization of the two surface meshes is thus opposite and the generation of a high quality volume mesh resolving the whole propeller region based on these grids is considered improbable due to the resulting twist in the volume mesh.

This issue can be overcome by splitting the propeller region into multiple parts with adjacent, non matching grids. An interpolation between these grid interfaces ensures correct exchange of solution information during the simulation. By splitting the propeller region into 3 different parts, the generation of a fully block-structured grid of very high quality cells becomes much easier. This offers the robustness in generating meshes of constant high quality that is needed for the upcoming automatic grid generation in the optimization process. Figure 2.6 shows an explosion view of the 3 separate parts of the propeller region mesh.

2.2.4 Grid generation of domain region

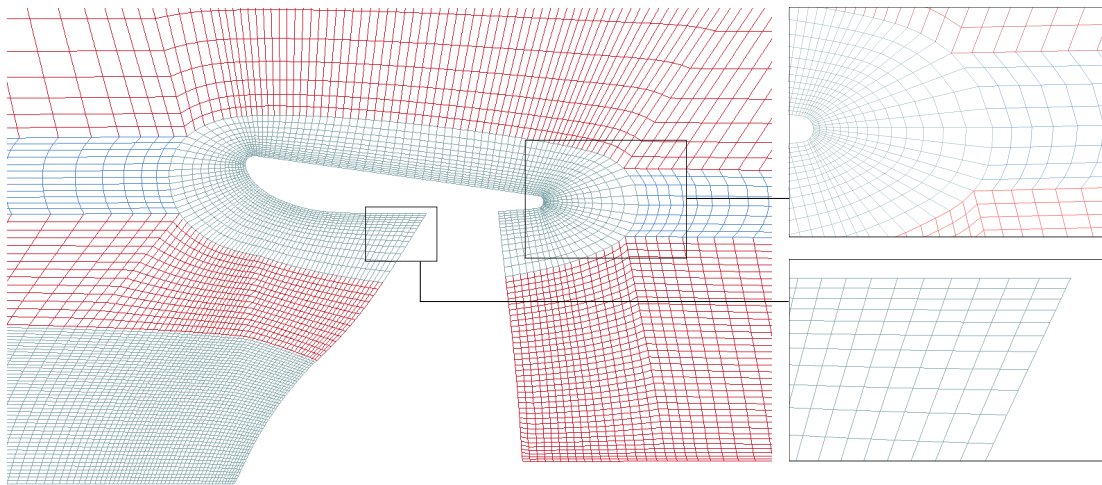


FIGURE 2.7: Surface mesh on the intersection surface of the domain region. The detailed views on the right show the meshing strategy chosen to provide maximum orthogonality in the grid. Note, that only the area close to the thruster is shown, as the general topology does not change further away towards the outer domain boundaries.

Because of the domain shape being a lot less complex than the propeller region, an ordinary block-structured grid can be generated for this region. The cutting surface, used to trim the cylindrical domain into a quarter section, will be discretized into quadrilateral elements and a rotational extrusion around the rotation axis of the propeller will then generate the volume mesh. The surface is therefore split into parts, defining the surface-mesh topology. A part of the overall intersection surface is shown in figure 2.7, showing the separation into

different subsurfaces as indicated by distinct colors. Note, that only the area close to the propeller domain is shown, as the topology does not change further away towards the outer domain boundaries.

The gray colored part in the bottom left corner will be handled later on, as it includes the axis of rotation. Generating a volume mesh by means of a rotational extrusion using this surface would lead to hexahedral elements degenerating down to triangular prisms at the axis of rotation. Behind the propeller no such special attention is needed as the shaft adds the necessary offset towards the axis of rotation. To all other regions a simple H-grid topology will be applied, keeping in mind the necessary near-wall spacing at the nozzle as well as the overall cell count.

In the bottom right detailed view, elements comprising a minimum included angle as low as 60° can be seen as dictated by the cone separating the propeller region described in 2.2.2. Two blue narrow subdivisions are added in front and aft of the leading and trailing edge of the nozzle. The points of intersection between their edges and the adjacent topology are chosen with respect to high orthogonality of the cells. The detailed view in the top right of figure 2.7 shows these critical areas and two grid lines, creating 3 equal 60° angles at every node, can be estimated. The angles indicated by the four grid lines leading towards the upper and lower domain boundaries are easily controlled through the grid point spacing applied to those edges. The final surface mesh can now be rotated by 90° to create the volume mesh extrusion that discretizes the majority of the domain region.

The above mentioned surface depicted in gray will be excluded from this process for the given reason. Instead, the triangular surface towards the propeller region that remains uncovered after the extrusion process will now be addressed. A point, approximately in the center of this triangular surface, is created and 3 gridlines, connecting this point and the center of the surface edges, are added. This leaves the surface divided into 3 quadrilaterals which can again be handled using a simple H-grid. After applying a smoothing solver, the triangular surface is ready for the extrusion. In this case, a translational extrusion is applied, matching the adjacent gridlines of the already existing volume mesh and stopping at a plane, normal towards the direction of extrusion, located at the domain inlet.

2.3 Simulation setup

To simulate the experimental setup followed by Oosterveld [22], a CFD simulation will be conducted using OpenFOAM. The experimental results are available in the form of open water diagrams showing the usual curves of K_T , $10K_Q$ and η_O . Out of the 5 different ratios of P/D investigated by Oosterveld, the $P/D = 0.8$ geometry is chosen to be simulated. The arbitrary mesh interface (AMI) functionality of OpenFOAM allows for conservative interpolation between volume meshes based on the algorithm described by [9]. Using AMI boundaries allows the simulation across disconnected, adjacent mesh domains and is used in two different ways throughout this thesis.

domain region	boundary condition in OpenFOAM	initial condition U	initial condition P
inlet	patch	fixedValue	zeroGradient
outlet	patch	zeroGradient	fixedValue
left, planar part	cyclic	cyclic	cyclic
left, non- planar part	cyclicAMI	cyclicAMI	cyclicAMI
right, planar part	cyclic	cyclic	cyclic
right, non- planar part	cyclicAMI	cyclicAMI	cyclicAMI
to propeller, suction side	cyclicPeriodicAMI	cyclicAMI	cyclicAMI
to propeller, pressure side	cyclicPeriodicAMI	cyclicAMI	cyclicAMI
nozzle	wall	fixedValue	zeroGradient
jacket	patch	fixedValue	zeroGradient
shaft	wall	fixedValue	zeroGradient
propeller region			
to domain, suction side	cyclicPeriodicAMI	cyclicAMI	cyclicAMI
to domain, pressure side	cyclicPeriodicAMI	cyclicAMI	cyclicAMI
left	cyclicAMI	cyclicAMI	cyclicAMI
right	cyclicAMI	cyclicAMI	cyclicAMI
rim	wall	movingWallVelocity	zeroGradient
hub	wall	movingWallVelocity	zeroGradient
blades	wall	movingWallVelocity	zeroGradient
3 separate parts, (see figure 2.6)	cyclicAMI	cyclicAMI	cyclicAMI

TABLE 2.4: Applied boundary and initial conditions for velocity U and pressure P .

Because of the domain being only a quarter section of the whole geometry, a cyclic boundary condition between one side of the section and the rotational symmetric partner surface needs to be applied. This behavior can generally be achieved, using the `cyclic` boundary condition provided within OpenFOAM. If the two coupled meshes do not match each other, or if the geometry is not a planar surface, the much more powerful `cyclicAMI` boundary condition can be used. The AMI algorithm accounts for partially overlapping faces by defining the fraction of the intersecting areas as weights. A sum of weights close to 1 shows a good geometric match with little conservation errors introduced. Single faces with very poor matching often occur close to geometric features like edges and discontinuities. If they are only a few in number, they can be handled using the `lowWeightCorrection` command which applies a zero

gradient condition to these particular cell faces.

The interfaces between the rotating propeller region and the static domain are also handled by the AMI algorithm. This is, where the ability of handling non-conforming patches becomes particularly beneficial. Simulating only a section of the rotational symmetric domain adds further requirements to the interpolation. With the OpenFOAM version v3.0+ a new boundary condition named `cyclicPeriodicAMI` has been introduced. The algorithm calculates the overlap between the wedge-like boundaries sliding along each other. If there are non overlapping regions remaining, a transformation, based on the transformation of another pair of coupled patches, is performed and the remaining overlap is calculated. This procedure is repeated until the overlap is found to be complete, or a given number of iterations is reached. This procedure allows even for one patch-section to be an integer multiple of the other.

The left and right boundaries of the static region are split into a planar surface with conformal surface-meshes on the left and right and a non-planar part with non-conforming meshes. The reason behind this is that the boundary condition `cyclicPeriodicAMI` requires a `periodicPatch` for the calculation of the transformation necessary to compute the remaining overlap. It was found in a first approach that setting the `periodicPatch` given within the declaration of `cyclicPeriodicAMI` boundaries to type `cyclicAMI` causes OpenFOAM to use an internal algorithm for the calculation of the necessary axis and center of rotation. This caused erroneous behavior as the algorithm failed to calculate the correct transformation vectors. The reason for this is presumably the fact that the calculations are based on the orientation of a single face-normal. Using a non-planar surface as the `periodicPatch` seemed to cause the algorithm to fail systematically and lead to convergence problems showing in oscillating forces acting on the thruster components and high residuals. Separating a set of planar, conformal meshed parts from the left and right `cyclicAMI` patches and setting them to `cyclic` solved the convergence issues as this ensures the transformation vectors being calculated correctly.

An overview of the applied boundary conditions, and the initial values of pressure and velocity can be found in table 2.4. Detailed information on the mathematical schemes and solution settings can be taken from the `fvSchemes` and `fvSolution` files within the digital appendix given with this thesis.

As can be seen from the `controlDict` file within the system folder of the appendix, `pimpleDyMFoam` is used as a solver. The solver is based on a merged PISO-SIMPLE, hence the term 'PIMPLE' algorithm and capable of dynamic mesh ('DyM') handling. From the SIMPLE algorithm comes the advantage of relaxation factors which speed up convergence towards steady-state condition. The actual PISO mode is time conservative but takes a lot of CPU time for complex problems due to its limitation to Courant Numbers $Co < 1$. Therefore, within a PIMPLE loop, the pressure-momentum coupling is calculated multiple times. Hereby, relaxation is used within all but the last iterations which allows smooth convergence at $Co > 1$ with a solution that is accurate in time and space.

Although in general a steady-state solution is expected, the use of this solver

allows to observe possible transient behavior of the flow such as unsteady separations. The number of iterations is set to a high maximum value and within the `fvSolution` file the `residualControl` keyword allows to specify earlier exit criteria based on the initial pressure and velocity residuals. When monitoring the simulations, the residuals along with the forces and momentums are examined to judge convergence as will be explained in the following chapter [3](#).

Chapter 3

Verification of reference simulation

To ensure reliable results and a good match of the simulation and experiments carried out by Oosterveld, a number of studies is carried out. The resulting total thrust is used as a measure to observe the solutions dependence on different factors. The aim is, to either find the necessary settings that ensure the solutions independence or to quantify the deviation caused by each factor individually. The settings chosen to be sufficient for the further investigations are not solely depending on a specific tolerance but also chosen with respect to the computational costs they induce.

With all these general preferences of the simulation set, residuals and forces are monitored closely to ensure the solutions accuracy and sufficient level of convergence. Grid quality is monitored and solver settings are adjusted to reach satisfying results.

3.1 Domain size and number of revolutions

The overall domain is of cylindrical shape, specified by a certain inlet- and outlet-length l_i and l_o measured from the propeller plane and a domain-radius R_D with the propeller rotation axis being collinear with the center axis of the cylinder. Researching the literature shows various estimations on the necessary size of the computational domain. In [26], [30] and [32], domain sizes of $3R \leq l_i \leq 6R$, $7R \leq l_o \leq 18R$ and $2.8R \leq R_D \leq 8R$ are found. In [8] the authors also show the results not changing after extending the overall length of the domain from $16R$ to $40R$ and the radius from $12R$ to $16R$.

As the given estimations are as distinct and none of the cited work focuses on ducted or rim-driven propellers in particular, an analysis on the necessary domain size is carried out. Simply choosing the greater of the above given values is not sufficient as well, as computational costs shall be kept low with the large number of simulations upcoming in mind. The 3 measures l_i , l_o and R_D are altered individually to make sure, no potential is lost. While altering the expansion in one direction, the other two are kept at the constant reference values $l_i = 6R$, $l_o = 10R$ and $R_D = 7R$. The overall cell count of the mesh at these reference settings equals around $1.2e6$ and changes as the domain size is expanded or reduced during the study.

The simulations are performed at a local Reynolds number of $Re_{0.7} = 3.5e5$ and a time step resolution of 140 steps per revolution with $Re_{0.7}$ being calculated according to the equations (2.2) and (2.3). As the development of recirculating flow affects the solution and is considered to happen more likely at low advance coefficients, the simulations are performed at bollard pull $J = 0$.

From $J = 0$ and the definition of the advance coefficient

$$J = \frac{v_a}{n \cdot D} \quad , \quad (3.1)$$

follows: $v_a = 0 \frac{m}{s}$. Hence, equation (2.3) simplifies and (2.2) can be solved for the number of revolutions

$$n = \frac{Re_{0.7} \cdot \nu}{l_{0.7} 1.4\pi R} = 7.178 \frac{1}{s} \quad . \quad (3.2)$$

Before comparing the results of the different domain sizes, the number of propeller revolutions n_{rev} that are simulated needs to be defined. A number of variables need to be monitored when deciding on the level of convergence a solution has reached. Besides controlling measures such as pressure losses over the domain and residuals of the solution, the forces and moments acting on the geometry are another important measure. When checking for convergence, a steady state behavior of the resulting forces acting on the thruster unit is expected to be reached after a sufficient number of time steps. This criteria is used to decide on the minimum number of simulation steps needed to obtain valid results.

A total number of 9 revolutions is simulated at the given reference values for l_i , l_o and R_D and the normalized total thrust is shown in figure 3.1. The advance ratio in this case is set to $J = 0.5$ with $v_a = 0.875 \frac{m}{s}$ and $n = 7 \frac{1}{s}$ to maintain $Re_{0.7} = 3.5e5$ according to equation (2.2). After the simulation of $n_{rev} = 3$ complete revolutions the resulting value does not change significantly any more. The difference in thrust to simulating a total of 4 revolutions is less than 0.14 %. Based on these results, the simulation of a total number of 3 revolutions is considered sufficient.

After this decision on the necessary number of propeller revolutions is made, the investigation on the minimum domain size needed, continues. Figure 3.1 also shows the resulting normalized total thrust depending on the chosen parameters for the domain size after 3 revolutions are passed. Clearly, the inlet length seems to have no effect on the results at all and might be reduced even further without any influence on the thrust. The minimum examined value of $l_i = 4R$ is chosen to be used for the remaining investigations. The outlet length also shows only minimal effect with the difference from $l_o = 8R$ to $l_o = 9R$ being less than 0.4 %. Not knowing about the reason for this step and the progression of the thrust between the examined parameters, an outlet length of $l_o = 10R$ is chosen. As the cells towards the outer domain boundaries are rather coarse, the total cell count is not influenced to much by this rather cautious decision. Out of the three parameters defining the domain size, the radial extent of the domain clearly shows the biggest impact on the results. The change in total thrust

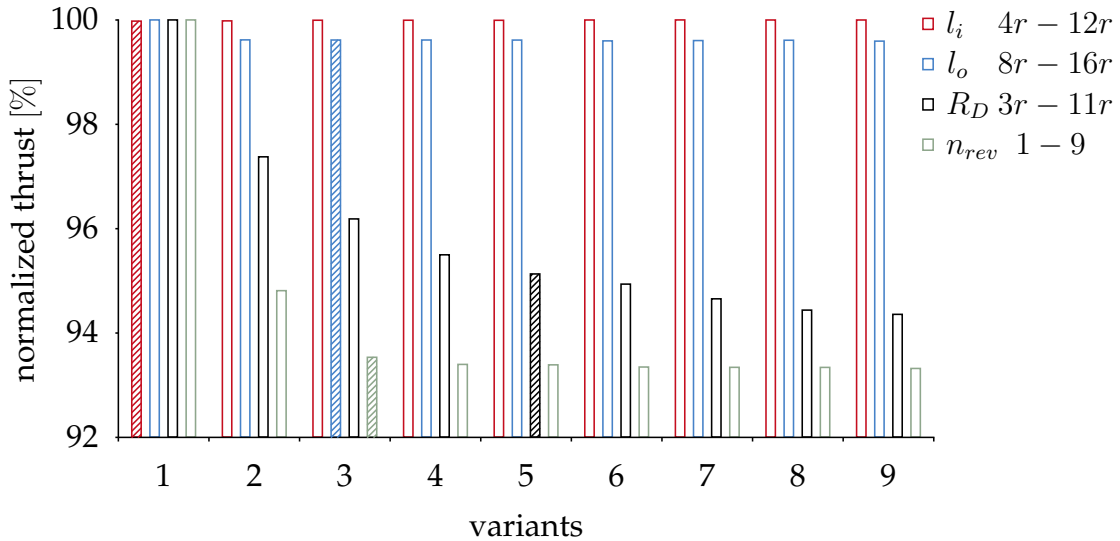


FIGURE 3.1: Dependency of thrust on domain size and number of revolutions. The bars of the chosen values for upcoming simulations are hatched for highlighting.

from $R_D = 6R$ to $R_D = 7R$ is less than 0.4 % and the progression shows an evident convergence behavior. Thus, $R_D = 7R$ is selected from the set without any further safety margin.

3.2 Reynolds number and time discretization

When setting a specific advance ratio J , the user usually has a free choice on the combination of v_a and n , as the three measures are related through equation (3.1). The simulation is set up to match the experiments carried out by Oosterveld as closely as possible. In [22, p. 97] a local Reynolds number at the blade is given as $Re_{0.7} = 3.5e5$ for the performed model tests. Using the equations 3.2 and 3.1, the speed of advance and rotational speed in accordance with the given Reynolds number can be calculated for a given J . However, in [22, p. 96] the experimental routine followed, is described as keeping the rotational speed at a constant value and varying the speed of advance. In the section on ducted propellers, Oosterveld furthermore describes his procedure as choosing the rotational velocity 'as high as possible' and mentions, that advance 'speeds above $v_a = 3 \text{ m/s}$ could not be investigated on account of the towing carriage' [22, p. 26]. These statements allow for different assumptions on how exactly the experiments have been carried out. Sticking to the given Reynolds number of $Re_{0.7} = 3.5e5$, leads to advance speeds in the range of $0 \text{ m/s} \leq v_a \leq 1.2 \text{ m/s}$ and rather low rotational speeds of $6.8 \text{ 1/s} \leq n \leq 7.2 \text{ 1/s}$. If the speed of advance is kept at the maximal feasible $v_a = 3 \text{ m/s}$, rotational speed increases drastically towards $J = 0$. The simulations are therefore set up to match the given Reynolds number at rotational speeds of around $n = 7 \text{ 1/s}$ and a variety of different Reynolds numbers is simulated additionally, to estimate the offset due to a possible misconception. The simulations are carried out for a constant

advance ratio of $J = 0.5$ at

$$Re_{0.7,1} = 3.5e5, \quad Re_{0.7,2} = 7e5 \quad \text{and} \quad Re_{0.7,3} = 10.5e5, \quad (3.3)$$

which leads to

$$v_{a,1} = 0.875 \frac{m}{s}, \quad v_{a,2} = 1.750 \frac{m}{s}, \quad v_{a,3} = 2.625 \frac{m}{s} \quad \text{and} \quad (3.4)$$

$$n_1 = 7 \frac{1}{s}, \quad n_2 = 14 \frac{1}{s} \quad \text{and} \quad n_3 = 21 \frac{1}{s}. \quad (3.5)$$

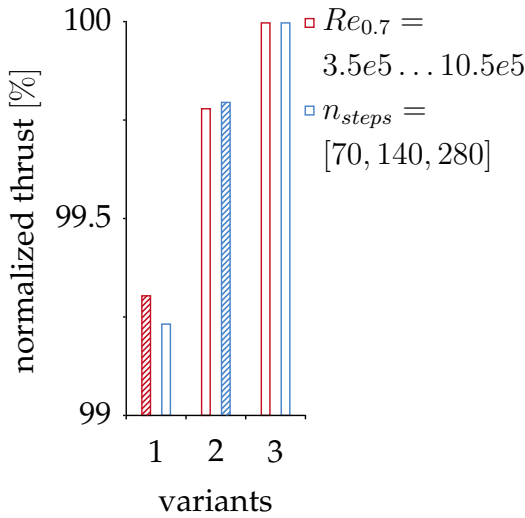


FIGURE 3.2: Effect of chosen time step and Reynolds number on the total thrust. The change in thrust depending on the Reynolds number is not rated as an error, but shows only the possible offset. The bars of the chosen values for upcoming simulations are hatched for highlighting.

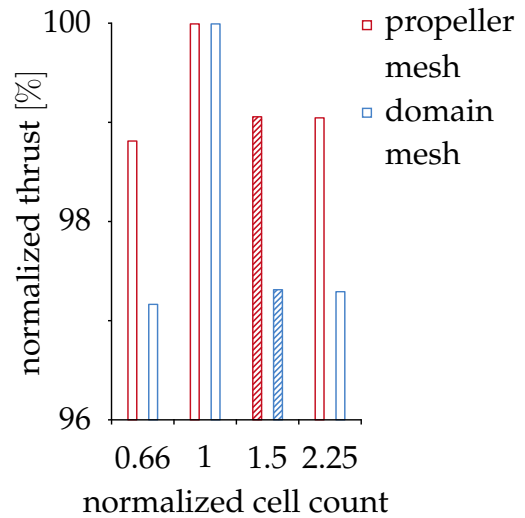


FIGURE 3.3: Study of solutions dependency on mesh resolution. The initial mesh of a normalized cell count equal to 1 consists of approximately $2.5e5$ cells in the propeller region and $7.5e5$ elements in the remaining domain. As in the figure on the left, the values chosen for upcoming simulations are hatched for highlighting.

The results in figure 3.2 show a distinct dependence of the total thrust on the Reynolds number, the uncertainty within the investigated interval is however within less than 1 % and thus not a mayor concern.

When setting up the simulations for the different rotational speeds, one also has to adjust the respective time step to keep the number of time steps per revolution at a constant value. Estimating the time step based on this measure is common practice and a documentation on the influence of the chosen mesh movement per time step can be found in [29]. Comparing the thrust and torque coefficient for mesh movements of 0.5° and 2° per time step, Turunen found the time discretization has significant influence on the resulting measures. Increasing the number of iterations inside each time step in the larger time step

scenario of $2^\circ/\Delta t$, lead to the results converging towards the results based on the smaller time step.

To eliminate this influence, the solver setup in the thesis uses a residual control within the pimple loop which ensures a sufficient number of inner iterations and a constant convergence level that does not depend on the time step. A comparison of the results based on 70, 140 and 280 time steps per revolution is drawn. It is found, that even with the residual control regulating the number of inner iterations, a distinct variation of the resulting thrust occurs for the varying time discretizations. The quantitative results can be found in figure 3.2 and show a significant increase in thrust of almost 0.6 % when refining the time step from 70 up to 140 steps per revolution. A further increase up to 280 steps per revolution still shows a small impact but also increases the computational costs dramatically. As, according to figure 3.2, the potential improvement lies within less than 0.25 %, the discretization of 140 steps per revolution is chosen for the upcoming simulations.

3.3 Mesh resolution

The number of cells during the previous simulations varied slightly due to the various domain sizes investigated. The overall cell count lies at approximately $1e6$ cells with $2.5e5$ cells in the propeller region and $7.5e5$ elements in the domain region. These initial values were chosen, based on similar CFD simulations as in [3] and [26]. However, a variation of the mesh resolution is necessary to verify the correct choice. By varying the resolution of the domain and the propeller region separately, the resulting number of cells might be lower than if both grids are changed at the same time. The number of cells from the coarsest to the finest grid increases approximately by a factor of 1.5 with each refinement. As the entire computational domain is discretized by structured hexahedrals, the number of cells can simply be adjusted by changing the resolution of the grid lines. A change of the initial resolution by a given factor f is achieved by scaling the number of points on each line by $f^{1/3}$. The resulting cell count for all meshes investigated, is given in table 3.1.

mesh	scaling factor f	propeller region	domain region
coarse mesh	0.66	176297	507222
initial mesh	1	271681	761667
fine mesh	1.5	405031	1139855
finest mesh	2.25	608181	1732296

TABLE 3.1: Table of grid resolution, showing the number of cells for each mesh region, depending on the scaling factor.

The results in figure 3.3 show a distinct dependency of the calculated thrust on the discretization of the computational domain. Changing the initial resolution of the domain region to the coarse version, lead to a predicted thrust of

only 97 %, compared to the solution on the initial mesh. A similar trend can be observed, when the initial domain region mesh is kept and the propeller region grid is exchanged for the coarse variant. Although the change in thrust is not as significant as in the previous scenario, the difference still exceeds 1 % and thus, is bigger than any of the cases examined in chapter 3.2. Increasing the number of cells by a factor of 1.5, in both cases leads to a similar change in thrust and thus, does not allow for any assumptions on the correctness of the solution. After a second refinement the results show a surprisingly small change. The difference in thrust from $f = 1.5$ to $f = 2.25$ lies at only 0.02 % for the domain mesh and 0.01 % for the propeller mesh. Although this exceptionally good match is likely to be coincidental, it is indicative that the fine mesh at about $1.5e6$ cells is already adequate for the task at hand.

3.4 Convergence and mesh quality

Despite of the previously outlined studies on the solutions correctness, convergence is a substantial criterion when judging the reliability of simulation data.

The most fundamental measures of convergence of an iterative solution are the residual values of the variables at each iterative step of the simulation. Figure 3.4 shows the residuals for pressure p and axial velocity v_x of the simulation at $J = 0.5$. After the simulation is running for 3 full revolutions, at around -1.5 , the logarithm of the pressure residual is rather high. At less than -4 , the logarithm of the velocity residual is significantly lower. However, both values do not reach a level as low as one would usually expect with a steady-state solution.

Some of the configurations examined throughout this thesis have shown very slight oscillations of the forces, probably related to unsteady flow separations occurring at certain Reynolds numbers. When post-processing those, a mean value of the forces and moments acting on the thruster components is calculated instead of only using the results obtained within the last time step. Transient behavior like this could explain the high initial residuals after each time step of the solution. However, figure 3.5 does not show this kind of behavior for the depicted configuration and thus, the reason for the rather high residuals must be of a different nature.

With each time step of the solution the two parts of the computational domain are rotated relative to each other. As a consequence, an interpolation between the adjacent grid faces needs to be performed. This technique, as it has been described in 2.3 introduces errors into the solution. Those errors mainly arise from very few badly matching cells and the simulation can be kept from diverging by specifying a `lowWeightCorrection` in the `createPatchDict` file. However, these errors are assumed to cause the rather high initial residuals for the first inner iteration of the PIMPLE loops.

When looking at the residuals over all inner iterations, a convergence down to the level specified within `relativeTolerances` and `residualControls` of the `fvSolution` file can be observed. The pressure residual within each Pimple loop drops by approximately one order of magnitude and the logarithm of the

velocity residual drops down to -6.5 . This progression is similar to the behavior one would expect for a transient simulation. Tightening the tolerances should help in further decreasing the residuals inside each Pimple loop. However, it was observed that the results of interest are not impacted significantly and thus, computational costs can be saved by using the `fvSolution` settings as they can be inspected in the digital appendix of this thesis. The tolerances of the residuals for pressure and velocity lead the Pimple loop to exit at about 20 to 30 iterations in the beginning of the simulation and after approximately 10 iterations once 3 propeller revolutions are computed.

As already mentioned in the previous section 2.3, using the Pimple algorithm adds the advantage of allowing large time steps even in case of transient solutions, as relaxation factors can be set. During each calculation of the pressure-momentum coupling within the pimple loop, under-relaxation is used to converge the solution and keep the simulation stable. Only the last iteration is done without under relaxation, as the `final` keywords in the `fvSolution` file are set to 1 to ensure the simulation is time conservative. Furthermore, a number of 2 `nNonOrthogonalCorrectors` is used, to correct the pressure field twice within each inner iteration which was found to help speeding up the simulation. The described setting allows for the maximum Courant number during the simulation to be as high as $Co_{max} = 25$ without causing convergence problems. The overall simulation time for the computation of the open water results given in 3.6 lies at about 25 h, running 8 cases in parallel on a total of 16 cores.

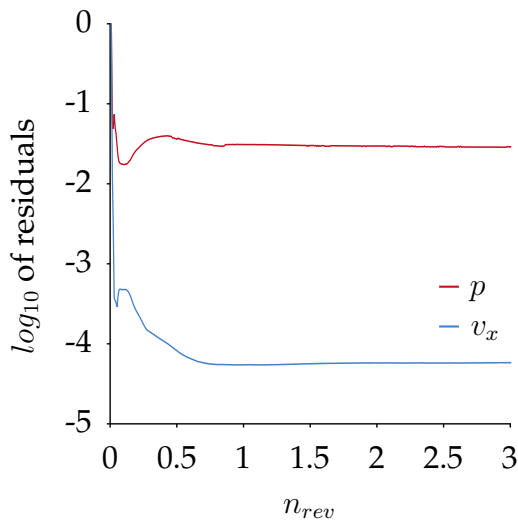


FIGURE 3.4: Initial residuals of p and v_x in first iteration of each pimple loop at $J = 0.5$, plotted against number of revolutions n_{rev} at 140 steps per revolution.

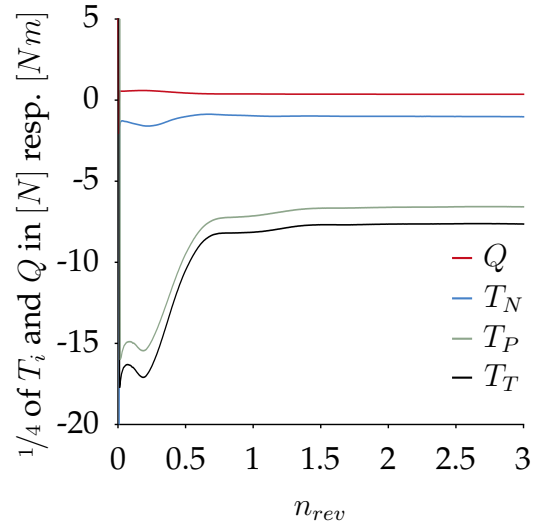


FIGURE 3.5: $1/4$ of propeller torque Q and thrust of nozzle T_N , propeller T_P and total thrust $T_T = T_N + T_P$ at an advance coefficient $J = 0.5$ and 140 steps per revolution.

An other way of judging the solutions convergence is to observe certain measures of interest such as forces or pressure values. In this case, the thrust

generated by the distinct parts of the thruster unit, as well as the torque acting on the propeller, are the most important results. Therefore, the propeller-torque Q is calculated after each time step of the simulation as the sum of the torques, acting on the hub, blade and rim. The thrust of the propeller T_P is calculated analogously as the sum of forces acting on these 3 components in direction of inflow. The nozzle thrust T_N is calculated as the thrust of the nozzle only, without the part acting as the propeller rim. Figure 3.5 shows the thrust and torque acting on the thruster unit and a good level of convergence towards a steady state can be observed after 3 revolutions as already shown in section 3.1. Note that the figure shows the results as obtained during the simulation and thus, the total forces are 4 times higher due to the fact that only a $1/4$ section is simulated.

The conservation of mass, momentum and energy during the simulation needs to be assured and thus, is observed as a third criterion. Monitoring the domain imbalances shows if convergence is reached, as these measures should tend towards 0 once the flow field matches the correct solution. The use of an interpolation across adjacent, non matching domain boundaries, as described in 2.3, caused large conservation errors during the first test setups created. However, by reducing the amount of AMI boundaries and increasing the tolerances during the mesh generation process, these problems could be overcome. At absolute values ranging from $1e - 9$ to $1e - 10$, the global time step continuity errors are well within acceptable limits.

Finally, the mesh quality needs to be kept in mind when judging any CFD results. Apart from the conducted study on the necessary mesh resolution, certain quality criteria have to be monitored during grid generation. Depending on the solver, special attention should be paid to differing measures. The `checkMesh -allGeometry -allTopology` command within OpenFOAM provides substantial information on all crucial quality measures. In table 3.2, the main outputs for the combined propeller and domain region mesh, used for the open water simulations in 3.6, are given. The outputs from the various grids, used during the computations of the previous sections, are not given in detail to narrow the extent of this thesis down at this point. However, all of them were checked during the process and passed the command without any warnings or errors.

3.5 Correction of frictional dissipation

One of the major trade-offs in rim-driven thrusters is the friction occurring between the propeller's ring and the nozzle. Because of the blade tips being directly attached to the ring, the small gap usually present in ducted propellers is avoided. The absence of any unfavorable tip clearance effects increases the efficiency but the existence of the rotating rim, at the same time, adds a considerable amount of friction and thus increases the torque. Oosterveld [22] used a flat plate drag model to estimate the frictional resistance and found the additional torque and the resulting decrease in efficiency outweighs the benefits of the absence of tip clearance effects. He concludes, that the axial extent of the

mesh statistics		quality checks		passed
points	1726366	max cell openness	$4.35e - 16$	✓
faces	5019642	max aspect ratio	44.74	✓
internal faces	4863432	min face area	$3.56e - 8$	✓
cells	1647179	max face area	$4.02e - 4$	✓
faces per cell	6	min volume	$1.37e - 11$	✓
boundary patches	22	max volume	$3.62e - 06$	✓
point zones	0	total volume	1.05	✓
face zones	2	max non-orthogonality	51.95	✓
cell zones	2	average non-orthogonality	16.95	✓
hexahedral cells	1647179	max skewness	1.37	✓
		average coupled	$3.49e - 17$	✓
		point location match		✓
		min edge length	$8.56e - 05$	✓
boundary openness	OK	max edge length	0.03	✓
topology checks	all OK	min face flatness	$99.1603e - 2$	✓
multiply connected	all OK	max face flatness	$99.9995e - 2$	✓
surfaces		min cell determinant	$32.38e - 4$	✓
face pyramids	OK	average cell determinant	$37.25e - 1$	✓
face tets	OK	min face	$22.21e - 2$	✓
angles in faces	all OK	interpolation weight		✓
concave cell check	OK	average face	$49.13e - 2$	✓
face interpolation	OK	interpolation weight		✓
weight check	OK	min face volume ratio	$29.03e - 1$	✓
mesh	OK	average face volume ratio	$96.00e - 1$	✓

TABLE 3.2: Table of mesh statistics and quantitative quality criteria for the mesh used for the open water test simulations.

rim shall be kept as low as possible in order to reduce dissipation down to a minimum.

Further investigations on the flow characteristics inside the gap have been carried out by numerous researchers. Batten, Bressloff and Turnock [1] used RANS equations and a special, low Reynolds number, $k-\omega$ model, to simulate the flow between two concentric cylinders of inner and outer radius R_i and R_o . Their work is not focused on a specific application, but investigates the general flow behavior in the gap between the outer, static and the inner, rotating cylinder. According to Taylor [27], who studied the stability of motion of a liquid in an analogous apparatus, a Reynolds number, based on the gap width d , can be formulated as $Re = vd/\nu$ and the Taylor number $Ta = Re^2 d/R_i$, can be written. Batten et al. performed simulations at various Taylor numbers by varying the outer radius and matched their results against various existing empirical formulas and experimental data. Their findings show the distinct influence of the gap size d and thus the occurring Reynolds number on the skin-friction. Critical Taylor numbers Ta_c are given for all test cases describing the formation of the characteristic array of alternating toroidal vortexes.

Cao et al. [4], recently investigated a thruster unit very similar to the one

present in this thesis. Their work cites Michael [18], dividing the rim's surface into the outer, inner and end-faces. Based on different empirical formulas the frictional resistance of the three parts is calculated separately. In an earlier publication [5], Cao et al. applied a similar empirical rim surface correction and validated their results with an experiment. The more recent publication [4] uses RANSE simulation and an angular momentum current analyzing method to study the effect of the gap flow in a RDT.

The rim's torque is divided into the outer surface and the rim-end faces and more sophisticated empirical formulas are developed to calculate the frictional losses of the system. The torque of the end faces was found to differ significantly from the experimental results of a rotating disk as the simulation resembles the axial gap flow in a RDT much better. Caused by centrifugal forces, a circular flow within the gaps at the end faces is observed, leading to a radial outflow at the rim's end faces and a radial inflow at the opposing duct surface for momentum conservation. Taylor vortexes within the radial gap were observed mainly near the edges which implies a small interference of the radial and axial gap flow. A number of simulations, varying the axial gap ratio while keeping the radial gap at a constant value and vice versa, are performed and the formulas (3.6) and (3.7) are derived. Experiments in a large cavitation tunnel are used for validation and a great improvement in predicting the frictional losses, compared to previous empirical formulas, was found. According to these formulas, the torque of the rim's end and outer surfaces can be calculated as

$$Q_{rim,end} = (-0.001634 \cdot \delta^{-1.003} + 0.2282) Re_r^{-0.25} \cdot \frac{1}{4} \rho \omega^2 R_o^5 \quad \text{and} \quad (3.6)$$

$$Q_{rim,out} = 0.01668 \eta^{-1.818} (1 - \eta)^{-1.757} Re_i^{1.8} \cdot 2\pi l_{rim} \rho \nu^2 \quad , \text{ with} \quad (3.7)$$

$$\delta = \frac{s}{R_o} \quad , \quad Re_r = \frac{\omega R_o^2}{\nu} \quad , \quad Re_i = \frac{\omega R_o h}{\nu} \quad \text{and} \quad \eta = \frac{R_i}{R_o} \quad .$$

These formulas are used, to correct the results obtained in this thesis, and allow for a comparison to the experimental findings of Oosterveld. As no exact measurements of the axial and radial gap clearances s and h are given in [22], a reasonable estimation is done. From the explanations and drawings of the test apparatus used, one can assume, that no bearing is used between the nozzle and ring. The propeller thrust and torque are rather measured the same way as in a conventional open water test setup via the propeller shaft. A bearing accepting axial forces within the nozzle would lead to the propeller thrust being induced into the nozzle and thus not allow for a separate measurement of the nozzle's thrust. Radial forces, acting on the shaft, are taken up by a bearing located between the propeller and dynamometer thus making any bearing within the nozzle unnecessary. This leads to the conclusion that for ease of manufacturing and to ensure no contact is made between ring and nozzle, the axial and radial gaps are rather wide compared to a fluid dynamic bearing. A clearance of $s = 1mm$ in axial and $h = 1mm$ in radial direction is assumed to be reasonable and the additional torque is calculated based on these values. The remaining unknown measures introduced in the equations (3.6) and (3.7),

are the axial length of the rim which can be obtained from the CAD model as $l_{rim} = 0.0297 \text{ m}$ and the outer radius which is $R_o = R_i + h = 126 \text{ mm}$. The rotational speed ω varies with the advance coefficient simulated, the density of the fluid $\rho = 998.21 \text{ kg/m}^3$ and the kinematic viscosity $\nu = 1.004e - 6 \text{ m}^2/\text{s}$ are set in the simulation to match the properties of freshwater in the towing tank at $20 \text{ }^\circ\text{C}$. Keeping in mind that the simulated thrust and torque measures are representing only $1/4$ of the thruster, while the additional $Q_{rim,end}$ and $Q_{rim,out}$ apply for the whole unit, the open water diagram in figure 3.6 can be plotted.

3.6 Comparison of results

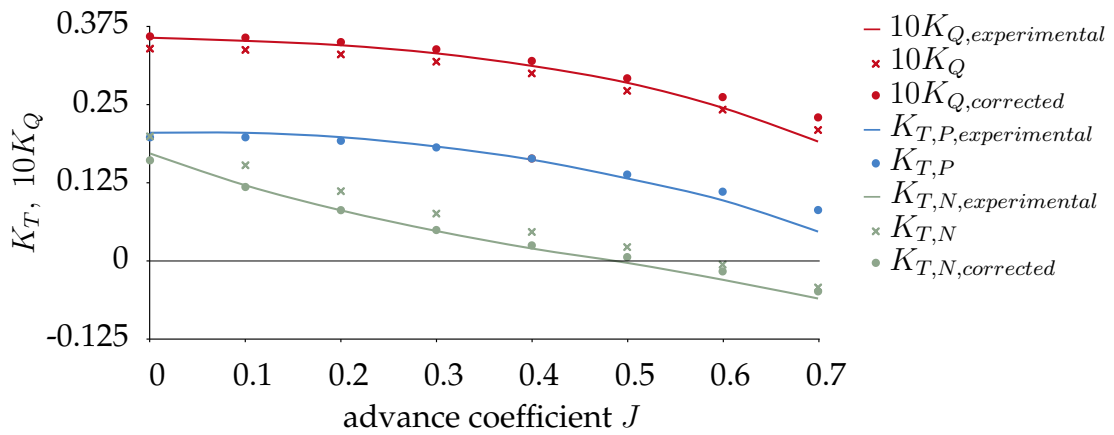


FIGURE 3.6: Open water diagram from [22] and simulation results at $P/D = 0.8$.

In figure 3.6, the open water diagram for the case of $P/D = 0.8$ obtained by Oosterveld [22] is shown. The thrust coefficient is split up into two components, namely the nozzle thrust coefficient $K_{T,N}$ and the propeller thrust coefficient $K_{T,P}$ which add up to the total thrust $K_{T,T} = K_{T,P} + K_{T,N}$. The simulation results obtained in this thesis are plotted in the same diagram. When looking at the propeller thrust, a very good agreement is found, which confirms the correct choice of blade geometry made in section 2.1.2. A small deviation towards higher thrust values at the advance coefficients $J = 0.6$ and $J = 0.7$ can be observed but is negligibly as the following optimization will focus on advance coefficients near the optimum open water efficiency.

A similar trend can be observed when comparing the results of the torque coefficient. In this case, additionally, an underestimation of the torque across the whole range of advance coefficients can be seen. This offset has been anticipated as the consequence of the neglect of friction between the nozzle and rim and is addressed using the empirical models described in the previous section 3.5. The corrected values $10K_{Q,corrected}$ are also given in the figure 3.6 and show a much better fit, although the forces are again slightly high towards higher advance coefficients.

The nozzle thrust appears to be slightly higher than the experimental findings over the whole range of advance coefficients. An approach on correcting

this offset was made, based on the assumption that an axial pressure difference between the suction and pressure side of the propeller acts on the end faces of the gap. No evidence on such behavior could be found in the literature, as Cao et al. [4] used a rotating disk instead of a propeller in their simulations. Hence, no axial pressure drop can be observed in their results. Others, like Batten [1], focused solely on rotating cylinders, without even considering the surrounding nozzle. However, looking at the axial pressure distribution inside the nozzle, a negative contribution to the nozzles thrust can be assumed, as the downstream facing side of the recess is exposed to a lower pressure than the opposing side. The opposite applies to the end faces of the rim. Hence, an increased propeller thrust could be expected on the same basis. As the rim-end faces are smaller in area than the end faces of the nozzles recess, their influence will be neglected. To estimate the force acting on the nozzle based on this theory, the pressure at the edge between the inside surface of the nozzle and the end faces of the recess is exported from the CFD results. The mean values \bar{p}_p and \bar{p}_s around the entire 360° circumference are calculated for the pressure and suction side edges. By multiplication with the respective face areas A_i and subsequent subtraction, the resulting force acting on the nozzle can be calculated as

$$\Delta T_N = A_s \bar{p}_s - A_p \bar{p}_p \quad (3.8)$$

and the corrected nozzle thrust coefficient can be written as

$$K_{T,N,corr} = K_{T,N} + \frac{\Delta T_N}{\rho n^2 D^4} \quad (3.9)$$

The face areas A_i are calculated based on the assumption of a radial depth of the recess of 2.5 mm and the resulting corrected nozzle thrust coefficient is also plotted in figure 3.6. The values are now in much better accordance with the experimental findings which shows that the calculated ΔT_N lies in the correct order of magnitude. Although this explanatory approach on the offset of nozzle thrust and the rough estimation provides good results, further work towards a verification of the made assumptions should be carried out. Thus, no correction of the nozzle thrust will be applied to the results of the upcoming optimization.

Chapter 4

Optimization

4.1 Baseline design

As a starting point for the exploration algorithm, a baseline design needs to be defined. The nozzle section geometry of this design is based on the CST Methodology to allow for maximum variability while keeping the number of design variables within reasonable limits. As the propeller geometry is much more complex than the nozzle and the number of design variables needs to be limited, the CST approach will not be applied to this task. By starting out with a predetermined design and introducing only a few variables by means of re-parametrization of said geometry, a sophisticated propeller can be generated with only a few variables. This procedure is vital as the number of design variables drastically increases the quantity of variants that need to be analyzed during the exploration and optimization phase. Furthermore, the use of a propeller geometry which is already adapted to the requirements of the task at hand makes for a much better starting point than if the baseline design was created without consideration of the demands.

4.1.1 Class Shape Transformation (CST) methodology

When it comes to optimization based on variable geometry, a parametric model is needed to provide a simple way of changing the shape by varying its specifying parameters. According to [15] any geometric representation technique should include the following desirable characteristics:

- Well behaved, producing smooth and realistic shapes
- Mathematically efficient and numerically stable process that is fast, accurate and consistent
- Require relatively few variables to represent a large enough design space to contain optimum shapes for a variety of design conditions and constraints
- Allow specification of design parameters such as leading edge radius, boat-tail angle, airfoil closure.
- Provide easy control for designing and editing the shape of a curve

- Geometry algorithm should have an intuitive and geometric interpretation.

The CST methodology fulfills those requirements. The approach is unique in its ability to model a large variety of geometries utilizing only a small number of equations and parameters. The use of discrete coordinates as design variables would evidently lead to a design space populated with a large number of infeasible, e.g. bumpy or irregular surfaces. Therefore parameterization methods based on Bezier curves, B-Splines or NURBS are often used to model smooth shapes, but oscillations can easily occur when performing curve fits based on those functions [16]. The CST approach is very similar to the above mentioned parameterization methods in that it is based on Bezier curves but enhanced by the use of an additional class function term. This class function ensures that the shapes of all derived variants within the design space match up with a particular category. Compared to a simple parametrization, the number of parameters is reduced as the selected class function inherently ensures that the generated CST curves lie within the group of shapes in question. Many known aerodynamic shapes such as NACA, elliptic and wedge airfoils can be reproduced by use of the CST airfoil classes using only a small number of parameters and any variants within the design space are smooth and physically realistic.

4.1.2 Nozzle design

As mentioned before, the design of the nozzle is based on the CST methodology. The nozzle itself is created as a surface of revolution of a section which is rotated around the axis of rotation of the propeller. The section is divided into an upper and lower curve, whereby the upper curve represents the part of the nozzle facing away from the propeller towards the surrounding fluid and the lower curve generates the surface facing inwards, towards the axis of rotation. As given in [16], the two curves can be written as:

$$\zeta_u(\psi) = C_{N_2}^{N_1}(\psi) S_u(\psi) + \psi \Delta \zeta_u \quad \text{and} \quad (4.1)$$

$$\zeta_l(\psi) = C_{N_2}^{N_1}(\psi) S_l(\psi) + \psi \Delta \zeta_l \quad , \text{ where} \quad (4.2)$$

$$\psi = \frac{x}{c} \quad \text{and} \quad \zeta = \frac{z}{c} \quad . \quad (4.3)$$

For a NACA type airfoil with a round nose and pointed end, the exponents of the general class function

$$C_{N_2}^{N_1}(\psi) = \psi N_1 (1 - \psi)^{N_2} \quad (4.4)$$

are set to $N_1 = 0.5$ and $N_2 = 1.0$. The overall shape functions for the upper and lower surfaces are:

$$S_u(\psi) = \sum_{i=0}^{N_u} A_u(i) S(\psi, i) \quad \text{and} \quad (4.5)$$

$$S_l(\psi) = \sum_{i=0}^{N_l} A_l(i) S(\psi, i) \quad , \quad (4.6)$$

with the component shape funktion given as:

$$S(\psi, i) = K_i^n \psi^i (1 - \psi)^{N-i} \quad \text{and} \quad (4.7)$$

$$K_i^n = \frac{n!}{i! (n - i)!} \quad . \quad (4.8)$$

Thus, the complete equations representing the upper and lower surface generating curve, can be written as:

$$\zeta_u(\psi) = \psi^{0.5} (1 - \psi)^{1.0} \sum_{i=0}^{N_u} \left[A_u(i) \frac{N_u!}{i! (N_u - i)!} \psi^i (1 - \psi)^{N_u - i} \right] + \psi \Delta \zeta_u \quad \text{and} \quad (4.9)$$

$$\zeta_l(\psi) = \psi^{0.5} (1 - \psi)^{1.0} \sum_{i=0}^{N_l} \left[A_l(i) \frac{N_l!}{i! (N_l - i)!} \psi^i (1 - \psi)^{N_l - i} \right] + \psi \Delta \zeta_l \quad , \quad (4.10)$$

using the equations (4.1) to (4.8). To introduce an angle of attack α_{nozzle} into the model, the last summand in (4.9) and (4.10) is simply set to $\psi \cdot \tan(\alpha_{nozzle})$. As the CST method, applied this way, tends to produce sections with a very thin and only slightly tapered trailing edge, one modification is added to the described procedure. A rounded trailing edge is added by cutting off the original sharp trailing edge at the position where the thickness of the section is 0.6 mm. A NURBS curve is than fitted in between the end points of the upper and lower section curve. The control points are chosen to match the angle of both curves to ensure C^1 continuity and the weights are set so that the trailing edge is close to circular in shape. As this procedure changes the nozzle length by a different fraction, depending on the shape, the section is afterwards scaled back to its original length.

In practice, the nozzle needs to accommodate the electric motor driving the propeller and hence, the motor dimensions need to be taken into account when changing any of the parameters defining the nozzle section shape. A lot of effort was made in parallel to this thesis, designing an electric motor with a large through-hole allowing to fit the rim and propeller, while the radial height of the motor was kept as low as possible. The construction is based on the assumption that the nozzle itself will not be beneficial when it comes to propulsive efficiency under working conditions. However, a number of reasons speak for

the targeted design and thus, the nozzle profile shall be kept as thin as possible while allowing for the necessary installation space for the motor, rim and bearings.

To achieve the desired motor specifications, it was decided, to realize the motor as an in-runner, with the stator being only a 33.75° section which can be embedded into the strut connecting the thruster to the hull. To further optimize this design, the nozzle itself will be machined out of fluid dynamic bearing material, such as PTFE. This allows for a very low radial height of the remaining circumference of the nozzle. Only the propeller's rim, connected to the permanent magnetic rotor and the part of the bearing which serves as a friction partner to the nozzle need to fit into the available space.

The upper and lower surface are both defined by $N_u = N_l = 3$ parameters plus the additional angle of attack α and the nozzle length l_{nozzle} . The parameters defining the upper curve and thus the outer surface of the nozzles are named O_i and consequently I_i in case of the lower curve or inner surface. The CST functions can now be written as:

$$\zeta_u(\psi) = l_{nozzle}\psi^{0.5}(1-\psi)^{1.0} [O_1(1-\psi)^3 + 3O_2\psi(1-\psi)^2 + 3O_3\psi^2(1-\psi)] + l_{nozzle}\psi \cdot \tan(\alpha_{nozzle}) \quad \text{and} \quad (4.11)$$

$$\zeta_l(\psi) = l_{nozzle}\psi^{0.5}(1-\psi)^{1.0} [I_1(1-\psi)^3 + 3I_2\psi(1-\psi)^2 + 3I_3\psi^2(1-\psi)] + l_{nozzle}\psi \cdot \tan(\alpha_{nozzle}) \quad , \quad (4.12)$$

where ψ covers the interval $[0, 1]$. After the trailing edge is added and the nozzle is scaled back to its originally defined length, the motor now needs to be placed at the most convenient position which is said to be the one allowing for the thinnest section profile. As the motor dimensions and position are fixed, the nozzle is allowed to move axially at a variable diameter to find said position. A simple algorithm is used which determines a nozzle diameter and axial position which fits the motor and subsequently scales the shape function parameters O_i and I_i down to a minimum which still allows the motor to fit inside with an additional 2 mm clearance to ensure the structural integrity of the nozzle. The diameter and axial position are then checked again for another suitable position and the shape function parameters are reduced further. This loop is executed a number of times, until the algorithm is not able to significantly reduce the parameters any further and thus, the thinnest profile at the given parameter combination is found and the optimum motor position inside the nozzle is set. Obviously, this scaling procedure results in the final shape of the section being the same, if the combination of parameters $O_{i,a}$, $I_{i,a}$ of a nozzle a are any multiple of a nozzle b , such as $O_{i,a} = m \cdot O_{i,b}$, $I_{i,a} = m \cdot I_{i,b}$. One of the six parameters, I_3 , is therefore set to a fixed value of $I_3 = -2$ and will not be varied, as a collective change of the remaining five parameters by a common factor m will effectively change I_3 .

In figure 6.1, given in the section on geometry comparison of the baseline and optimized variant, two sections along with their defining parameters and schematic motor drawings can be seen. A good impression on the overall parametric model is also given in the figures 6.4 and 6.5 of section 6.1.2. Depending

on the shape of the nozzle and the corresponding motor position, a part of the inside surface is separated to be added to the rotating region as rim of the propeller. As the rim itself creates a lot of friction due to its rotative motion, the rim surface is held as narrow as possible within the constraints of the electric motor design.

4.1.3 Propeller design

The dimensions of the vessel and consequently the data such as required power input, speed of advance and rotational speed are very small compared to any vessels that usually operate in similar environments. It is therefore assumed that criteria such as thrust loading coefficient, strength of the propeller blades or cavitation number can be neglected. Unsteady forces acting on the hull due to the discrete number of blades are not of any concern either, as they will be of low amplitude and no aspects of comfort need to be considered on an unmanned vessel. The number of propeller blades is consequently set to $n_{blades} = 2$ as the lower surface area aids in reducing viscous forces. A one-bladed propeller, though probably possible from a cavitation and thrust loading viewpoint, is discarded to prevent excessive bearing wear due to high torque acting orthogonal to the propeller's axis of rotation. To start out with an already reasonably good design and keep the parametric propeller model fairly simple, a baseline design for the propeller is generated, based on a set of rough data. This initial design is not part of this work as it is no personal contribution of the author, but a support given by third party to the aXatlantic project behind this thesis (see page v). To enable geometry variation of the designed blade for further optimization, a re-parameterization needs to be performed. The geometry is given in the form of an IGES file and thus, at first the blade section needs to be extracted at any radii in between the propeller through-hole at $r = 6.26 \text{ mm}$ and the rim at $r = 50 \text{ mm}$. A feature compiled within CAESES extracts those sections by intersecting the blade with a cylinder of varying radius and flattens them out onto a plane. The angle of attack of each section is then determined by generating the chord-lines and measuring the angle towards the axis of $P/D = 0$. The discrete points are fed into a curve fitting procedure and the resulting 3rd degree B-Spline curve with 6 control points is stored as $\alpha_{baseline}(r)$. When regenerating the propeller surface as a parametric version, instead of the original curve $\alpha_{baseline}(r)$, a modified version called $\alpha_{total}(r)$ is handed over to the algorithm. This allows for any modification of P/D over the hole range $[6.26 \text{ mm}, 50 \text{ mm}]$ of R . To modify $\alpha_{baseline}(r)$, two parameters are introduced, namely $\Delta\alpha$ and $\alpha_{distribution}$. The first mentioned simply offsets the baseline curve by adding its value up to the corresponding coordinate of all 6 control points. The second parameter $\alpha_{distribution}$ creates a B-Spline curve

based on three control points p_i which are set to

$$p_1 = (6.25/0/0) \quad , \quad (4.13)$$

$$p_2 = \left(\frac{50 - 6.25}{2} / 0 / 0 \right) \quad \text{and} \quad (4.14)$$

$$p_3 = (50/0/\alpha_{distribution}) \quad . \quad (4.15)$$

The ordinate values of this curve are determined at 6 equidistant positions over the hole range of radii and also added up to the corresponding coordinate of the six control points of the baseline curve. The resulting 6 points are used, to define the new curve $\alpha_{total}(r)$ which remains unchanged if $\Delta\alpha = 0$ and $\alpha_{distribution} = 0$, but allows for very flexible modifications.

In a similar manner, the camber of the blade is changed. For this step, no baseline was extracted and stored. The parameters for an additional camber Δc and for variation $c_{distribution}$ are defined and added up to a curve $c_{total}(r)$. This curve defines one camber value for every radial position. This value of camber is then added to each section by means of a B-Spline curve c_r , defining the variable offset from the original profile. The function c_r is defined at each radial position based on the distance between leading and trailing edge and a mid-point which creates an offset of $c_{total}(r)$. Subsequently, the curves defining the suction and pressure side of each section are offset by the variable distance given by c_r . To achieve this within CAESSES, the suction and pressure curves as well as c_r are discretized and the ordinate values are summed up. The total angle of attack of the sections is set to $\alpha_{total}(r) = 0^\circ$ during this process, to ensure the direction of offset lies perpendicular to the chord-line.

4.2 Design variables

When optimizing the thruster, a number of geometric parameters are introduced as design variables. Certain measures, such as the propeller diameter and thickness of the nozzle section, are set by the dimension of the electric motor. The parameters defining the thruster geometry as described in the previous sections 4.1.2 and 4.1.3 can be used for geometry variation during the optimization process. To limit the computational effort, not all parameters will be used as design variables, although the computational setup would allow for a much more comprehensive study. A presumption of the parameters that are considered to have the highest potential in improving the efficiency of the thruster is made and the remaining parameters, although set as design variables, are held constant during the process.

Table 4.1 gives an overview over the variables and their interval ranging from the lower bound b_l to the upper bound b_u , including the value that defines the baseline design v_b . The parameters held constant during the computations are marked as disabled and those used as design variables as enabled, respectively. In the last column, the impact of each variable is outlined for a quick insight.

variable	en-/disabled	$[b_l/v_b/b_u]$	$[unit]$	description
α_{nozzle}	enabled	$[0/0/10]$	$[deg]$	changes the nozzle section's angle of attack with higher values resulting in an accelerating duct and vice versa
I_1	enabled	$[-3/ - 2/ - 1]$	$[1]$	shape function parameter acting on the inside of the nozzle section in proximity to the leading edge with higher values resulting in a more bulbous shape
I_2	enabled	$[-3/ - 2/ - 1]$	$[1]$	shape function parameter with the same impact as I_1 , but acting in the mid region of the section
O_1	disabled	$[1/2/3]$	$[1]$	same as I_1 , but acting on the outside surface
O_2	disabled	$[1/2/3]$	$[1]$	same as O_1 , but acting in the mid region
O_3	disabled	$[1/2/3]$	$[1]$	same as O_1 , but acting near the trailing edge
l_{nozzle}	disabled	$[40/50/60]$	$[mm]$	nozzle length
$\Delta\alpha$	enabled	$[0/0/10]$	$[deg]$	blade's angle of attack that is added up to the original distribution of the baseline design
$\alpha_{distribution}$	disabled	$[0/0/5]$	$[deg]$	creates a distribution function for the angle over the hole range of radii that is also added up to the original distribution of the baseline design
Δc	enabled	$[0/0/2]$	$[1]$	discrete value that results in a change of the camber mean line for every radius
$c_{distribution}$	disabled	$[0/0/2]$	$[1]$	creates a distribution function for the camber value over the hole range of radii that acts the same way as Δc , but enables a variation in radial direction

TABLE 4.1: Table of design variables showing their status, bounds, units and a brief description on their effect on the geometry.

4.3 Objective

During the process of optimization, a measure is needed to evaluate the quality of every variant. The starting point in similar tasks is usually the design speed of the ship which is set based on various economic considerations and with the operating profile in mind. In the task at hand, the energy on board is supplied by solar cells on the deck and therefore, only limited power is available to propel the vessel. A rough calculation, based on the amount and efficiency of solar cells mounted, as well as the geographic position range and operating season, results in an approximated minimum continuously available power of 15 W for the propulsion. Usually, when choosing a propeller for a given ship, the aim is to meet $\eta_{o,max}$ while advancing at the desired design speed to minimize power consumption. However, in the case at hand, there is no specific target speed given. The aim is rather to get the best possible performance out of the available power by using minimum energy to cover maximum distance. Thus, the objective of the optimization will be, to maximize the speed of the vessel

$$\max \|v_S\| \quad , \quad (4.16)$$

while using the given amount of available power

$$P = 15\text{ W} \quad . \quad (4.17)$$

To calculate the advance coefficient J , the corresponding rotations per minute n and the vessels velocity v_S at the given power of $P = 15\text{ W}$, the following considerations are made:

For every design variant investigated, there is an advance coefficient J_d , at which the vessel uses the exact amount of available power. If J differs from this specific design advance coefficient, the vessel either uses up more or less power, or an external force would have to act on the hull. Thus, it is very unlikely to meet this design point when simulating a variant of unknown propulsive characteristics.

Common practice in similar tasks involves a linear interpolation of K_T and K_Q over a short interval of J . By calculating the power consumption as a function of J , K_T and K_Q , the same basic principle can be applied to the task at hand. Firstly, the delivered thrust of the thruster needs to match the resistance of the hull. This dependency can be written as

$$R_T = T(1 - t) \quad (4.18)$$

with the thrust deduction coefficient t accounting for the propeller-hull interaction. Using the correlation $T = K_t \rho n^2 D^4$, equation (4.18) can be written as

$$R_T = K_T \rho n^2 D^4 (1 - t) \quad . \quad (4.19)$$

The torque coefficient in equation (4.19) is known from the CFD simulation and the resistance of the hull is determined from experiments in the towing tank at TU Berlin. As no further tests were performed in the tank and also no simulations in any other than open water status are performed, the thrust deduction coefficient, as well as the wake fraction coefficient are estimated at

$$t = 0.1 \quad \text{and} \quad w = 0.15 \quad .$$

The thrust deduction coefficient t describes the propeller-hull interaction due to the reduction of pressure upstream of the propeller. In case of the vessel at hand, only very little surface area is exposed to this region of reduced pressure. In fact, the only rigid surface positioned directly upstream of the thruster is the vessel's keel. This surface however mainly faces sideways and hence does not create much of a decelerating force when exposed to the suction of the propeller. Therefore, at $t = 0.1$ the estimated thrust deduction is still rather conservative.

On the other hand, the wake fraction might be estimated slightly high. At a block coefficient of the hull as low as $C_B = 0.22$, the wake fraction coefficient could be expected to be even lower than $w = 0.15$. As both coefficients come together in the hull efficiency as:

$$\eta_H = \frac{1 - t}{1 - w} \quad , \quad (4.20)$$

erroneous assumptions in both estimates should balance each other out to some degree.

To use the discrete experimental values of the hull resistance as a continuous function of speed in equation (4.19), a curve-fit based on a least squares approach is done. According to ITTC '57, the total resistance of a ship is described by a frictional resistance coefficient c_F and a number of other coefficients, such as the residual resistance coefficient c_R and additional resistance coefficients accounting for wind, waves and appendages. Hence, the total resistance can be written as:

$$R_T(v_S) = c_T \frac{1}{2} \rho v_S^2 S \quad (4.21)$$

with the total resistance coefficient

$$c_T = c_F + c_R + c_A \quad . \quad (4.22)$$

The frictional resistance coefficient c_F can be estimated based on the empirical model-ship correlation line formula in ITTC '57 as:

$$c_F = \frac{0.075}{(\log_{10}(Re) - 2)^2} \quad (4.23)$$

and the above given formulas (4.21, 4.22 and 4.23) can be joined and simplified to

$$R_T(v_a) = \left[\frac{0.075}{\left[\log_{10} \left(\frac{v_a l}{(1-w)\nu} \right) - 2 \right]^2} + c_R + c_A \right] \frac{1}{2} \rho \left(\frac{v_a}{1-w} \right)^2 S \quad (4.24)$$

$$= \frac{av_a^2}{(\log_{10}(v_a) + b)^2} + cv_a^2 \quad (4.25)$$

$$\text{with } Re = \frac{v_S l}{\nu} \quad \text{and} \quad v_S(1-w) = v_a \quad .$$

The coefficients a , b and c in equation (4.25) are the parameters that will be determined by the least squares fitting algorithm. They are simply introduced by substituting:

$$a = \frac{0.0375\rho S}{(1-w)^2} \quad , \quad (4.26)$$

$$b = \log_{10} \left(\frac{l}{\nu(1-w)} \right) - 2 \quad \text{and} \quad (4.27)$$

$$c = \frac{(c_R + c_A)\rho S}{2(1-w)^2} \quad . \quad (4.28)$$

Fitting a curve based on the model function (4.25) to the experimental data does not necessarily correspond to the determination of any unknown variables in the equations (4.26), (4.27) and (4.28). The reason for this is, that these parameters are derived from an empirical formula which is based on a flat plate drag model and additional coefficients that are not a function of the ship speed. However, as the total resistance of the vessel at the speed range under consideration can be assumed to be mainly frictional resistance, the model function should still be applicable for a good approximation of the experimental data.

The results of the resistance test carried out in the towing tank at TU Berlin are given in table 4.2 and the graph in figure 4.1 shows the curve fitted to those measures based on equation (4.25). The parameters determined are:

$$a = 42.0456 \quad , \quad (4.29)$$

$$b = 8.3354 \quad \text{and} \quad (4.30)$$

$$c = 1.0653 \quad . \quad (4.31)$$

The graph shows a good approximation with a slight overestimation of R_T for all, but the last measure and the sum of squares equals 0.15 N for the given coefficients. It seems, the lower measures might easily be approximated more accurately by the given model function, but as v_s comes close to 2 m/s , which is approximately the hull speed of the vessel, the model function fails to reproduce the increase in resistance due to increasing wave making resistance. The

speed of the ship v_s in $[m/s]$	total resistance R_T in $[N]$
0	0
1.007	1.594
1.216	2.340
1.429	3.196
1.639	4.277
1.840	5.454
2.051	7.129

TABLE 4.2: Total resistance data and ship speed measured during the towing tank tests.

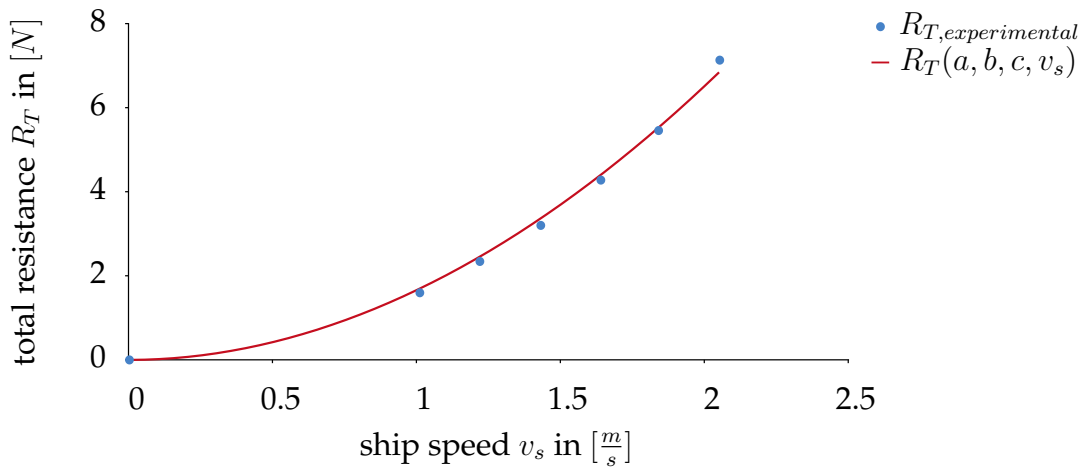


FIGURE 4.1: Discrete experimental findings from the resistance test and the curve fitted, based on the coefficients given in (4.29), (4.30) and (4.31) and the model function (4.25).

approximation is still considered accurate enough to proceed with the calculation of the optimizations objective based upon it.

After computing the coefficients a , b and c , an additional resistance coefficient could be simply introduced into c , to account for an expected sea margin. This would be only a rough guess, as no reliable data could be found in the literature for a vessel this size operating in a similar environment. Additionally, the most favorable route and season will be chosen for the maiden voyage of the aXatlantic. Therefore, it might be even possible for c_A to be negative with strong currents and winds facing in the direction of travel. In total, those effects might cancel out with negative influences such as waves and fouling. Apart from that, one side effect in not introducing an additional coefficient is, that the accuracy of the predicted propulsion point can rather simply be assessed by analyzing the vessels power consumption versus speed in calm conditions.

Once the coefficients are known, from the equations (4.19) and (4.25) follows:

$$K_T \rho n^2 D^4 (1-t) = \frac{a v_a^2}{(\log_{10}(v_a) + b)^2} + c v_a^2 \quad . \quad (4.32)$$

Hence, the rotational speed can be written as:

$$n = 10^{\left(\frac{\sqrt{a} J D}{\sqrt{K_T \rho D^4 (1-t) - c J^2 D^2}} - b - \log_{10}(J D) \right)}, \text{ with } v_a = J n D \quad (4.33)$$

and the power used by the thuster can be written as a function of J as follows:

$$P(J) = 2\pi K_Q \rho D^5 \cdot 10^{3 \left(\frac{\sqrt{a} J D}{\sqrt{K_T \rho D^4 (1-t) - c J^2 D^2}} - b - \log_{10}(J D) \right)}, \quad (4.34)$$

with the power of the rotating propeller:

$$P = 2\pi K_Q \rho D^5 n^3 \quad . \quad (4.35)$$

As stated earlier, the coefficients K_T and K_Q are not known over the hole range of advance coefficients. However, within an interval $[J_1, J_2]$ they can be approximated as a linear function with sufficient accuracy as:

$$K_T(J) = \frac{K_{T2} - K_{T1}}{J_2 - J_1} J + \left(K_{T2} - \frac{K_{T2} - K_{T1}}{J_2 - J_1} J_2 \right) \quad \text{and} \quad (4.36)$$

$$K_Q(J) = \frac{K_{Q2} - K_{Q1}}{J_2 - J_1} J + \left(K_{Q2} - \frac{K_{Q2} - K_{Q1}}{J_2 - J_1} J_2 \right) \quad . \quad (4.37)$$

The chosen interval $[J_1, J_2]$ should preferably include the design advance coefficient, or at least ensure, J_d lies within close proximity to the bounds. Therefore, during the exploration phase, when the solutions accuracy is not jet as vital as during the final optimization, an estimation on J_1 and J_2 is sufficient enough. After the exploration phase is completed, the values can be adjusted to meet the design advance coefficient as closely as possible.

With the results for both simulations at hand, the equations (4.36) and (4.37) allow for the calculation of the power consumption $P(J)$ according to equation (4.34). Hence, the design point J_d can be calculated. Based on J_d , now the corresponding values of $K_T(J_d)$ and $K_Q(J_d)$ can be calculated, again using the equations (4.36) and (4.37). With $K_T = K_T(J_d)$, now also the rotational speed of the propeller $n(J_d)$ is known and finally, the speed of advance $v_a(J_d)$ and thus, the vessels velocity $v_S(J_d)$ can be calculated based on the definition of the coefficient of advance and the approximation of the wake fraction coefficient.

As $v_S(J_d) = v_S(P = 15 W)$, the objective (4.16) and the constraint (4.17) of the optimization can be summarized into one single objective:

$$\max \|v_S = v_S(J_d, n(J_d, P = 15 W))\| \quad . \quad (4.38)$$

4.4 Grid generation

For an automatic CFD computation of every variant of the changing geometry, an automatic grid generation tool is needed. The basis for each mesh is an IGES export with the geometry data of the design. The process of grid generation is split up into the nozzle and propeller region of the mesh.

The nozzle region is handled first, by exporting a section of the nozzle, along with the most important components defining the mesh topology. It has shown during this work, that the generation of a structured grid for varying geometry, using the same basic topology, can be challenging in terms of the resulting mesh quality. One mayor step in improving the grid quality, especially towards criteria like skewness and aspect ratio was, to add the most important parts of the grid topology already within CAESES as a part of the parametric thruster model. This way, they easily adjust to the changing geometry without the need to analyze the shape within the grid generation script and adjust the topology at this stage. Figure 4.2 shows the exported geometry of two different nozzles as well as the resulting surface meshes in close proximity to the propeller region.

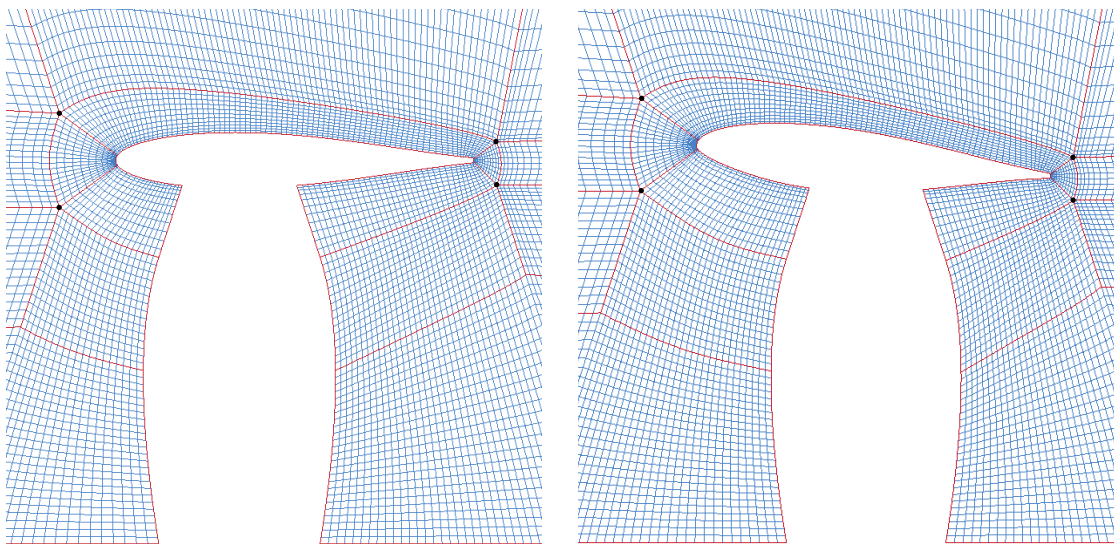


FIGURE 4.2: Surface meshes on the symmetry plane of the computational domain (excluding propeller region) for initial and optimized design. The most important grid lines and points are not generated within the Pointwise script, but already exported from CAESES together with the thruster geometry.

It can be seen, that the export of the basic topology helps in positioning important grid points in their favorable position. As already mentioned in chapter

2.2.4, the position of those points where five grid-lines meet in one point is important, as these areas are prone to create low included angles within the cells. The 4 points this applies to are highlighted with black markers in figure 4.2. By positioning them so that the grid lines running towards the nozzle surface meet the nozzle section at an angle of 90° , a high quality boundary layer is assured. All other grid lines running away from these points are defined in such a way, that the included angles within of all five grid lines is close to $360/5^\circ = 72^\circ$ which is the theoretical optimum achievable in those points.

The thickness of the boundary layer region is set, as can be seen from the red grid lines surrounding the nozzle in figure 4.2. This allows for easy manipulation of the wall spacing and number of layers within the script. The dimensions of the domain are set as they were derived during the domain-size study for the reference simulations in section 3.1. Because of the propeller blades having their widest span in axial direction somewhere in between the rim and the axis of rotation, the boundaries towards the propeller region are somewhat bulky. This creates enough room inside the propeller region to allow a sufficient number of boundary layers around the blade without interfering with the nozzle region. To cut the computational costs, as also done during the reference simulations, only a rotational symmetric section will be simulated. In this case, as the propeller is two-bladed, the grid needs to cover a 180° region. This is simply achieved by creating a rotational extrusion of the generated surface mesh around the propeller's axis of rotation. The area near the axis of rotation is handled separately as in the reference case (see. subsection 2.2.4), to keep the cell from degenerating to triangular prisms at the centerline.

The meshing of the propeller region proved to be a lot more difficult to handle by a script due to the complex shape of the blade. Regions like the fillet connecting blade and rim, the sharp trailing edge and the winglet are already demanding. Additionally, the blades shape changes over a wide range of parameters which is hard to handle by one single meshing strategy. As a result, the quality of the propeller mesh is not quite as good as in the nozzle region. When the minimum included angle and aspect ratio of the cells are monitored, the propeller region shows a number of cells with slightly lower quality than in the nozzle region. Attention is paid to the areas in which those cells are located as they do not impact the solution or convergence as much when occurring in regions with low gradients. The near-wall cells, as well as cells downstream of sharp edges and those located in close proximity to the AMI interfaces are of much greater importance and thus, the grid generation is focused on creating a higher grid quality in those areas.

Although different meshing scripts could be applied to certain groups of geometry variants which would possibly help to raise the propeller mesh quality up to the level of the nozzle region, another reason speaks for a single approach to handle the whole range of geometry variants. This way, the meshes of two different variants are nearly consistent in topology and the change in between rather equals a mesh morphing than two completely different grids. Especially when comparing geometries that are very similar, the simulation error induced by the quality of the grid could exceed the actual difference in performance of

the two variants. However, if the two grids are almost identical, as would also be the case in a traditional mesh morphing approach, the two variants might still be rated from a relative point of view.

The propeller-region mesh is, based on the experience gained during the grid generation of the reference design, split into three separate regions. In general, the resulting grid looks similar to the one shown in figure 2.6 except from being a $1/2$ section, rather than a $1/4$ section as with the reference design. The cell-faces on the surfaces connecting those regions are again handled by the AMI interpolation functionality within OpenFOAM. In the digital appendix that comes with this thesis, the grids for the baseline and optimized thruster design are given. Additionally, the Pointwise script is included, enabling the user to generate grids for any geometry version within the possibilities of the parametric CAD model.

4.5 Simulation setup

As opposed to the reference simulation, the surface mesh used to create the volume mesh of the nozzle region by means of rotational extrusion, is now entirely planar. This allows for the use of a `cyclic` boundary condition instead of `cyclicAMI` and thus eliminates interpolation errors and consequently reduces CPU time needed to perform those interpolations at each time step.

Furthermore, the propeller variants generated by the parametric model are two-bladed only, as opposed to the four-bladed Ka4-70 propeller examined as a reference case. Hence, a 180° section of the computational domain will be calculated instead of the 90° section during the reference simulation.

Another difference distinguishing the two setups is the definition of the rotating and stationary region. During reference simulations the propeller region has been defined as rotating, while the remaining volume has been set as static domain. During test runs of the 180° version, convergence problems have been observed arising from the `cyclicPeriodicAMI` boundaries. While similar problems also occurred in an early stage of the 90° setup, careful matching of the sliding faces solved the problems at this stage. As an analogue procedure did not help in case of the 180° domain, the problem has been solved by changing the definition of the static region towards rotating as well. The physics of the simulation are not affected by this kind of definition, as the nozzle itself is a rotational symmetric body and its U -boundary condition is still set to zero. As a result, the sliding grid interfaces in between the rotating and previously static region are no longer in relative motion towards each other. Their boundary conditions are changed from `cyclicPeriodicAMI` towards `cyclicAMI` accordingly. Technically, even the generation of two separate grids becomes unnecessary due to this procedure. However, as the complex geometry of the RDT asks for separate grid regions anyway, the already existing automatic grid generation script remains unaltered by this adjustment.

Besides the change in domain size from a $1/4$ towards a $1/2$ section, the new definition of the rotating domain and the necessary adjustments in boundary conditions, the CFD setup developed during the reference simulations remains

unchanged. This is important, as the reason of conducting the reference simulations was not only to choose a valid procedure for the correction of frictional losses, but also the definition of an accurate simulation setup. By applying only minimal changes when adapting this reference-setup to the optimization task, a validation of the results by means of experiments can be forgone.

Along with this thesis, a digital copy containing several OpenFOAM files is compiled which allows detailed insight into the many aspects of the CFD setup not addressed within this written work. Appendix C gives an overview of the included files and allows a quick insight to the interested reader for rerunning, testing, altering or monitoring any specific setup or data.

4.6 Exploration phase

As with most optimization problems, there is no information on the target function within the design space. Therefore, the research area of the optimization is often referred to as a "black box". Inside this black box, the target function may have multiple local minima and maxima. To gain an insight into the approximate behavior of the target function an exploration algorithm based on a Sobol sequence will be used. This preliminary exploration is helpful in speeding up the process of finding an optimized geometry. It helps in choosing a suitable starting point for an upcoming optimization and additionally serves as a basis for the surrogate model. This allows for a much better convergence during this second phase.

Sobol sequences, often referred to as 'quasi-random', are used to fill a design space with points that are evenly distributed but of low discrepancy. Filling the design space with a grid-like, structured set of points can lead to poor convergence. Selecting samples that align with the coordinate axes can cause unexpected behavior, as a row of points may align with a corridor in the target function accidentally. Low discrepancy sequences avoid this kind of structured distribution, as the discrepancy itself is a measure of the uniformity of a distribution. At the same time, the Sobol algorithm aims to cover the design space evenly, avoiding any clustering of point sets or large regions with no points at all. This holds true also for multi dimensional design spaces and can be monitored by comparing all possible pairs of dimensions in a 2D space. A further advantage of the Sobol algorithm, related to its quasi-randomness, is the fact that it can be reproduced as opposed to a random distribution.

This is particularly convenient when adjustments are made to the evaluation of the target function or any other evaluations within CAESSES. Provided the starting point is the same as in a previous investigation, the algorithm always generates the exact same sample and thus allows for a dry rerun of the computations after any changes are applied. Subsequently, the results folders can be swapped and a quick re-evaluation updates all evaluations based on their new definitions. Another advantage is, that the generation of variants can be stopped at any time or further designs can be appended without compromising the low discrepancy and even distribution of the sample. Finally, as the parameter combination for all individual designs are chosen regardless of the

results of any previous simulation, CPU time can be reduced. Instead of massive parallelization of each individual variant, multiple designs can be handled at the same time which minimizes processor-to-processor boundaries and thus, helped to reduce overall computation time.

Table 4.1 shows the whole range of design variables available within the parametric model and also lists those that are enabled during the exploration phase. To estimate the number of design evaluations necessary to capture the interactions between a given number of design variables, a look into the strategies applied within Response Surface Models based on Design of Experiments (DoE) is taken. Although originally developed as a strategy for physical experiments, the DoE approach can be applied to numerical simulations just as well. An approach often chosen is the fractional factorial design. It is based on the full factorial design which aims at covering all the interactions between a number of variables.

To cover the most basic, linear dependencies between k variables, a full factorial design already needs 2^k function evaluations and even 3^k , if second order non linear behavior of the target function shall be covered [19]. An approach often chosen, particularly in early design phases and during screening experiments is the fractional factorial design. It allows to drastically reduce the number of function evaluations at the drawback of aliases occurring within the variables. Thus, it is not possible to differentiate whether a response is caused by a certain variable or its alias, namely a different variable or an interaction of multiple other variables. However, as the number of active variables within this exploration is $k = 5$, as shown in table 4.1, the total number of evaluations for a full factorial 3^k design would be 243. At 2 simulations for each design, because of the two advance coefficients that need to be simulated for each variant, this number by far exceeds the computational resources available. Thus, the number of necessary evaluations for the Sobol algorithm is set to 25. This is close to a fractional factorial 3^{k-2} design which at 27 evaluations corresponds to a $1/9$ fraction of full factorial 3^5 design. Although the design points are not chosen systematically as usual within the DoE process, this number should be sufficient to cover the main influences and interactions between variables, to build a primary response surface upon the results.

Table 4.3 lists the parameter combinations set by the Sobol algorithm and also the initially estimated design speed $v_{d,0}$ of the vessel for each variant, along with further results obtained from the CFD simulation.

4.7 Optimization phase

As already mentioned in the previous section 4.6, the optimization is based on a surrogate model. To enable the use of this kind of algorithm, the external optimization toolbox Dakota is embedded into CAESES. With it comes the possibility of using Response Surface Methodology (RSM) [20] for the optimization task.

The design space available to the optimization algorithm has been described as a black box in the previous section. Hence, a surrogate model can be used to

#	α_{nozzle}	I_1	I_2	$\Delta\alpha$	Δc	$J_{d,0}$	$K_{Q,J_{d,0}}$	$K_{T,J_{d,0}}$	$n_{d,0}$	$v_{d,0}$	$\eta_{o,J_{d,0}}$
0	5.00	-2.00	-2.00	5.00	1.00	0.74	0.06	0.14	16.23	1.42	0.30
1	7.50	-2.50	-1.50	2.50	1.50	0.83	0.07	0.17	15.25	1.48	0.34
2	2.50	-1.50	-2.50	7.50	0.50	0.65	0.05	0.11	17.21	1.31	0.23
3	3.75	-2.25	-1.75	1.25	1.75	0.87	0.07	0.19	14.90	1.52	0.36
4	8.75	-1.25	-2.75	6.25	0.75	0.69	0.05	0.12	16.61	1.35	0.26
5	6.25	-2.75	-2.25	3.75	0.25	0.74	0.06	0.14	16.23	1.41	0.29
6	1.25	-1.75	-1.25	8.75	1.25	0.65	0.05	0.11	17.10	1.32	0.24
7	1.88	-2.38	-2.38	6.88	1.13	0.69	0.05	0.12	16.77	1.36	0.26
8	6.88	-1.38	-1.38	1.88	0.13	0.77	0.06	0.15	15.79	1.43	0.30
9	9.38	-2.88	-1.88	9.38	0.63	0.63	0.05	0.10	17.32	1.29	0.23
10	4.38	-1.88	-2.88	4.38	1.63	0.78	0.06	0.15	15.86	1.45	0.32
11	3.13	-2.63	-1.13	5.63	0.88	0.72	0.05	0.13	16.53	1.40	0.28
12	8.13	-1.63	-2.13	0.63	1.88	0.89	0.08	0.20	14.65	1.53	0.37
13	5.63	-2.13	-2.63	8.13	1.38	0.68	0.05	0.12	16.85	1.35	0.26
14	0.63	-1.13	-1.63	3.13	0.38	0.74	0.06	0.14	16.31	1.42	0.30
15	0.94	-2.06	-1.31	4.06	0.56	0.73	0.05	0.13	16.43	1.41	0.29
16	5.94	-1.06	-2.31	9.06	1.56	0.67	0.05	0.11	16.94	1.33	0.25
17	8.44	-2.56	-2.81	1.56	1.06	0.83	0.07	0.17	15.32	1.49	0.34
18	3.44	-1.56	-1.81	6.56	0.06	0.65	0.05	0.11	17.18	1.32	0.24
19	4.69	-2.81	-2.06	2.81	1.31	0.81	0.06	0.17	15.59	1.48	0.34
20	9.69	-1.81	-1.06	7.81	0.31	0.63	0.05	0.10	17.10	1.27	0.22
21	7.19	-2.31	-1.56	0.31	0.81	0.84	0.07	0.18	15.13	1.50	0.35
22	2.19	-1.31	-2.56	5.31	1.81	0.75	0.06	0.14	16.07	1.43	0.30
23	1.56	-2.69	-1.94	8.44	1.69	0.67	0.05	0.11	16.88	1.33	0.25
24	6.56	-1.69	-2.94	3.44	0.69	0.76	0.06	0.15	16.04	1.44	0.31

TABLE 4.3: Parameter combinations set by the Sobol algorithm and propulsive characteristics for all 25 variants examined during the exploration phase. Note the index '0' used with the obtained measures which indicates that the results are rather qualitative than quantitative (see section 4.8).

describe the measure of interest within this black box. The term Response Surface comes from the special case of 3 design variables. In this case, the measure of interest will be described as an approximated function of those 3 variables, similar to a 3 dimensional surface which can be described as a function $f(x, y, z)$ of 3 coordinates. The same principle can also be applied to any higher order design space, such as in the case at hand. The response surface can no longer be visualized, as in the 3D case. However, technically it could be described as a 5 dimensional surface approximating the target function within the design space that is spanned by the 5 design variables. This approximation function then allows to estimate the target measure for any point in the design space. Models like this become especially advantageous, whenever any outcome of interest can not easily be determined.

In the case at hand, the initial surrogate model is build based on the results of the 25 variants examined during the exploration phase. When used as an optimization tool, the accuracy of the surrogate within the overall design space

is of minor importance. Instead, only areas of high potential with respect to the measure of interest need to be resolved with higher precision. Based on the first approximation, the optimum point within the design space as estimated by the surrogate model is determined. As this approximation is based only on those few variants examined during the previous exploration phase, it will certainly lack accuracy. Therefore, the determined design point is actually simulated as a next step. The result of the target function is then used to refit the response surface based on all simulations evaluated until this point. This approach increases the accuracy of the surrogate model within the region of interest and allows a better estimate on the optimum variant with the number of iterations increasing.

#	α_{nozzle}	I_1	I_2	$\Delta\alpha$	Δc
11	4.7223	-1.3250	-2.7750	-4.6250	1.7000
8	4.7223	-1.3250	-2.8250	-4.6250	1.7000
1	8.1250	-1.6250	-2.1250	0.6250	1.8750
14	4.8284	-1.3375	-2.8125	-4.5313	1.7125
12	4.8123	-1.3375	-2.8125	-4.5313	1.7125
2	7.6250	-1.5250	-2.2250	-0.1250	1.8739
3	7.1250	-1.6250	-2.3250	-0.8750	1.9739
4	6.6250	-1.7250	-2.4250	-1.6250	2.0000
17	4.8333	-1.3406	-2.8094	-4.5078	1.7156
15	4.8310	-1.3406	-2.8094	-4.5078	1.7156
5	6.2223	-1.6250	-2.5250	-2.3750	2.0000
6	5.7223	-1.5250	-2.6250	-3.1250	1.9000
7	5.2223	-1.4250	-2.7250	-3.8750	1.8000
9	4.9723	-1.3750	-2.7750	-4.2500	1.7500
10	4.8473	-1.3500	-2.8000	-4.4375	1.7250
13	4.8177	-1.3438	-2.8063	-4.4844	1.7188
16	4.8255	-1.3422	-2.8078	-4.4961	1.7172

TABLE 4.4: Parameter combinations subsequently set by the RSM-based optimization algorithm. Note, that invalid designs are grayed out and variants are sorted with increasing performance.

In the case at hand, the initial point chosen by the surrogate model is listed as design #2 in table 4.4. Design #1 is linked to the optimum variant #12 obtained during the exploration phase (see table 4.3 for reference). An increase in performance can be monitored at this first iteration already, which proves the surrogate model to be a valid approximation of the target function. Looking at table 4.5 one can see that in fact the surrogate model was able to predict an optimum at every iteration which outperformed all previous designs. After as few as 16 iterations, the design variables, as well as the objective measures converged up to a satisfactory level. Overall, an improvement of approximately 6 % in design speed has been achieved during this phase.

#	$J_{d,0}$	$K_{Q,J_{d,0}}$	$K_{T,J_{d,0}}$	$n_{d,0}$	$\eta_{o,J_{d,0}}$	$v_{d,0}$
11	1.0000	0.0912	0.2544	11.5859	0.4440	1.3630
8	1.0000	0.0912	0.2544	11.6131	0.4441	1.3662
1	0.8870	0.0761	0.1994	14.6487	0.3699	1.5287
14	1.0000	0.0909	0.2532	13.1598	0.4434	1.5482
12	1.0000	0.0909	0.2532	13.1833	0.4435	1.5510
2	0.9074	0.0764	0.2085	14.6304	0.3942	1.5618
3	0.9317	0.0797	0.2197	14.4264	0.4089	1.5813
4	0.9499	0.0824	0.2283	14.2657	0.4190	1.5943
17	1.0000	0.0908	0.2529	13.6400	0.4433	1.6047
15	1.0000	0.0908	0.2529	13.6439	0.4433	1.6052
5	0.9682	0.0852	0.2371	14.1047	0.4287	1.6067
6	0.9799	0.0871	0.2428	14.0007	0.4345	1.6140
7	0.9932	0.0894	0.2494	13.8843	0.4412	1.6224
9	0.9962	0.0901	0.2509	13.8461	0.4415	1.6227
10	0.9992	0.0906	0.2524	13.8193	0.4430	1.6245
13	0.9997	0.0907	0.2527	13.8142	0.4432	1.6248
16	1.0000	0.0908	0.2528	13.8116	0.4432	1.6249

TABLE 4.5: Propulsive characteristics of variants examined during the optimization phase. Designs are sorted according to optimization objective $v_{d,0}$ at increasing performance and invalid designs are grayed out. Note that, as in table 4.3, the index '0' is used with the obtained measures which indicates that the results are only qualitative (see section 4.8).

The designs that are grayed out within the results table, are considered invalid as they do not match the requirement of a power consumption of $P = 15 W$. Further consideration on this issue is spent in section 6.2.

4.8 Evaluation

The previous sections 4.6 and 4.7 lead to a number of variants that can be compared based on the simulation results obtained. The main problem within finding the optimum design is the fact, that the propulsion point of each variant can not easily be determined. Therefore, an optimization strategy was developed, as described in the section 4.3. The given procedure involves the linear approximation of the torque coefficient $K_Q(J)$ based on two subsequent simulations at different advance coefficients J_1 and J_2 . These measures are not directly obtained from the CFD computations. As outlined in section 3.5, adjustments to account for the neglect of friction within rim and nozzle need to be applied to obtain reliable data. While it might be sufficient to assume a linear behavior of $K_T(J)$ and $K_Q(J)$, especially within a small interval $[J_1, J_2]$, this does not hold true for the function $P(J)$ as it is given in (4.34). Not only does it contain highly non-linear terms in J , but more importantly it misses any dependency on the rotational speed of the propeller.

As the simulations were all performed at $n_0 = 7 \text{ s}^{-1}$, the correction of frictional losses during the optimization is based on this rotational speed as well. However, the results given in table 4.5 show a significantly higher value of $n_{d,0} = 13.81 \text{ s}^{-1}$ for the optimum design #16 in the bottom row.

As the following discussion will show, this does not affect the rating of the designs among each other. However, it impacts on the propulsion point and also the quantitative performance of the variants. Hence, the results given in table 4.5 are to be seen from a qualitative standpoint only. This is also stated by the use of the index '0' with the above given measures. As they are based on an initial estimate of the propeller's rotational speed only, they do not resemble quantitative performance of the designs. To show the effect of an adjustment of the rotational speed, a re-evaluation of all design variants is carried out.

The determination of the propulsion point and its characteristic measures $J_{d,1}$, $K_{Q,J_{d,1}}$, $K_{T,J_{d,1}}$, $n_{d,1}$ and $v_{d,1}$ is repeated, based on the obtained rotational speed of $n_{d,0} = n_1 = 13.81 \text{ s}^{-1}$. To do so, the additional torque due to friction within rim and nozzle is re-calculated using the empirical equations (3.6) and (3.7). These approximations contain higher order terms in the angular velocity ω , which is at $\omega = 2\pi n$ well known to be a function of n . The new approximation of the dissipation results in a new function $K_{Q,1}(J)$. As $K_{Q,1}(J)$ is fed into $P(J)$ (4.34), which is used to determine $J_{d,1}$, now a new propulsion point is found. To show the effect of this procedure, figure 4.3 shows the obtained values $v_{d,0}$ and $v_{d,1}$ for all variants based on the two distinct rotational velocities used for their respective correction of frictional losses in $K_Q(J)$. The figure shows all design variants sorted according to their performance when evaluated based on the rotational speed of $n_0 = 7 \text{ s}^{-1}$. One can see that the evaluation based on $n_1 = 13.81 \text{ s}^{-1}$ primarily results in a scaling of the objective measure $v_{d,i}$.

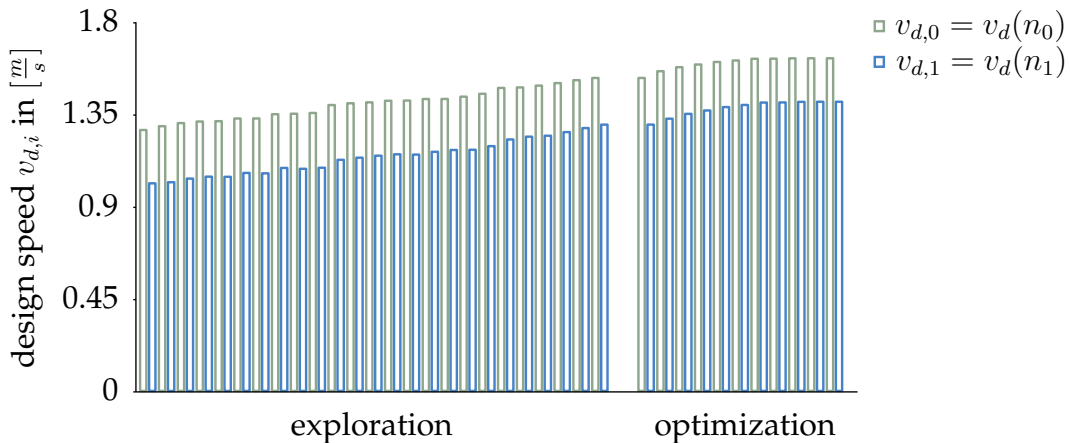


FIGURE 4.3: Difference in estimation of design speed due to approximation of frictional losses based on distinct rotational speeds. Results are sorted according to their performance based on $n = 7 \text{ s}^{-1}$. No qualitative difference in the rating of performance can be seen when comparing both evaluations.

When comparing different designs based on any of the two evaluations, the relative performance between designs does not seem to be affected. This substantiates the prior assumption that the performance of each variant, while it heavily depends on the frictional losses, can be rated qualitatively without considering said dissipation.

As the re-evaluation of the designs did cause a change in the estimated $J_{d,i}$ and $v_{d,i}$, naturally also $n_{d,i}$ changes according to the new propulsion point. In figure 4.4, three different curves of $P(J)$ are given, based on different rotational speeds used for the calculation of their respective frictional losses. As equation (4.34) contains high order terms of J , the ordinate is scaled logarithmic to allow a better comprehension of the plot.

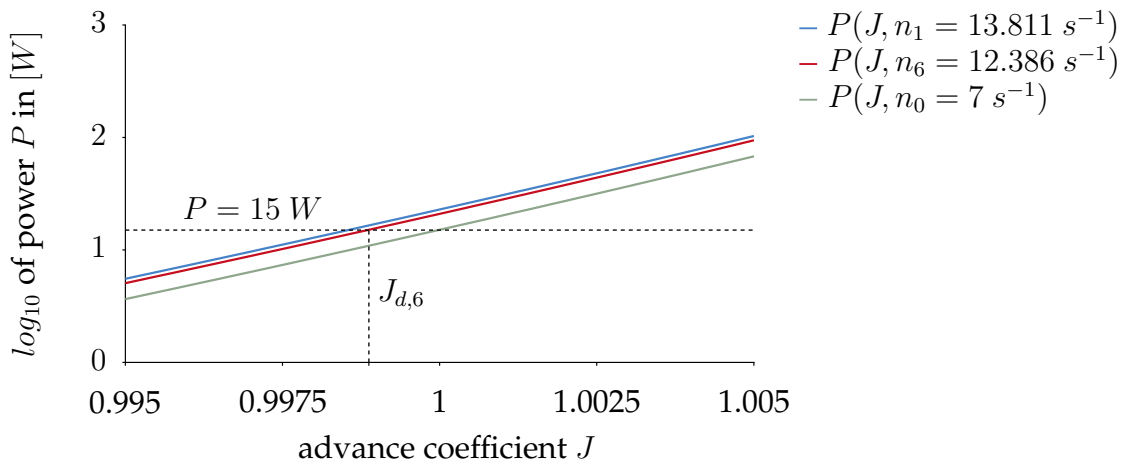


FIGURE 4.4: Evaluation of equation (4.34) over the interval $[J_1 = 0.95, J_2 = 1]$ based on three different rotational speeds n_i . The functions are based on the results of the best design obtained during the optimization, labeled #16 (see table 4.5 for reference).

The graphs show the function $P(J)$ of design number 16 (see table 4.5) which is the best variant found during the optimization phase. As mentioned before, this function depends on the correction of frictional losses and hence, changes with varying rotational speed. After calculating the self propulsion point for the first time, the following pair of variates was obtained:

$$n_0 = 7 \text{ s}^{-1} \qquad n_{d,0} = 13.8116 \text{ s}^{-1} \quad . \quad (4.39)$$

The first re-evaluation then led to:

$$n_1 = 13.8116 \text{ s}^{-1} \qquad n_{d,1} = 12.0145 \text{ s}^{-1} \quad . \quad (4.40)$$

Examining those values, one can already assume a convergence towards $n_i = n_{d,i}$. A total of 6 re-evaluations prove this to be the case, as the values are equal up to less than $1e - 3 \text{ s}^{-1}$:

$$n_6 = 12.3860 \text{ s}^{-1} \qquad n_{d,6} = 12.3855 \text{ s}^{-1} \quad . \quad (4.41)$$

This level of convergence is considered high enough to rate $n_{d,6}$ as the actual rotational speed of the optimized design:

$$n_d = n_{d,6} = 12.39 \text{ s}^{-1} \quad . \quad (4.42)$$

Chapter 5

Verification of optimized thruster design

The exploration and subsequent optimization are carried out based on a number of preliminary assumptions, as well as a procedure of estimating the propulsion point that need further verification. By thorough examination, not only the accuracy of the obtained solution is confirmed, but also the proper operation of the optimization algorithm can be verified. This allows to rate the propulsive efficiency of the optimum design not only towards the comparative geometries, but also in terms of the solutions accuracy.

Out of the 17 variants generated during the optimization phase, the design labeled number 16 is found to be the most suitable. As the optimization algorithm targeted only one single objective, namely v_d , this selection is easily done. In table 4.4, the values of the design variables leading to this geometry can be found and in subsection 6.1.1 figures of the resulting thruster geometry compared towards the initial design are shown.

5.1 Estimated self propulsion point

As already mentioned in the previous section 4.8, the design number 16, out of those generated during the optimization, is considered the optimum obtained within the process. Based on the iterative calculation of n_d , the propulsion point along with its characteristic measures can now be calculated. The table 5.1 lists the results and also compares them to the outcome of a separate flow simulation at this exact propulsion point. This procedure is necessary to confirm the correctness of the estimated propulsion point. It shows, that even with $J_d \approx 1$ outside the interpolation interval of $[J_1 = 0.85, J_2 = 0.95]$, the estimated propulsive characteristics are very accurate (see table 5.1). The validation is carried out at the same rotational speed of $n = 7 \text{ s}^{-1}$, as the simulations at J_1 and J_2 . This keeps the change in Reynolds number to a low level and thus allows for a better validation.

J_1	$v_{a,1}$	n_1	$K_{T,1}$	$K_{Q,1}$		
0.85	0.595	7	0.3100	0.1301		
J_2	$v_{a,2}$	n_2	$K_{T,2}$	$K_{Q,2}$		
0.95	0.665	7	0.2719	0.1273		
$J_{d,estimate}$	$v_{a,estimate}$	$n_{estimate}$	$K_{T,estimate}$	$K_{Q,estimate}$	$\eta_{o,estimate}$	$P_{estimate}$
0.9989	1.237	12.3855	0.2532	0.1259	0.3197	15
$J_{d,validate}$	$v_{a,validate}$	$n_{validate}$	$K_{T,validate}$	$K_{Q,validate}$	$\eta_{o,validate}$	$P_{validate}$
0.9989	0.699	7	0.2531	0.1257	0.3201	14.9744

TABLE 5.1: The table shows the findings obtained from the simulation of the two advance ratios J_1 and J_2 during the optimization process. Furthermore, the estimated characteristic values of the propulsion point at $P = 15 W$ are listed as they are calculated from the simulations at J_1 and J_2 . The bottom section shows the results of another CFD computation at $J_{d,validate} = J_{d,estimate}$. A very good match in the propulsive characteristics such as K_T and K_Q can be seen. This shows also in the very accurate prediction of power consumption at self propulsion point which is well within 0.2 %.

5.2 Reynolds number of optimized variant

The flow simulations during the optimization process are all performed at a constant rotational speed of $n = 7 s^{-1}$. At $J_1 = 0.85$ and $J_2 = 0.95$, the corresponding Reynolds numbers can be written according to the equations (2.3) and (2.2) as:

$$Re_{0.7} = \frac{\sqrt{v_a^2 + (0.7\pi nD)^2} \cdot l_{0.7}}{\nu} . \quad (5.1)$$

With $l_{0.7} = 0.029 m$, $D = 0.1 m$, $v_a = JnD$ and $\nu = 1.004e - 6$, this leads to:

$$Re_{0.7,1} = 47670 \quad \text{at } J = J_1, \quad (5.2)$$

$$Re_{0.7,2} = 48436 \quad \text{at } J = J_2 \text{ and} \quad (5.3)$$

$$Re_{0.7,d} = 86409 \quad \text{at } J = J_d. \quad (5.4)$$

The study of the solutions dependency on the Reynolds number in 3.2 has shown only a small influence of the chosen combination of v_a and n when setting a given J . Based on the findings given in the corresponding figure 3.2, a change in $Re_{0.7}$ of less than a factor 2 should not impact the calculated normalized thrust more than 0.5 %. Therefore, any difference in performance that might be observed when re-running the CFD calculations also at $n_d = 12.3855 s^{-1}$ is assumed to be insignificant.

5.3 Mesh resolution of optimized variant

A comprehensive study on the size of the computational domain and the mesh resolution necessary has been conducted for the reference design in the sections 3.1 and 3.3. The obtained dimensions for the computational domain are applied during the optimization phase as well and are considered to not need any further verification. At

$$l_i = 4 r \quad , \quad (5.5)$$

$$l_o = 10 r \quad \text{and} \quad (5.6)$$

$$R_D = 7 r \quad , \quad (5.7)$$

these measures can be easily applied to the two-bladed thruster examined in the optimization process.

The mesh used for the flow simulations during this phase differs from the one used during reference simulations. The resolution found sufficient for the $1/4$ section of the Ka4-70 propeller investigated is given in table 3.1 at a total of approximately $1.5e6$ cells. As the 2 bladed thruster requires the simulation of a $1/2$ section of the geometry, the cell count during the optimization is chosen higher. A total number of approximately $2.5e6$ cells is assumed to be sufficient during this phase. This is because the cell count is greatly influenced by the resolution of boundary layers adjacent to the propeller components such as blades and hub. Although the computational domain is twice the size, the parametric thruster design examined during the optimization still features only one propeller blade and no hub. Hence, an increase in cell count of a factor 2 was considered unnecessary and the speedup gained by using $2.5e6$ instead of $3e6$ cells more relevant.

This assumption, but also the fact that the general mesh topology differs from the reference simulations involves a verification of the adequate choice of mesh resolution. Similar to the approach in section 3.1, the number of cells will be varied starting from a coarse mesh, compared to the already given mesh and a fine version, each refined by a factor of approximately 1.5. The boundary layers remain unchanged to not bias the outcome due to a manipulation of the wall function and the study is applied to the optimized thruster variant only. As the grids between variants are based on the same meshing script, they vary only slightly in terms of quality and topology and the outcome of this validation is considered representative for all variants. The table 5.2 lists the number of cells for the three grids examined. In figure 5.1 the calculated thrust, normalized to the result obtained from the initial mesh, is compared for the three variants.

The results given in figure 5.1 show a very clear dependency of the calculated thrust, as well as torque, on the chosen mesh resolution. A coarsening of the mesh by a factor of 0.66 leads to an increased prediction of both measures of up to 3 – 4 %. However, a refinement of the initial mesh does not impact the results significantly. A change in the resulting thrust and torque of approximately 0.5 % can be observed which is considered insignificantly small. To confirm the stagnation of forces and moments at further increasing mesh density one might

mesh	scaling factor f	propeller region	domain region
coarse mesh	0.66	464115	1243100
initial mesh	1	694656	1798250
fine mesh	1.5	1043421	2797400

TABLE 5.2: Table of grid resolution, showing the number of cells for each mesh region, depending on the scaling factor. The last column lists the normalized thrust as a measure of the solutions dependency on grid resolution.

consider adding a further level of refinement to this examination. However, the initial mesh density has already been chosen based on a more extensive study of this type (see section 3.3 for reference). As the results now observed reflect a very similar behavior as those obtained for the reference case, the cell count chosen for the simulations during the optimization process is considered to be adequate without further analysis.

5.4 Extrapolation of forces

To reduce the computational effort during the optimization process, only two propeller revolutions were simulated. During the reference simulations in 3.1, a minimum number of 3 revolutions was found necessary in order for the forces to reach a sufficient level of converge. However, upon closer examination of the output data obtained from the first 8 variants generated by the Sobol algorithm, two effects could be observed.

Even with the simulation setup and input parameters held exactly the same as during reference simulations, the convergence of forces took one more revolution to reach a satisfactory level. The chart given in figure 5.2 shows the convergence of total torque for the first 4 rotations of the simulation. No specific reason could be found for this type of behavior but in order to allow the simulation of a sufficient number of design variants, running each computation for a total number of 4 revolutions is disadvantageous.

Closer examination of the moment and force output shows that the progressions of the different variants share distinct similarities for all 8 designs. This leads to the conclusion that one might be able to get an accurate prediction by simply extrapolating the results from before convergence is reached.

To proof this a valid procedure, the results obtained from the first 16 simulations (Sobol design variants #0 to #7, each at J_1 and J_2) are examined. The graphs in figure 5.3 show the described similar convergence behavior of moments over a range of 4 revolutions simulated. A very similar observation can be made when plotting the total thrust. Figure 5.2 shows the difference in thrust calculated after simulating 2 revolutions as opposed to running a total of 4. A noticeable difference in the resulting measure can be observed for each design variant. However, apparently the offset seems to be very similar in all cases. This might allow to extrapolate the result with sufficient accuracy which cuts the computational effort of each simulation down to almost 50 %. In order to

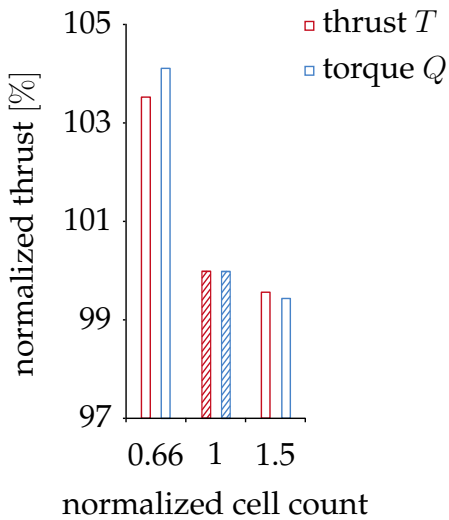


FIGURE 5.1: Examination of grid convergence for the optimized thruster design. The initial grid, consisting of approximately $2.5e6$ cells, is coarsened by a factor 0.66 and refined by a factor of 1.5, respectively. The total thrust and torque of the thruster are normalized according to the initial mesh as to show the solutions dependency on the mesh resolution.

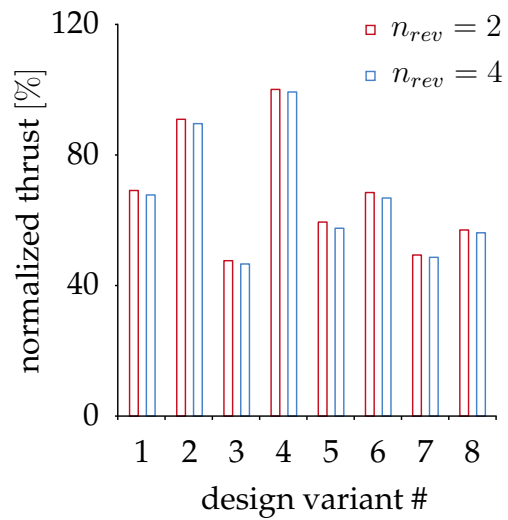


FIGURE 5.2: Comparison of CFD results obtained after simulating 2 complete propeller revolutions and after running the simulation for a total number of $n_{rev} = 4$ revolutions and with the advance coefficient set to $J = J_1$. As a measure of interest, the total thrust of each variant is evaluated and normalized according to the maximum thrust generated by design #4.

do so, the thrust and torque results for all 16 simulations are compared and the average offset between 2 and 4 revolutions is calculated. For the accuracy of said procedure, the magnitude of this offset alone is of no great importance. However, as this technique will be applied to many different variants, the relation of standard deviation and average offset allows for a far better estimation of the accuracy.

The results obtained are an average offset in thrust of:

$$\Delta T = 1.02 \cdot 10^{-2} N \quad , \quad (5.8)$$

which equals approximately 2 % of the average thrust. In terms of torque, the average offset is calculated to be:

$$\Delta Q = -2 \cdot 10^{-4} Nm \quad , \quad (5.9)$$

which also refers to approximately 2 % of the average torque.

$$(5.10)$$

Both thrust and torque are found to be slightly overestimated if only two revolutions are simulated. The Standard deviations of the offset values for all

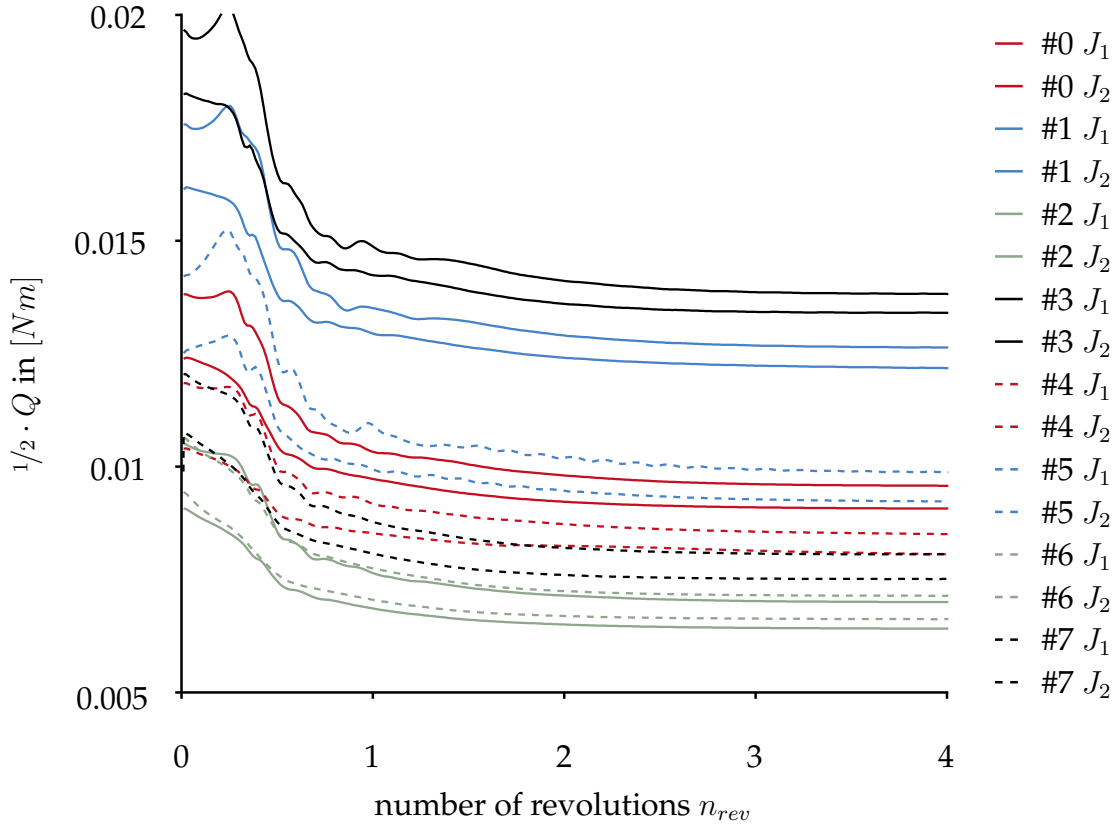


FIGURE 5.3: Convergence of torque as it can be observed after running the simulation for a total of 4 propeller revolutions. The key note taken from this chart is the fact that all 16 simulations apparently exhibit a very similar progress, especially during the last 2 rotations. This allows for the assumption that it might be sufficiently accurate, to extrapolate the results instead of simulating the complete number of propeller revolutions for each variant.

16 simulations are calculated to be:

$$\sigma_T = 5 \cdot 10^{-3} N \quad \text{and} \quad (5.11)$$

$$\sigma_Q = 8 \cdot 10^{-5} Nm \quad . \quad (5.12)$$

These values refer to approximately 1.8 % and 0.8 % of the average thrust and torque.

Based on these observations and qualitative assessments all the remaining simulations of the optimization process have been shortened to run for only 2 revolutions. After the process is finalized, the accuracy of performance prediction shall be validated for the optimized design. Therefore, the simulation that was performed in order to validate the approximation of the self propulsion point in 5.1, is reset to run for an additional 2 revolutions.

The extrapolation based on $\Delta T = 0.0102 N$ and $\Delta Q = 2 \cdot 10^{-4} Nm$ after 2 revolutions led to an extrapolated total thrust and torque of:

$$T_{total,extrapolation} = 0.6189 N \quad \text{and} \quad (5.13)$$

$$Q_{total,extrapolation} = 0.0172 Nm \quad . \quad (5.14)$$

The additional simulation time proves these extrapolations to be as accurate as expected, as the actually calculated total thrust and torque after a total number of 4 revolutions are obtained at:

$$T_{total,simulation} = 0.6250 N \quad \text{and} \quad (5.15)$$

$$Q_{total,simulation} = 0.0173 Nm \quad . \quad (5.16)$$

These measures refer to an accuracy of 99.02 % and 99.42 % in the prediction of thrust and torque, respectively. This level of accuracy is sufficient to do a qualitative, as well as quantitative evaluation of the various thruster designs. However, as equations 5.11 and 5.12 already suggest, this procedure holds only valid for small corrections as in the case at hand. As it allowed to cut computational costs down to almost 50 % it still proved to be highly valuable as it still improves the results accuracy at only minimal effort.

5.5 Residuals

As an additional criterion the residuals are examined, as they are of great importance when assessing convergence. The chart given in figure 5.4 shows a progression of the residuals of pressure p and axial velocity v_x very similar to the results of the reference simulation given in figure 3.4. This time not only the initial residual of the first Pimple-iteration of each time step is given. However, this measure can be seen within the chart when looking at the upper limit of the values throughout the entire 4 revolutions simulated. Within each loop, a sufficient number of iterations is executed until the solution is considered converged within this time step. The initial residuals of the last iteration before the algorithm advances in time by one step, can be visually seen as the lower boundaries of the two curves. The decreasing residuals in between the first and last iteration are not visible at this scale but also not as significant. The number of iterations necessary to reach the level of convergence within each loop that triggers a new time step, varies. It ranges from a maximum of 38 iterations in the beginning of the simulation to a constant 13 iterations towards the end.

From looking at the resulting forces and moments as they are given in figure 5.3 and for a problem like this in general, one would actually expect a steady-state solution. Hence, the graph of the residuals in 5.4 is not very satisfying as this would mean constant low residual values once convergence is reached. However, the graph hardly differs from the results obtained during the reference-simulations in chapter 3. A reason for the observed behavior might be errors introduced by bad matching of single faces within the AMI interpolation algorithm, as already discussed in section 3.4. Based on those

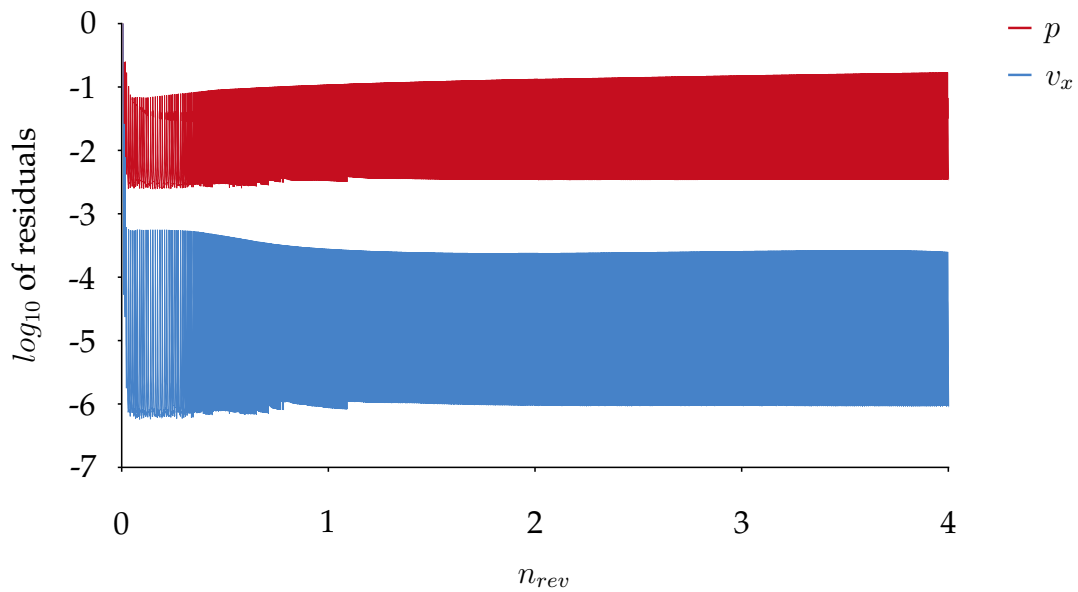


FIGURE 5.4: Initial residuals of pressure p and axial velocity v_x over the extended simulation (see section 5.4 for reference) of 4 revolutions. The evaluation is given for the optimized design variant and the residuals are given for all inner iterations executed within the Pimple-loops.

considerations and since a good level of agreement between the simulation and experimental data has been found in the preliminary reference-simulations, the same level of convergence is rated as sufficient at this stage again.

Chapter 6

Conclusion

6.1 Optimized thruster

This section will give an overview of the final design chosen for the application. The term 'optimized' is used throughout this thesis referring to this variant, although certain constraints need to be kept in mind. Strictly speaking, the terminology is meant to describe the best variant found within the active limitations such as the parametric model, deficiencies of evolved methods or limited computational resources.

6.1.1 Geometry comparison

Starting out from an initial design, the optimized thruster geometry is determined during the optimization process. Hereby, the baseline design is set based on considerations regarding the characteristics of ducted, rim-driven thrusters in general, as well as an initial propeller design as described in the corresponding sections 4.1.2 and 4.1.3.

Figure 6.1 shows a comparative view of the nozzles section in the baseline, as well as optimized variant. The corresponding design parameters are listed and the rim is highlighted in red color. The baseline design can be characterized as symmetrical with all 6 parameters of the CST equations set to equal values. After the optimization process, the resulting nozzle section is found to be angled at $\alpha_{nozzle} = 4.8255^\circ$. The resulting nozzle tapers towards the trailing edge and the flow is accelerated. Out of the 6 CST parameters defining the nozzle section, I_1 and I_2 where set as design variables. The absolute value of I_1 is reduced down to $|I_1| = 1.3422$ resulting in a chamfered inlet region of the nozzle. This allows a more gradual acceleration of the inflow and results in a slightly sharper leading edge. At $|I_2| = 2.8078$, the middle section of the inside profile is more bulbous compared to the baseline design which causes the electric motor to be positioned more aft then in the initial configuration. Due to the complex nature of the optimization problem it is hard to say what exactly causes the increased performance of the optimized design, especially as it will be a combination of multiple affects. Therefore, it can not be said weather the shift of the propeller plane in axial direction is favorable in itself or just a side effect of the superior set of design variables of the optimized nozzle. It is however interesting that the cross-section of the nozzle is the smallest in the

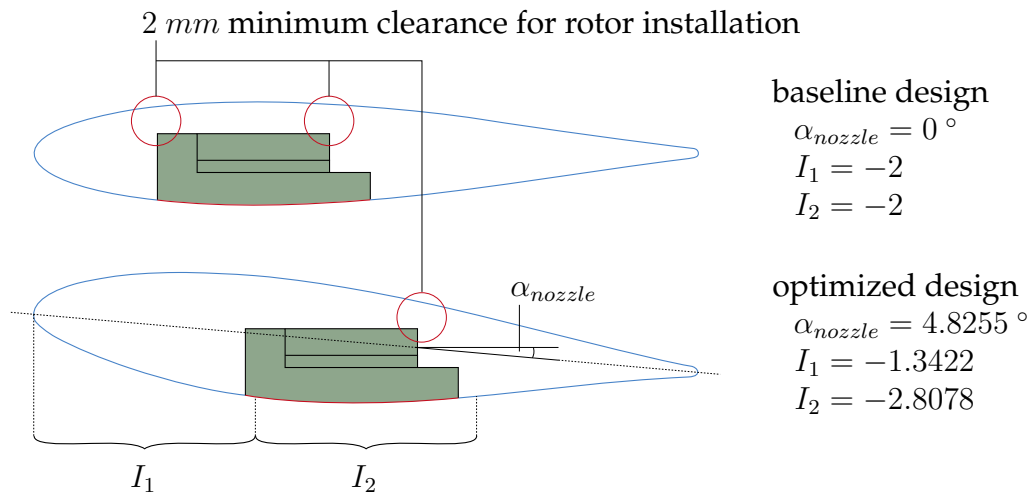


FIGURE 6.1: Comparison of the nozzles section-design of the baseline (top) and optimized (bottom) variant. The parameters defining the geometry are listed along with the corresponding section views and their influence on the resulting geometry can be conceived visually. The rotor part of the BLDC motor driving the propeller is shown schematically and split up into the propeller's ring on the inside, surrounded by an iron ring and an array of permanent magnets. The minimum clearance set within the algorithm for positioning of the motor is satisfied and the critical edges are highlighted by red circles.

baseline design and still, the more voluminous section of the optimized variant yields higher performance. The unintuitive nature of results like this are a great example for the potentialities of optimization algorithms and their use along with simulation-driven design.

As already mentioned earlier, the positioning of the BLDC motor within the nozzle is handled by a script which can be found in the digital appendix accompanying this thesis. In figure 6.1 the rotor part of this motor is shown schematically and the critical edges are highlighted. As it can be seen, the nozzles section is not scaled to an absolute minimum in thickness, but an additional 2 mm of clearance are kept to ensure the necessary structural integrity of the design. The algorithm hereby pays attention to all 3 outside edges of the rotor, as different edges can cause collision when scaling down the section in thickness. In the baseline design, further scaling or a shift of the motor to the left or right would cause a violation of the collision criteria in the top left or right corner, respectively. However, in the optimized design, scaling or any shift to the left or right would cause a violation only in the top right corner.

The blade, as described in the corresponding section 4.1.3 is shown as a linesplan in figure 6.2 and can be compared to the optimized variant which is also given in the same drawing. The distinct shape of a winglet at the blade tips can be seen. In both cases, this does not extent around the leading edge of the blade to not risk problems with entanglement of the propeller. The impact of the parameter Δc on the blades shape can be seen clearly when comparing sections of constant radius. At $\Delta c = 1.7172$ a significant amount of camber has been

found to be beneficial. Although no unit is specified for this design variable it can be translated to an offset of 1.7172 mm in the center of the section. The exact distribution of chamber is defined via a B-Spline curve within a CAESES-feature and can be reconstructed based on the digital appendix to this work.

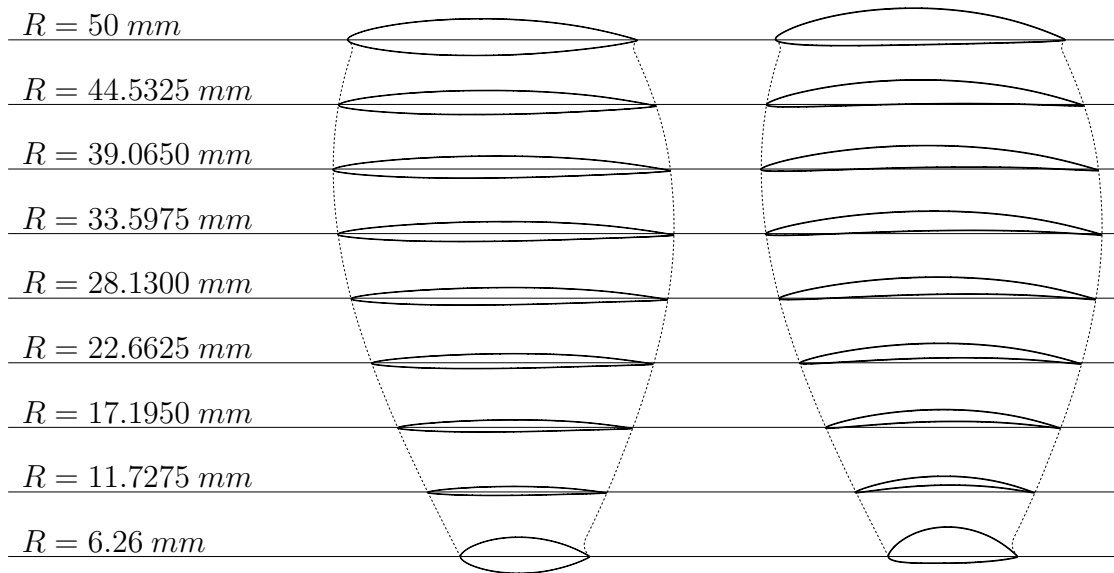


FIGURE 6.2: Linesplan of the baseline (left) and optimized (right) blade design. The winglets at $R = 6.26 \text{ mm}$ can be seen, as well as a significant amount of chamber for the optimized variant.

The second parameter that distinguishes the optimized blade shape from the baseline design is the pitch-to-diameter ratio of the propeller. As in CAESES this value is manipulated by the design variable $\Delta\alpha$, the actual distribution of P/D as a function of radius is given in the same unit as well. Although not very common, this description is maintained throughout this thesis to allow better comparison to the parametric model given in the digital appendix.

Figure 6.3 shows the two curves of $\alpha = 90 - \arctan(P/\pi D)$ as a function of the radius. As the variable radial distribution has been disabled within CAESES during the optimization phase, the optimized version of the graph is simply a vertical shift of the baseline's distribution by $\Delta\alpha = -4.4961^\circ$.

Prior to the exploration algorithm a choice on the parameter boundaries had to be made and $\Delta\alpha$ has been set to the interval $[b_l = 0^\circ, b_u = 10^\circ]$. Due to the considerable impact of the frictional losses in the gap-flow within rim and nozzle on the efficiency, the rotational speed of the propeller was expected to be reduced. This would lower the amount of energy dissipation within the gap and thus increase the open water efficiency of the thruster. As a reduced rotational speed at the same ship speed generally requires a higher propeller pitch, one might choose a lower boundary $b_l < 0$. However, the initial blade design was meant to be used along with an accelerating type of nozzle and therefore based on an inflow velocity of $v_a = 3 \text{ m/s}$. To account for this assumption, P/D needs to be reduced significantly and therefore the lower boundary was chosen

to be $b_l = 0$. In other words, it was assumed that the reduction of rotational velocity which asks for a higher pitch is outweighed by the assumption of a too high inflow velocity which needs to be counteracted by a lowered pitch.

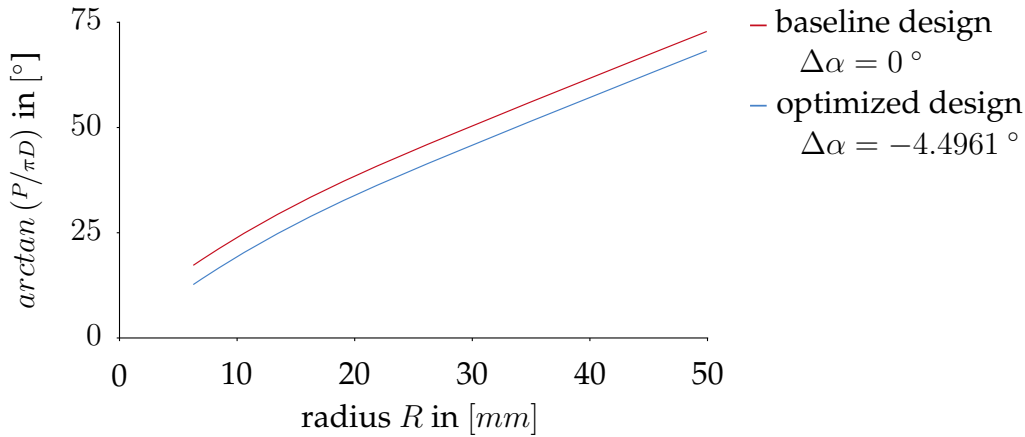


FIGURE 6.3: Radial distribution of propeller pitch comparing the baseline and optimized thruster geometry. As the design variable $\alpha_{distribution}$ has been disabled and $\Delta\alpha = -4.4961^\circ$ for the optimized thruster, the blue graph is simply a vertical shift of the baseline's distribution.

After finishing the exploration phase, the two best designs were both found to have values of $\Delta\alpha < 1$ in common. This shows that the assumption on the impact of reduced rotational speed versus overestimation of inflow velocity did not hold true as expected. Consequently the lower bound is adjusted to $b_l = -5^\circ$ during the optimization which proved to be a very valuable decision, as the optimized design features a value of $\Delta\alpha$ as low as -4.4961° .

For a more visual impression on the baseline and optimized thruster design, the figures 6.4 and 6.5 are given in the following section 6.1.2. The left view in both figures gives an impression on the overall design and provides a good comparison towards the reference-design of the Ka4-70 propeller in a MARIN Nozzle 19A (see figure 2.4). In the section view, again, the cross-section of the nozzle can be seen along with the rim and blade positioning in axial direction. Finally, the view from the direction of inflow gives a good impression on the disc area ratio which is very similar in both cases at 20.98 % for the baseline and 19.00 % for the optimized variant. Furthermore, this view shows the greater projected area of the optimized nozzle due to its tapered shape.

6.1.2 Visualization

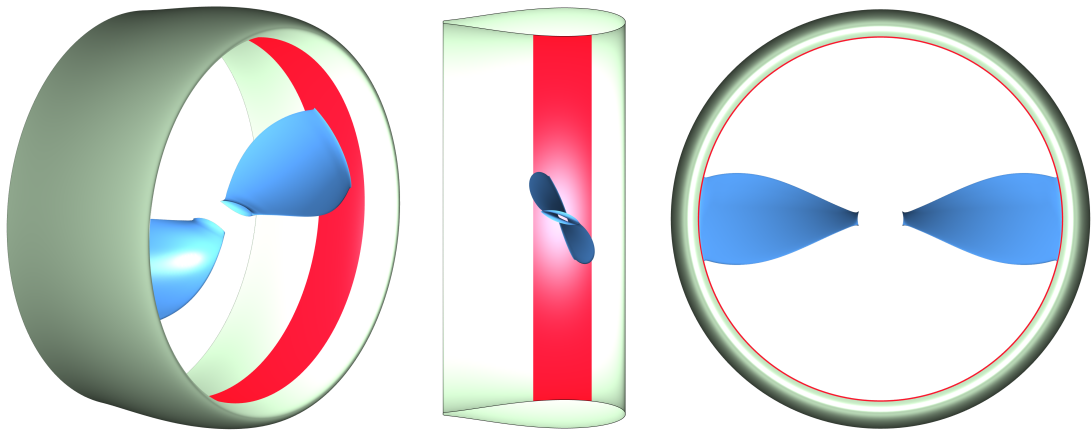


FIGURE 6.4: The images show the baseline thruster design, as it is specified by the parameters given in table 4.1. From left to right, an angled view, a Y-section view and a front view in direction of inflow are given. Compared to the optimized design the rim and blades are located closer to the leading edge, as this allows for the thinnest possible nozzle section that still provides installation space for the electric motor. The nozzle section is symmetric and the propeller blades remain unchanged.

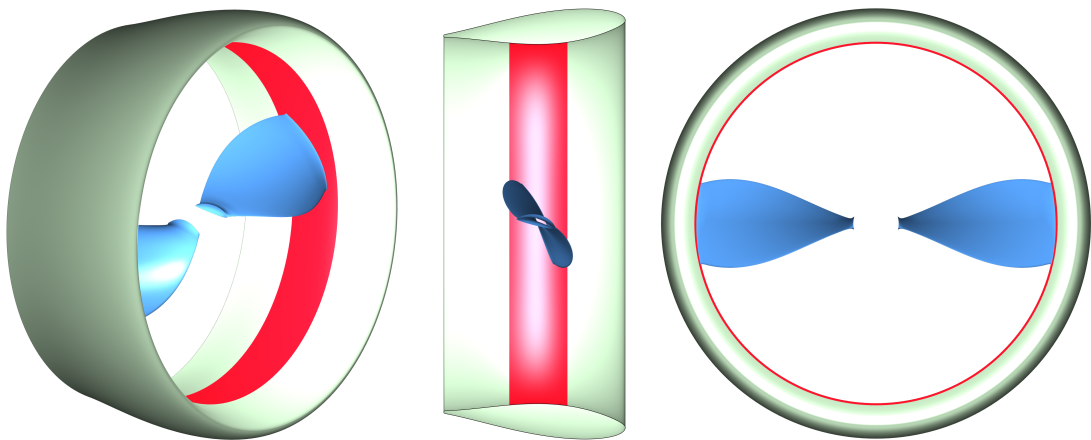


FIGURE 6.5: The parameters defining the optimized thruster design are given in the bottom line of table 4.4. While the parametric CAD model still ensures sufficient installation space for the electric motor, the rim and blades have shifted towards the middle. The nozzle section no longer remains symmetric and the duct is tapered towards the aft, thus resulting in what is commonly known as an accelerating duct.

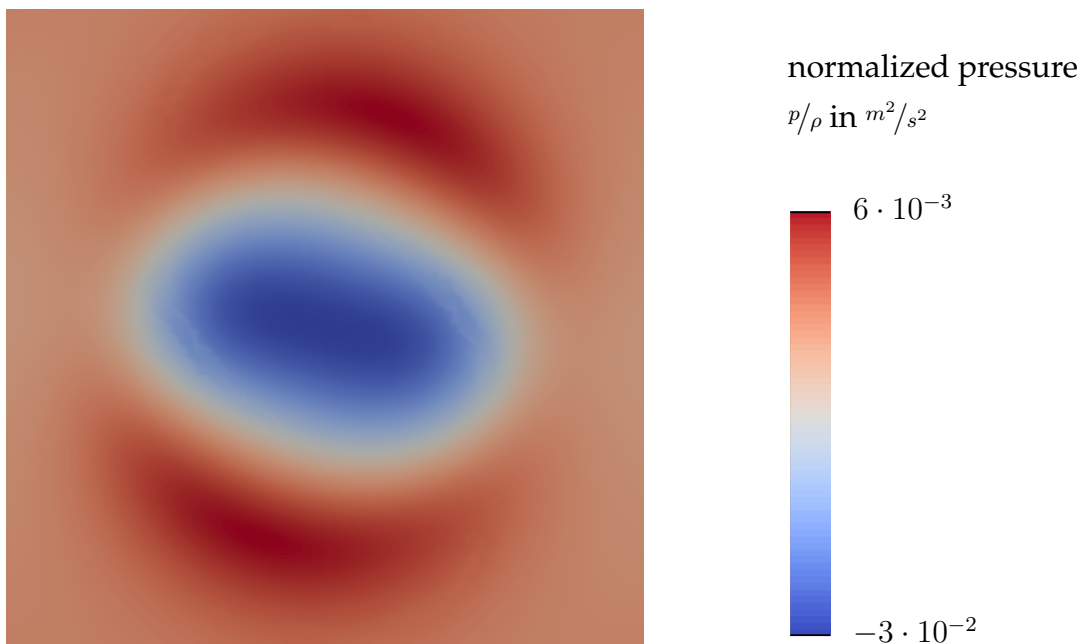


FIGURE 6.6: Distribution of density-normalized pressure upstream of propeller plane at a distance of $R = 50 \text{ mm}$ (one propeller radius). The blue area is created by the suction of the propeller blades. As they are only two in number, the shape is rather elliptical as opposed to a circular shape commonly seen with multi-blade propellers.

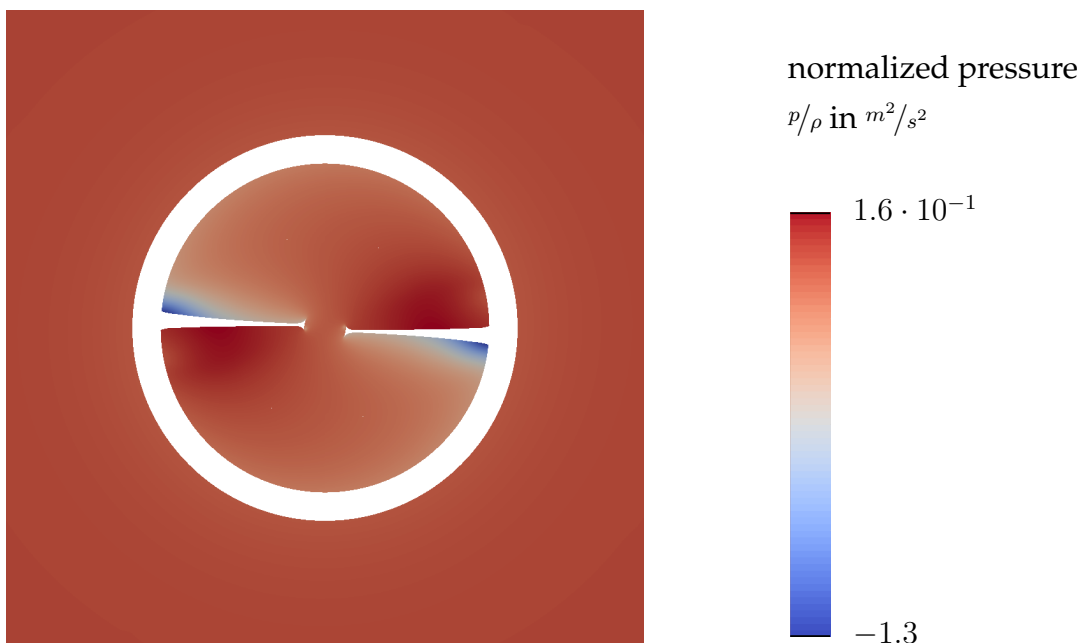


FIGURE 6.7: The distribution of pressure in the propeller plane clearly shows the pressure and suction sides of the blades. As the rim-drive is a hubless design, winglets are added to reduce the formation of tip vortices facilitated by this pressure differential.

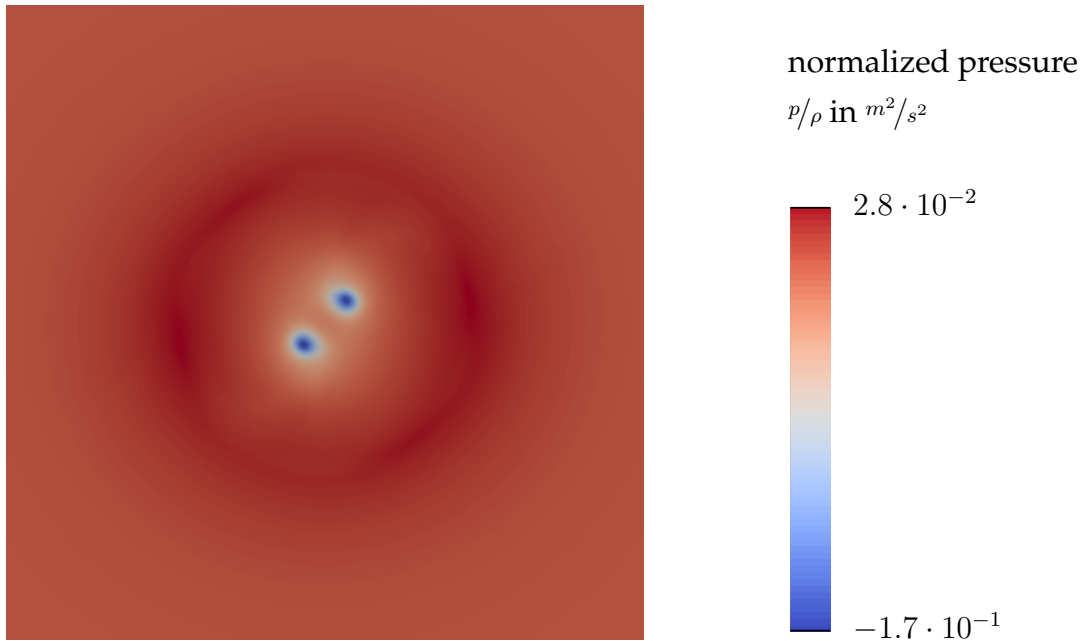


FIGURE 6.8: The figure shows the distribution of normalized pressure at a distance of one radius ($R = 50 \text{ mm}$) downstream of the propeller plane. An area of higher pressure, circular in shape, can be observed in the nozzles wake due to the boundary layer adjacent to the nozzle that decelerates the flow. Furthermore, two tip vortices can be observed, clearly indicated by the low pressure areas near the center plane.

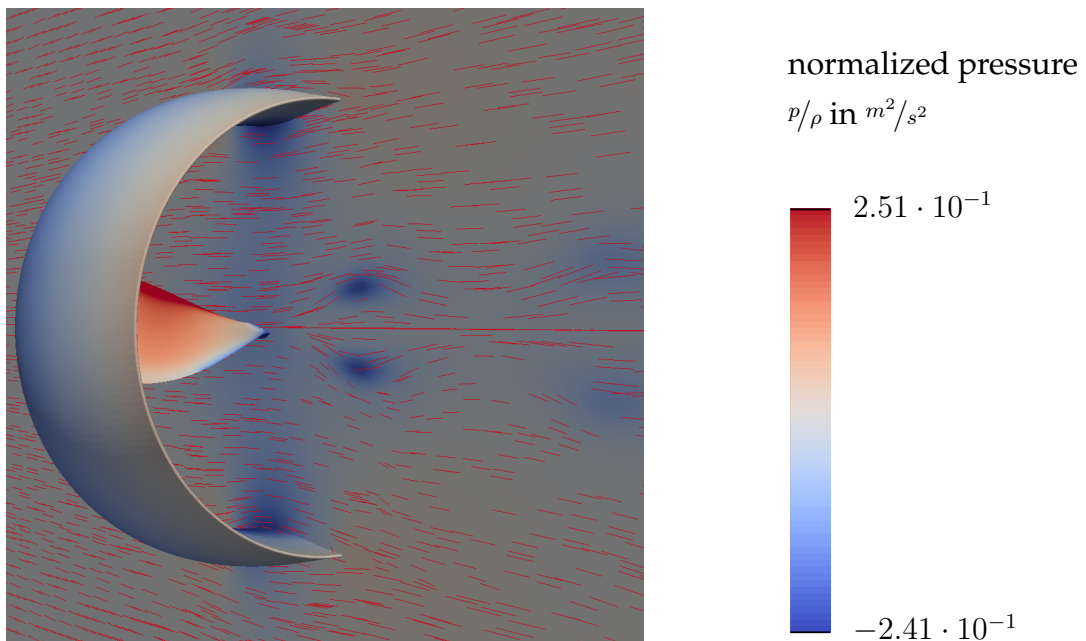


FIGURE 6.9: The pressure distribution on thruster surface, as well as on the symmetry-plane is shown. The pressure side of the blade faces the viewer as can be clearly identified by its red color. The tip vortices already visible in figure 6.8 can be seen, emphasized by the velocity-vectors on the symmetry plane. Furthermore a light red color on the nozzles outside, near the trailing edge indicates the overpressure that acts on the angled surface in this region and thus, causes the nozzle itself to generate thrust.

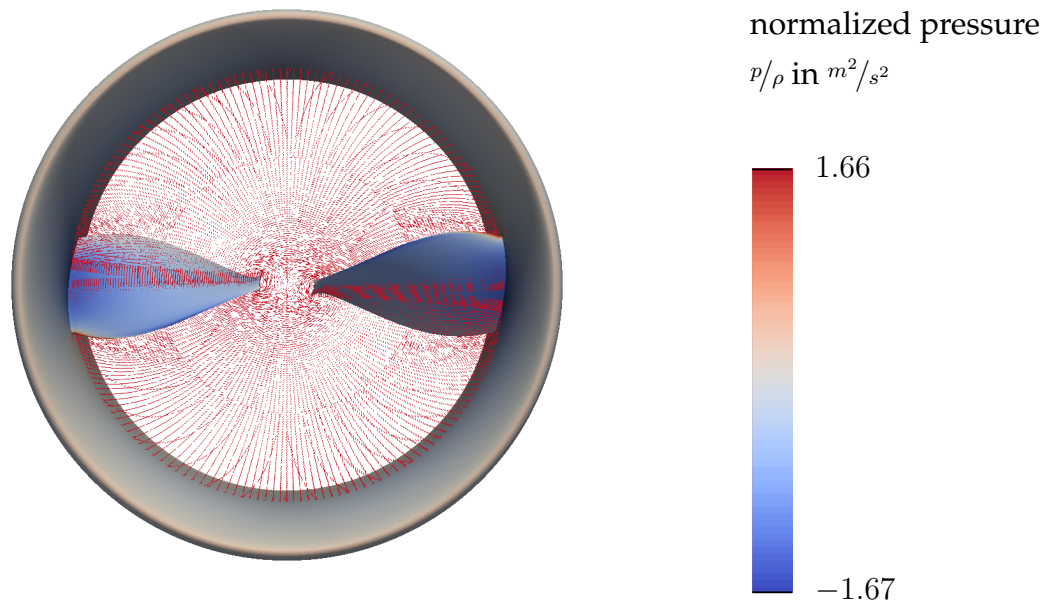


FIGURE 6.10: The front view into the nozzle shows the suction side of the blades and the stagnation point on the leading edge of the nozzle. The rotation induced into the fluid is distinctly shown by the velocity vectors close to the axis of rotation.

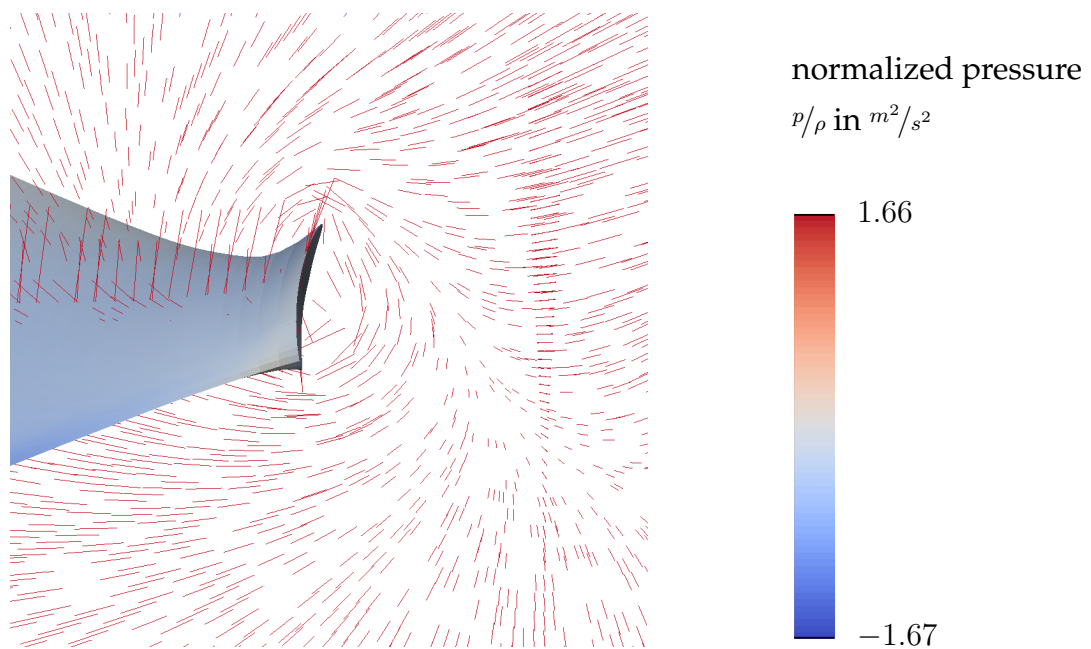


FIGURE 6.11: The image shows a detailed view on one of the blade tips shown in the previous figure 6.10. The swirling motion of the tip vortex forming around the blades edge is shown by the 2D vectors of the velocity in the propeller plane.

6.1.3 Performance

When judging the performance of the optimized thruster design, not only the objective itself is regarded. For a better understanding of the efficiency achieved by the optimized design, the generated thrust can be split into separate components originating from the single thruster elements such as nozzle, rim and propeller blades. Information can also be gained by splitting the torque into a part originating from the blades and a second one arising from the rim. A lot of work has been put into the correct estimation of the frictional losses within rim and nozzle and a significant influence on the design resulting from this energy dissipation can be monitored. Finally, one characteristic of the optimized design that has been neglected during the optimization process can be assessed now. Theoretically the highest possible performance of the thruster is desirable and the optimization algorithm therefore is focused solely on maximizing said performance. However, due to small possible errors such as manufacturing tolerances or inaccuracy of the CFD simulations the result might vary slightly. At this point the importance of a robust design becomes relevant, meaning that a small variation in geometry or minor computational errors should preferably not impact the performance significantly. Hence, the solutions robustness, if not considered as an objective or constraint during the optimization process already, needs to be examined afterwards as it might influence the choice of design that suits the application best.

As mentioned before, the splitting of total thrust into its separate components allows a more detailed insight into the working principle of the thruster. The three thrust components generated by the nozzle, rim and propeller that add up to the total thrust generated by the unit can be divided into:

$$T_B = 95.65 \% \quad , \quad (6.1)$$

$$T_R = 1.04 \% \quad \text{and} \quad (6.2)$$

$$T_N = 3.31 \% \quad (6.3)$$

of the total thrust $T_T = 100 \%$. In the introductory chapters 1.1 and 1.2, it has been assumed, that no substantial benefit in terms of efficiency can be anticipated due to the use of a nozzle in the application at hand. Instead, the decision for this particular kind of propulsion device is based on other characteristics such as its unlikeliness of getting entangled. The propulsive efficiency of ducted propellers compared to conventional ones usually only increases towards bollard pull condition [22]. The reason for this behavior is the large amount of thrust generated by the nozzle itself in this condition. However, in the application at hand bollard pull is not considered a relevant operating condition and thus high performance at a low coefficient of advance is not beneficial. This assumption led to the conclusion that, if the nozzle itself is unlikely to contribute much to the total thrust, it should be designed in a way that minimizes drag and thus does not show too much of a negative impact on the efficiency. With the amount of thrust generated by the nozzle at $J = J_d$ being only $T_N = 3.31 \%$, this prognosis has proven correct. Figure 3.6 shows a comparable thruster generating more than 45 % of its total thrust through the nozzle at

$J = 0$. At $T_N = 3.31 \%$, the efficiency of the optimized design is not reduced due to the use of a nozzle but the total thrust, at $T_B = 95.65 \%$, is still mainly generated by means of the propeller itself.

Based solely on this observation one might assume an open water efficiency of the thruster comparable to conventional propellers. A closer examination of the torque and its components shows why this is not the case. The CFD results can be split up analogous to the thrust components into:

$$Q_B = 89.61 \% \quad \text{and} \quad (6.4)$$

$$Q_R = 10.39 \% \quad . \quad (6.5)$$

A too simplistic calculation, neglecting the presence of the propeller's ring, leads to an open water efficiency of $\eta_o^* = 0.63$. When including the torque acting on the rim as obtained from the viscous flow simulation into the calculation, the efficiency is reduced to $\eta_o^{**} = 0.57$. However, the results in table 5.1 show an open water efficiency of $\eta_o = 0.32$. This result is based on the results from the flow simulations as well as the estimation of additional frictional losses inside the gap within rim and nozzle. The comparison of η_o towards η_o^* and η_o^{**} shows the significance of the energy dissipation caused by the rim. Although η_o^* still does not match the performance that might be achieved with a well designed two-bladed conventional propeller, it still shows the massive disadvantage of a rim-driven thruster at the given operating condition. Reasons for η_o^* still being comparatively low might be the flow acceleration inside the nozzle which increases viscous drag on the blade surfaces, or the uneven inflow velocity caused by the nozzle which requires careful setting of the radial distribution of P/D .

Besides the fact that the decision towards a rim-driven thruster was not made based on efficiency considerations, the impact of the dissipative losses of a RDT on the vessels speed are well within acceptable limits. Early concept formulations of the ASV the thruster is designed for ask for an average speed of $v_s = 1.5 \text{ m/s}$ to allow proper operation. At $v_s = 1.46 \text{ m/s}$ for the optimized variant this target value has been closely matched. Without frictional losses due to the gap flow the overall efficiency would almost double. However, even after an assumed increase of efficiency of 200 %, the design speed rises only by a factor of approximately $\sqrt{2}$ or energy savings of around 7.5 Wh per hour could be expected. While both would be favorable for the given application, none would change the actual feasibility of the project and the original reasons for choosing an RDT over a conventional propeller are still considered more relevant.

As already mentioned, the robustness of the design is another important point that needs careful consideration. When comparing the results of the optimized design variant towards the baseline, the characteristics in terms of robustness are adequate as can be seen from the results given in the chart in figure 6.12. While the curve of $\eta_o(J)$ for the baseline design reaches its maximum at $J \approx 0.78$, the optimized design does so at a considerably higher advance coefficient of $J \approx 1$. As a result, besides the higher efficiency, the graph of $\eta_o(J)$ for the optimized design is also scaled up along the abscissa of the open water diagram. This means, that small changes along this horizontal axis do not result

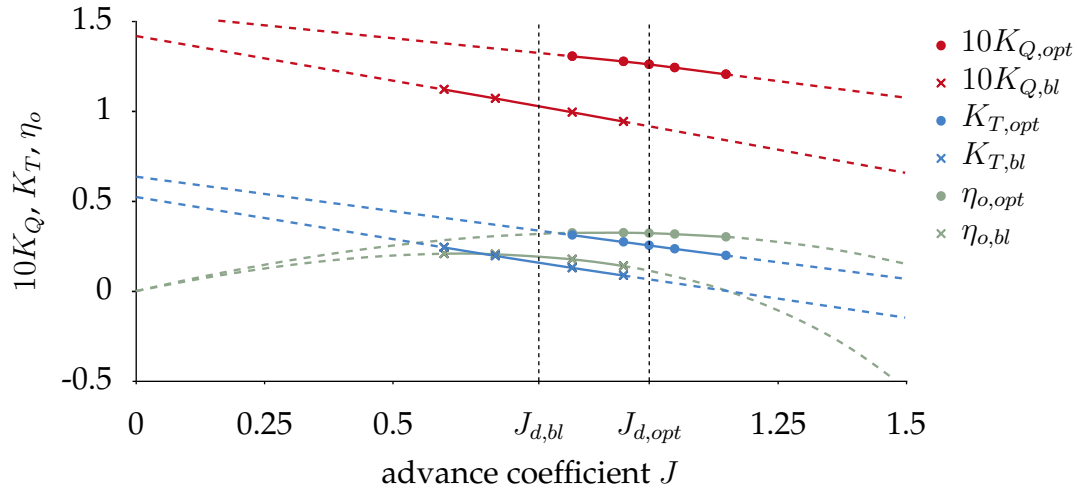


FIGURE 6.12: The given chart shows the open water characteristics of the baseline thruster, as well as the optimum design found. The dashed lines represent the extrapolation area, while the solid ones cover the area of interpolation. The exact values obtained from the viscous flow simulations and empirical correction of frictional losses are represented by the markers. A significant increase in open water efficiency can be observed, as well as a shift of maximum efficiency towards higher J for the optimum design.

in a large variation of the efficiency. In other words, the open water efficiency is robust towards small variations in J . This characteristic is of great importance for a number of different reasons. Uncertainties in preliminary assumptions, but also errors within the flow simulations and empirical models are one reason why in practice the advance coefficient might be off to some degree. More importantly however, external forces, such as waves, wind or current acting on the hull can have significant impact on the advance coefficient the vessel is operating under. As no sea margin has been applied, the importance of this wide and flat progression of $\eta_o(J)$ is even more relevant.

The actual reason behind the optimization algorithm converging towards higher advance coefficients is, however of a different nature. Upon close examination of all the variants generated during the exploration and subsequent optimization phase a certain correlation can be noticed. When sorting the designs in increasing order according to their performance in terms of the objective measure v_d , J_d also increases, while n_d decreases with every single variant. With the large influence of the frictional losses in mind, this behavior becomes intuitively clear. As the friction increases quadratic with increasing rotational velocity, lower n_d results in higher efficiency and therefore increased ship speed. At the same time, a lower rotational speed results in a higher coefficient of advance. Hence, the robustness although not included into the optimization algorithm as an additional constraint increases along with the objective v_d . Subsequently the variant of highest performance also provides maximum robustness and is chosen as the optimum design.

A different kind of robustness can be observed when comparing the performance of various design variants that vary only slightly in shape. This becomes an especially important attribute with manufacturing tolerances in mind or due to possible wear out of the final product over time. The variants listed within the tables 4.4 and 4.5 allow a good judgment of this quality. Looking at the best 5 designs listed in the bottom 5 rows of table 4.5, only very minor differences in terms of the propulsive characteristics can be observed. In the corresponding rows of table 4.4 the geometry parameters of those 5 designs are listed and although rather small, their relative changes are much larger than those observed in the resulting performance. The decreasing changes of the design variables towards the end of the optimization phase also show a very good convergence of the algorithm within the relatively small number of design variants examined.

6.2 Re-evaluation of invalid design variants

In the tables 4.4 and 4.5, a total of 6 variants are shown grayed out. Those are invalid designs as their propulsive characteristics have been calculated erroneously during the optimization process. As one can see, these variants show a comparatively low design speed at higher open water efficiency than others. The design advance coefficient of all these variants is given as $J_d = 1$ in table 4.5. However, this is simply because advance coefficients $J_d > 1$ are not accounted for within the estimation of the self propulsion point, as J_d was not expected to increase this much. As a consequence, their performance is calculated incorrect, as one can see when calculating the power consumption. For example, at $P = 13.55 \text{ W}$, design #8 does not use the total amount of available power which causes an underestimated performance in $v_{d,0}$. After adapting the script to allow for values of $J_d > 1$, it shows that in fact the performance of the affected designs is better than anticipated.

As has been explained in section 4.8, the results given in table 4.5 are only based on a first estimation of the propulsion point. However, after the first iterative re-evaluation of the performance, all but the designs #8 and #11 lie within $J_d < 1$. In both cases at $J_d = 1.0004$, the algorithm allowing $J_d > 1$ did not result in a significant difference towards the initially estimated advance coefficient.

After the first re-evaluation and with the algorithm adapted to allow for $J_d > 1$, the qualitative ranking of the affected variants changes. It has to be noted at this point, that in fact all designs regarded as invalid before, outperform the design which was previously considered the optimum. However, at between 0.00505 % to 0.105 % increased v_d , compared to design #16, this does not affect any of the drawn conclusions or the choice of the optimum variant. As a matter of fact, the differences in geometry of all 7 designs are presumably within the manufacturing tolerances. However, the adaptation of the script to allow for $J_d > 1$ still shows a huge significance of this limitation.

The initial restriction of J_d towards values $J_d \leq 1$ acted on the optimization algorithm in a similar way, as a penalty function would have done. Due to the erroneous calculation of the advance coefficient, the available power of

$P = 15 W$ was not exhausted for the affected variants (see figure 4.4 for a better understanding of this correlation). As a result, the design speed of those variants has been underestimated. In consequence, the optimization algorithm converged towards the variant of maximum performance, that did just not violate this limitation. The first time a penalty was applied was with the evaluation of design #8. From this point onwards, the surrogate model has been manipulated in an unwanted manner, resulting in the convergence towards $J_d = 1$. After the re-evaluation, one can see, that the actual improvement from design #7 to #8 adds up to 0.38 %. This suggests the assumption, that substantial potential performance has been lost at this point, as further convergence towards $v_{d,max}$ at advance coefficients $J_d > 1$ might have happened at a similar rate of improvement.

6.3 Summary

The scope of this work originates from the design and construction of a small unmanned ASV targeted to cross the Atlantic. A short overview on the particularly challenging tasks within the aXatlantic project is given. A hubless RDT is described as a means of propulsion that meets the special requirements of the underlying task.

Upon research a reference simulation of a Ka4-70 propeller in a MARIN Nozzle 19a is run. Experiments with this exact same geometry carried out by Oosterveld [22] are accurately reproduced via open water simulations. A wall function approach is used and close attention is payed to the treatment of near-wall cells within grid generation. The viscous flow simulations are based on OpenFOAMs dynamic mesh handling capability and the coupling of stationary and rotating region via AMIs. The computation involves only a rotationally symmetric section and extensive studies on the required domain size, time step, number of revolutions simulated, Reynolds number and mesh resolution are carried out. The residuals are monitored and high grid quality is ensured already taking into consideration the automatic grid generation procedure needed during the optimization task. An accurate performance prediction can be made based on this numerical setup, enhanced by existing empirical models accounting for the neglected dissipation due to the gap flow within rim and nozzle.

A fully parametric geometry model of a nozzle is then generated based on CST methodology within CAESES. The CAD model incorporates an optimized utilization of available installation space for the BLDC motor designed specifically for this thruster. An existing propeller geometry is re-parameterized and mayor design variables are introduced. The unappended hull-resistance is measured experimentally in the large towing-tank of TU Berlin and the resulting measures are fitted to a carefully chosen model function based on a least squares approach. The given amount of available power at the propeller shaft, as well as thrust deduction and wake fraction coefficient are estimated. On this foundation, a method of calculating the design speed of the vessel is introduced.

Two separate simulations at different coefficients of advance are carried out for each design variant allowing a precise performance prediction that comprises all the afore-mentioned considerations. As an objective measure, this result is used for an automated optimization process within CAESES. The framework is coupled with the grid generation software Pointwise and a script for automatic grid generation of the variable thruster geometry is compiled. The evolved OpenFOAM setup is attached to the process and the external optimization toolbox Dakota is coupled to CAESES as well. Five design variables are activated within the parametric model and a Sobol-sequence of 25 variants is run. Subsequently a surrogate model is used to further improve propulsive performance using RSM. A well founded decision towards a final 'optimized' design is made based on the obtained results.

A shortcoming in the programming of the algorithm that calculates the objective measure is observed. A re-evaluation is performed to examine the impact on the optimization process. Possible further performance potential is assessed and will be addressed in the outlook given in 6.4.

The geometric and hydrodynamic characteristics of the optimized design are presented in detail and compared towards the initial 'baseline' design. The applicability of assumed simplifications is verified and a number of analyses are run to verify the correctness of the viscous flow simulations. A very high level of accuracy is found and open water efficiency is increased from the baseline by approximately 168 % towards the optimized geometry.

6.4 Outlook

The application of Simulation-Driven Design to the task at hand has proven a very valuable and powerful approach. The results achieved very well match the expectations and the level of performance predicted is considered satisfactory for the underlying ASV. However room for improvement has been found in multiple aspects of this thesis meaning significant further potential.

The generation of each geometry variant through a parametric CAD model and subsequent handling of said geometry by a separate grid generation tool could be simplified a lot. Both aspects take major time in preparation and need to be coordinated precisely in order to function reliable. Hence, a mesh morphing approach is suggested as this technique allows the handling of geometry and mesh as one single component. This method provides substantial benefits over the chosen approach not only in terms of ease of use, but also allows to significantly reduce CPU time in comparable tasks [2].

Further potential lies within the amount of design variables enabled during the optimization. To limit the computational costs within the thesis, only 5 of the available 11 parameters were activated as design variables. Enabling those parameters, or even further expanding the CAD model certainly enables further increase in performance.

A very important future step could also be the evaluation of additional variants based on the existing setup. As the method of performance prediction has

been adapted towards design advance coefficients $J_d > 1$ this could allow significant improvement as outlined in section 6.2. Additionally this might lead to certain design variables reaching the defined boundaries which would involve adjustments on the design space, again.

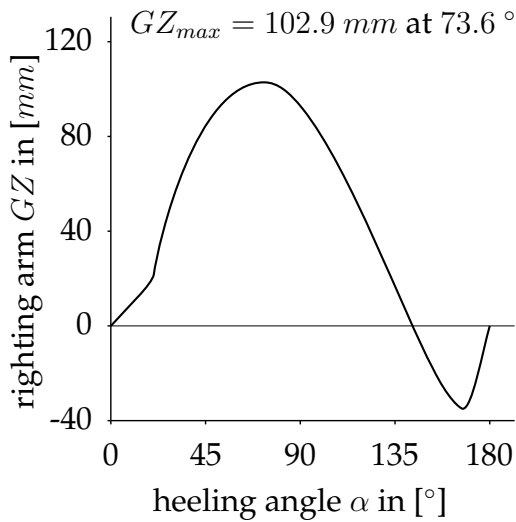
Another promising step could be the expansion of the method of estimating J_d presented in 4.3 towards incorporating the iterative procedure of calculating the quantitative performance as described in 4.8. Technically speaking, this could be achieved by adding another dimension to equation (4.34). In this work, the power consumption has been calculated as a function of J and the abscissa value at $P = 15 W$ has been determined as $J_{d,0}$, based on an initial rotational speed n_0 . A subsequent iterative re-evaluation then lead to the actual result of interest at $n_d = n_i = n_{d,i}$. By adding the rotational speed n_i as another dimension, (4.34) can be written as $P(J, n_i)$. Hence, self propulsion point can be directly obtained as $P(J_d, n_i = n_d) = 15 W$.

Besides the afore-mentioned suggestions which are mainly focused on further optimization of the thruster, the actual realization of the unit yields a completely isolated means of validation. In section 4.3, the comparison of the vessels power consumption versus speed in calm condition is suggested as the simplest way of assessing the accuracy of the performed task. However, in order to gain a more detailed insight into the overall system, further experiments in the towing tank, wave basin or on maneuvering characteristics are a promising option.

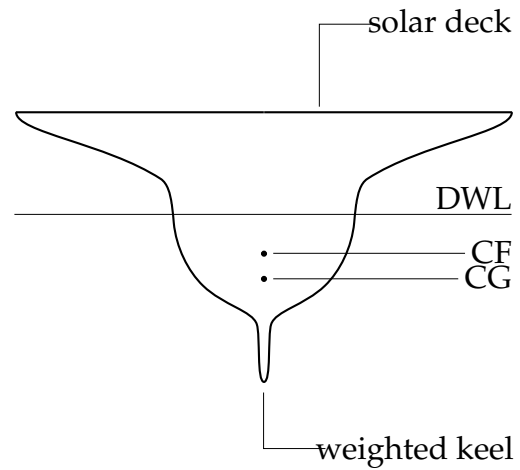
Finally, the maiden voyage of the aXatlantic will provide a great deal of information on a lot of aspects related to the entire design and construction and allow a first judgment of the propulsive efficiency achieved.

Appendix A

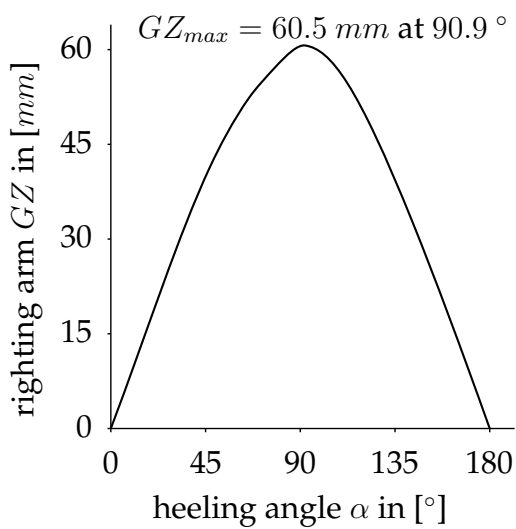
Schematic hull design



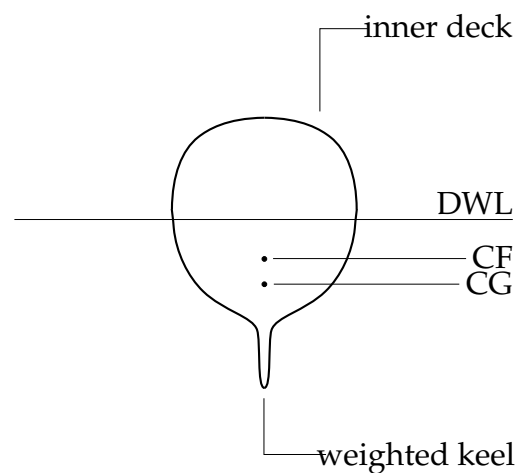
GZ curve of non self-righting outer hull.



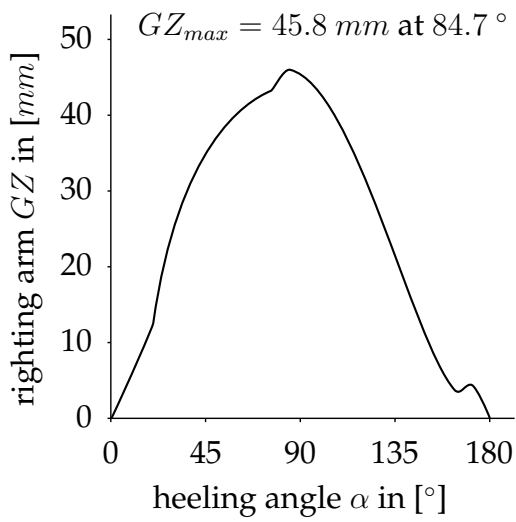
Hull section at $l/L = 0.7$, non self-righting, entirely watertight.



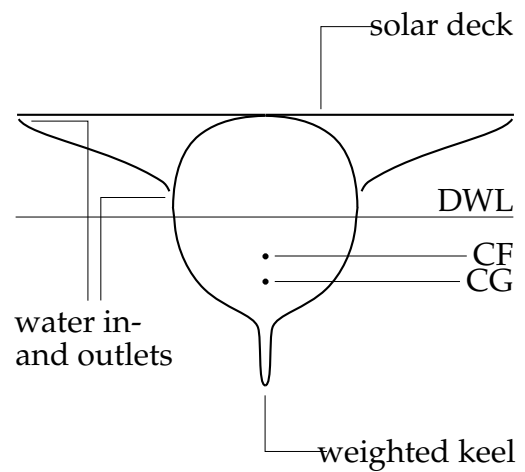
GZ curve of self-righting inner hull.



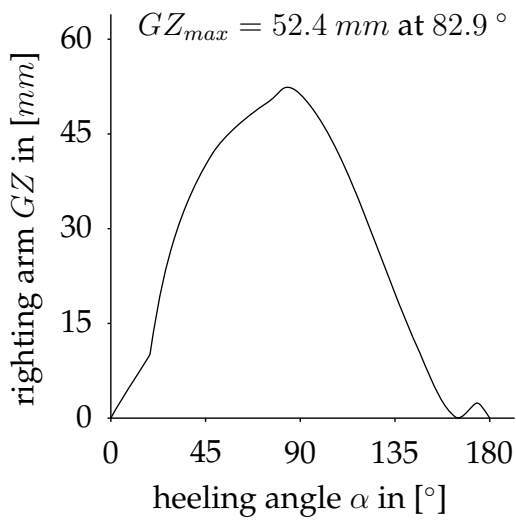
Hull section at $l/L = 0.7$, self-righting, missing solar deck.



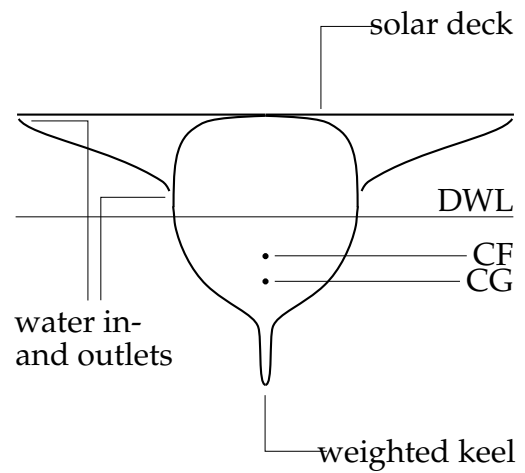
GZ curve of complete hull. Self-righting due to water in- and outlets.



Hull section at $l/L = 0.7$, self-righting, water in- and outlets.



GZ curve of optimized hull. Higher GZ_{max} at lower heeling angle α .



Optimized hull section at $l/L = 0.7$, self-righting, water in- and outlets.

Appendix B

Blade geometry: table of offsets

Table 2

		Dimensions of the four-bladed screws, type Ka 4-70										Length of blade section at 0.6R = 0.3445D if $F_c/F = 0.70$
		r/R	0.2	0.3	0.4	0.5	0.6	0.7	0.8	0.9	1.0	
Length of the blade sections in percentages of maximum length of blade section at 0.6R.	From center line to trailing edge	30.21	36.17	41.45	45.99	49.87	52.93	55.04	56.33	56.44	56.44	
	From center line to leading edge	36.94	40.42	43.74	47.02	50.13	52.93	55.04	56.33	56.44	56.44	
Max. blade thickness in percentages of diameter	Total length	67.15	76.59	85.19	93.01	100.00	105.86	110.08	112.66	112.88	112.88	
	Distance of maximum thickness from leading edge in percentages of length of sections	4.00	3.52	3.00	2.45	1.90	1.38	0.92	0.61	0.50	0.50	
Distance of maximum thickness from leading edge in percentages of length of sections	From maximum thickness to trailing edge, percent	34.98	39.76	46.02	49.13	49.98	—	—	—	—	—	
	From maximum thickness to leading edge, percent	—	—	—	—	—	—	—	—	—	—	

		Table of ordinates of Ka 4-70 series									
		Distance of ordinates from maximum thickness					From maximum thickness to leading edge, percent				
r/R	From maximum thickness to trailing edge, percent	20	40	60	80	100	20	40	60	80	100
0.2 0.3 0.4 0.5 0.6 0.7 0.8 0.9 1.0	—	95.00	97.92	90.83	77.19	55.00	38.75	27.40	—	—	—
	82.40	95.86	97.63	90.06	75.62	53.02	37.87	27.57	—	—	—
	84.14	96.25	97.22	88.89	73.61	50.00	34.72	25.83	—	—	—
	85.69	96.60	96.77	87.10	70.46	45.84	30.22	22.24	—	—	—
	86.42	96.47	96.47	85.89	68.26	43.58	28.50	20.44	—	—	—
	85.89	96.58	96.58	86.33	69.24	45.31	30.79	22.88	—	—	—
	86.33	96.76	96.76	87.04	70.84	48.16	34.39	26.90	—	—	—
	87.04	97.17	97.17	88.09	72.94	51.75	38.87	31.87	—	—	—
	88.09	97.00	97.00	88.00	73.00	52.00	39.25	32.31	—	—	—
	88.00	—	—	—	—	—	—	—	—	—	—
0.2 0.3 0.4 0.5	—	—	—	—	—	—	—	—	—	—	—
	0.1	1.46	1.46	4.37	10.52	16.04	20.62	33.33	—	—	—
	1.77	0.83	0.83	2.72	6.15	8.28	10.30	21.18	—	—	—
	1.07	0.42	0.42	1.39	2.92	4.44	5.89	13.47	—	—	—
0.4 0.5	—	—	—	—	—	—	—	—	—	—	—
	0.17	0.17	0.17	0.51	1.02	1.53	2.04	3.53	—	—	—

NOTE: The percentages of the ordinates relate to the maximum thickness of the corresponding section.

Table of offsets used for the geometry generation of the Ka4-70 propeller blades, given in van Manen, Member and Oosterveld [17].

Appendix C

Program files overview

With this thesis comes a series of files. To allow easy navigation and reproduction of results, a quick insight into the appended data shall be given here. Inside the program files, scripts and code documents, comments and interactive help (in case of the CASES file) are provided.

`optimization.fdbc` is the main CAESES file containing the entire parametric CAD model of the thruster (including electric motor specifications), as well as the result tables of all variants evaluated. The CAD tree is supplemented with descriptions of all top level scopes and features, as are the evaluations of the optimization tab. Two IGES export files are specified for the computational domain (including the nozzle geometry) and propeller export. A DesignLab engine is provided to manually investigate any variant of interest, although this requires further setup of the remaining framework on the local computer.

`meshingScript.glf` is the glyph script that allows automatic meshing of any geometry variant of interest. The path to the IGES files generated from within the `optimization.fdbc` file needs to be specified in 1.14 and 1.3541, as well as the export file location in 1.8741. The script can then be run from the shell for an automated process, or manually from the menu within Pointwise.

`OpenFOAMSetup` is a folder containing a prepared setup of the usual `0`, `constant` and `system` directories used with OpenFOAM. The version used within this thesis and needed to rerun any of the simulations without further adjustments is `v3.0+`. Further information on the necessary steps to repeat can be obtained from the `allrun` script.

`allrun` is the shell script specified within CAESES as executable that triggers the external computations. It is well documented and, together with the previously mentioned files, allows to run a fully automated optimization process based on CAESES. Besides the necessary software and the specification of paths locating the various import, export and result data within the affected files and scripts, no further tools are needed to repeat or append to the results of this work.

`CFDresults` is a folder that contains the geometry data and results of viscous flow simulations of the most interesting variants. The Baseline design at $J = J_d = 0.78$ is included, as well as the complete range of investigated advance

coefficients of the optimized variant. All simulations are run for $n_{rev} = 2$ revolutions and the latest time step as well as the forces, moments and logfiles of the entire simulation time are included. The evaluated results are also included in the result-tables of `optimization.fdbc`. Additionally, the results of the reference simulations featuring a Ka4-70 propeller in Nozzle 19a are included for all advance coefficients examined.

`referenceDesign.fdbc` is another CAESES file that contains the parametric geometry model of the Ka4-70 propeller in Nozzle 19A examined as a reference case.

Bibliography

- [1] W. M. J. Batten, N. W. Bressloff, and S. R. Turnock. “Transition from vortex to wall driven turbulence production in the Taylor-Couette system with a rotating inner cylinder”. In: *INTERNATIONAL JOURNAL FOR NUMERICAL METHODS IN FLUIDS* (2002), pp. 207–226.
- [2] M. E. Biancolini, I. M. Viola, and M. Riotte. “Sails trim optimisation using CFD and RBF mesh morphing”. In: *Computers and Fluids*, 93 (Apr. 2014), pp. 46–60.
- [3] N. Bulten and R. Suijkerbuijk. “Full scale thruster performance and load determination based on numerical simulations”. In: Third International Symposium on Marine Propulsors. Nov. 2013.
- [4] Q. M. Cao et al. “Effect of gap flow on the torque for blades in a rim driven thruster without axial pressure gradient”. In: *7th International Conference on Fluid Mechanics, ICFM7* (2015), pp. 680–685.
- [5] Q. M. Cao et al. “Prediction of loading distribution and hydrodynamic measurements for propeller blades in a rim driven thruster”. In: *Journal of Hydrodynamics* (Nov. 2011), pp. 50–57.
- [6] A. J. Dubas. “Robust Automated Computational Fluid Dynamics Analysis and Design Optimisation of Rim Driven Thrusters”. PhD thesis. University of Southampton, Oct. 2014.
- [7] A. J. Dubas et al. *Computational Fluid Dynamics Simulation of a Rim Driven Thruster*. Tech. rep. EPSRC Doctoral Training Centre grant (EP/G03690X/1). University of Southampton.
- [8] S. Ehlers et al. “Maritime-Port Technology and Development”. In: Kindle Edition. CRC Press, Oct. 2014, p. 129.
- [9] P. E. Farrell and J. R. Maddison. “Conservative interpolation between volume meshes by local Galerkin projection”. In: *Computer Methods in Applied Mechanics and Engineering* 200 (Jan. 2011), pp. 89–100.
- [10] M. D. Freeman and M. A. Marshall. “An analytical investigation into the design of a shaftless thruster using finite element and computational fluid dynamics approaches”. In: *Journal of Ocean Technology* 2011 6 (2011), pp. 55–68.
- [11] H. Grümmer and J. Frölich. *aXatlantic, aCROSS atlantic: autonomous, solar powered*. <http://axatlantic.com/>. 2016.
- [12] A. W. Hughes, S. M. Abu Sharkh, and S. R. Turnock. “Design and Testing of a Novel Electromagnetic Tip-Driven Thruster”. In: *School of Engineering Sciences, University of Southampton* (2000). unpublished.

- [13] A. W. Hughes, S. R. Turnock, and S. M. Abu Sharkh. "CFD Modelling of a Novel Electromagnetic Tip-Driven Thruster". In: *School of Engineering Sciences, University of Southampton* (2000). unpublished.
- [14] Ø. Kr, K. Andresesn, and N. Sand. "Thermal properties of a Prototype Permanent Magnetized Electrical Motor Embedded in a Rim Driven Thruster". In: (May 2006).
- [15] B. M. Kulfan. "Universal Parametric Geometry Representation Method". In: *Journal of Aircraft* 45 (Jan. 2008).
- [16] K. A. Lane and D. D. Marshall. "A Surface Parameterization Method for Airfoil Optimization and High Lift 2D Geometries Utilizing the CST Methodology". In: *47th AIAA Aerospace Sciences Meeting* (Jan. 2009). Including the New Horizons Forum and Aerospace Exposition.
- [17] J. D. van Manen and M. W. C. Oosterveld. "Analysis of Ducted-Propeller Design". In: The society of naval architects and marine engineers. Nov. 1966.
- [18] T. J. Michael. *AHFID Propulsor Performance Prediction*. paperback. 2002.
- [19] R. H. Myers, D.C. Montgomery, and C. M. Anderson-Cook. "Response Surface Methodology". In: 3rd ed. Wiley, 2009. Chap. 3.
- [20] R. H. Myers, D.C. Montgomery, and C. M. Anderson-Cook. "Response Surface Methodology". In: 3rd ed. Wiley, 2009. Chap. 1.
- [21] U. Nienhuis. "Analysis of thruster efficiency for dynamic positioning and low speed manoeuvring". PhD thesis. Delft University of Technology, 1992.
- [22] M. W. C. Oosterveld. "Wake adapted ducted propellers". PhD thesis. Delft University of Technology, 1970.
- [23] S. M. Abu Sharkh and S. H. Lai. *Design Optimization of a Slotless PM Brushless Motor with Helical Edge Wound Laminations for Rim Driven Thrusters*. Tech. rep. University of Southampton, 2010.
- [24] S. M. Abu Sharkh, S. R. Turnock, and G. Draper. "Performance of a Tip-Driven Electric Thruster for Unmanned Underwater Vehicles". In: vol. 2. International Offshore and Polar Engineering Conference. June 2001.
- [25] S. M. Abu Sharkh et al. *Prototype Integrated Electric Thrusters for Work-Class Underwater Vehicles: Design Construction and Test*. Tech. rep. EPSRC Research Grant Report. University of Southampton.
- [26] S. Subhas et al. "CFD Analysis of a Propeller Flow and Cavitation". In: *International Journal of Computer Applications* 55 (Oct. 2012).
- [27] G. I. Taylor. "Stability of a Viscous Liquid contained between Two Rotating Cylinders". In: *Transitions of the Royal Society of London* (1923), pp. 289–343.
- [28] J. F. Thompson, B. K. Soni, and N. P. Weatherill. "Handbook of grid generation". In: CRC Press, 1999. Chap. 21.

-
- [29] Tuomas Turunen. "Analysis of Multi-Propeller Marine Applications by Means of Computational Fluid Dynamics". An optional note. MA thesis. Aalto University, May 2014.
- [30] T. Watanabe et al. "Simulation of steady and unsteady cavitation on a marine propeller using RANS CFD code". In: *Fifth international Symposium on Cavitation (CAV2003)* (Nov. 2003).
- [31] A. Y. Yakovlev, M. A. Sokolov, and N. V. Marinich. "Numerical design and experimental verification of a rim-driven thruster". In: *Second International Symposium on Marine Propulsors* (June 2011).
- [32] J. Yao. "On the propeller effect when predicting hydrodynamic forces for manoeuvring using RANS simulations of captive model tests". PhD thesis. Technische Universität Berlin, 2015.